Dissertation

submitted to the
Combined Faculty of Mathematics, Engineering and Natural Sciences
of Heidelberg University, Germany
for the degree of
Doctor of Natural Sciences

Put forward by

Jan Otto Wolff, M.Sc.

born in: Berlin, Germany

Date of the oral examination: 23 November 2022

MINFLUX tracking of single fluorophore-labeled proteins with nanometer/millisecond spatio-temporal precision

Referees: Prof. Dr. Dr. h. c. mult. Stefan W. Hell
Prof. Dr. Joachim Spatz

Zusammenfassung

Wachsende Präzision und zeitliche Auflösung bei der Beobachtung von Dynamiken sind von entscheidender Bedeutung für die Erforschung zelluläre Prozesse und Funktionen. Im Feld der höchstauflösenden Mikroskopie rücken dabei die Auswirkungen von Markern auf die Probe stärker in den Fokus, wobei deren individuelle Einflüsse häufig unvorhersehbar sind. Fluoreszierende Moleküle stellen die bis heute minimalinvasivsten Marker dar, wurden jedoch wegen der limitierten Fluoreszenzphotonenrate für Hochgeschwindigkeitsmessungen durch die Verwendung großer Beads, die bis heute die höchste räumliche und zeitliche Präzision bieten, weitestgehend ersetzt. MINFLUX lokalisiert, selbst bei geringer Anzahl von Fluoreszenzphotonen, einzelne Moleküle mit Nanometer Präzision und bietet damit großes Potenzial für deren Verfolgung. Im Rahmen dieser Arbeit wurden, mit Hilfe eines neuen interferometrischen MINFLUX-Mikroskops, die Trajektorien einzelner, fluoreszenzmarkierter Motorproteine mit 3 nm Präzision, Kilohertz Aufnahmerate und nur 20 Fluoreszenzphotonen pro Messpunkt aufgezeichnet und damit die Messgeschwindigkeit kamerabasierter Einzel-Farbstoff-Studien um zwei Größenordnungen übertroffen. Eine umfangreiche Untersuchung der Schritte und Subschritte des mit einem einzelnen Farbstoff markierten Motorproteins Kinesin-1, löste Details in dessen Laufverhalten auf, die bisher ausschließlich durch Bead-Studien zugänglich waren und identifizierte so den umstrittenen ATP-Bindungszustand. Auf Grundlage dieser Ergebnisse erweist sich MINFLUX als eine wegweisende neue Technik für die hochaufgelöste Untersuchung von Proteinbewegungen bei minimaler Beeinträchtigung des biologischen Systems.

Abstract

Observing dynamics at increasing precision and temporal resolution is vital to extend the knowledge about inner-cellular processes and functions. At ever-shrinking scales, the influences of labels for super-resolution microscopy have become more and more relevant, with their impact often being unforeseeable. However, single fluorescent molecules, as minimally invasive labels, are substantially limited by the achievable fluorescence photon rate and have been outpaced by the use of large beads, which provide the highest spatio-temporal precision as of today. MINFLUX has shown high potential for tracking of single molecules and enables nanometric precision even at low fluorescence photon numbers. This thesis employs a new interferometric MINFLUX microscope achieving 3 nm precision, while following the trajectory of single proteins with kilohertz sampling at as little as 20 fluorescence photons, outperforming the measurement speed of camera-based single fluorophore tracking studies by two orders of magnitude. A broadly scoped investigation of the single fluorophore-labeled motor protein kinesin-1 resolved features of its stepping mechanism, so far exclusively accessible by bead tracking studies, and identified the disputed ATP binding state. In the context of these results, MINFLUX protrudes as a new technique versatile and decisive for studying fast protein movements with minimal interference with the biological system.

Contents

List of Abbreviations

1D	one dimension
1HB	one-head-bound
2D	two dimensions
2HB	two-head-bound
3D	three dimensions
ADP	adenosine 5'-diphosphate
AOTF	acousto optical tunable filter
APD	avalanche photodiode
ATP	adenosine 5'-triphosphate
BD	calcite beam displacers
BFP	back focal plane
EOAM	electro optical amplitude modulator
EOD	electro optic deflector
EOPM	electro optical phase modulator
FCS	fluorescence correlation spectroscopy
FIONA	fluorescence imaging with one nanometer accuracy
FOV	field of view
FP	focal plane
FPGA	field programmable gate array
FRAP	fluorescence recovery after photo-bleaching
FRET	Förster resonance energy transfer
FWHM	full width at half maximum
GLSE	generalized least-squares estimator
GSD	ground state depletion
HMM	Hidden Markov Model
IR	infrared
LS	line-shaped
MPH	motorized pinhole
PAINT	points accumulation for imaging in nanoscale topography
PALM	photoactivated localization microscopy
PIC	photon information content
RESOLFT	reversible saturable optical fluorescence transitions
RSS	residual sum of squares
RTP	rubidium titanyl phosphate
SBR	signal-to-background ratio
STED	stimulated emission depletion
STORM	stochastic optical reconstruction microscopy
STP	spatio-temporal precision

Preface

Progress in the field of life sciences comes hand in hand with improvements in both conceptualization and implementation of new techniques visualizing biological structures and processes with constantly greater detail. One fundamental aspect is the use of small fluorescent molecules to mark specific details of a sample with various degrees of complexity. These dyes can then be observed non-invasively utilizing a fluorescence microscope, under, apart from autofluorescence, near background-free conditions. While larger, brighter and more photostable emitters have been developed [1, 2] to increase contrast, precision and recording speed, single, small-molecule, organic fluorophores remain the go-to address, because they can routinely be introduced into living organisms. After the ability of microscopes to discern nearby molecules had been drastically increased with the introduction of super-resolution techniques like stimulated emission depletion (STED) [3, 4] and photoactivated localization microscopy (PALM) [5] or stochastic optical reconstruction microscopy (STORM) [6], biochemical labeling strategies with smaller linkers and high specificity needed to be developed [7, 8] to minimize the spatial mismatch between the fluorescent reporter and the structure of interest. Within the last decade, a localization precision of a few ten nanometers has become routinely available [9], with some examples even reaching single digit nanometer precision [10].

Besides the challenge of distinguishing close emitters for structural analysis, a similar approach applies to the observation of temporal changes in the position of single particles for studying their non-stationary organization of function. With increasing precision, a more and more detailed picture of individual particle kinetics have deepened the understanding of subcellular and macromolecular dynamics [11]. Still, the spatio-temporal precision (STP) of fluorescent single molecule tracking has so far been conceptually limited by the emission rate of fluorophores, despite improvements on the side of dyes [12] and anti-bleaching agents [13]. Since all super-resolution techniques obey an inverse square root dependency on the number of detected photons, a significant STP boost required the use of brighter, but thus larger emitters [14].

A paradigm shift to this problem was brought about by the recent introduction of MINFLUX [15]. It achieved nanometer precision at less than 1000 photons by overlapping the emitter position with an excitation intensity minimum. In the conceptual limit, the dye

can be localized without the need to emit photons, because the position of the laser beam within the sample is precisely known. Any recorded photons therefore imply a mismatch of the minimum and the fluorophore, and can be thus used to bring both closer together. As a result, MINFLUX minimizes instead of maximizes detection rates, fundamentally changing the way an emitter is localized. Even though the technique has developed fast, now extending to detection multiplexed dual-color and three dimensions (3D) measurements [16], it still has not exploited its full potential.

With the aim to prove that MINFLUX significantly advances the field of single molecule tracking, the scope of this thesis was to conceptualize, design and built a novel microscope based on the dynamic synthesis of an excitation profile featuring a line-shaped (LS) minimum for pushing the boundaries of tracking single, small-molecule fluorophores in terms of the precision achieved with a given number of detected photons (photon information content (PIC)). While chapter 1 and 2 of this thesis provide an introduction to super-resolution microscopy and single particle tracking as well as presenting the theoretical framework of MINFLUX, the herein presented microscope is described in chapter 3. The core component of this setup is the so-called phase scanner, a combination of two electro-optical modulators to interferometrically generate and move an LS minimum with microsecond response time. The phase scanner is capable of modifying the amplitude and phase of four different beams in the back focal plane (BFP). Precisely controlling the phase enables directing the LS minimum with sub-nanometer precision. High phase stability of the microscope is obtained by minimizing the beam length and ensuring that all beams pass the same optical components. Since in fact an LS minimum provides a higher curvature than the typically used donut-shaped intensity distribution [4], while also promising less residual intensity in the minimum, this approach to MINFLUX promised significant improvements of the STP as compared to current MINFLUX implementations. Chapter 4 benchmarks the presented MINFLUX microscope by localizing and tracking single, surface-immobilized ATTO 647N molecules. The PIC achieved proved to be three times higher than that of previous MINFLUX applications [17] and even ten times higher compared to that of camera-based methods [18]. As any improvement to the localization precision entails a quadratic increase in the number of detected photons, this implies that the herein presented MINFLUX microscope needs 100 times less photons to achieve the same tracking precision as camera-based methods. Further, these molecules were moved on a defined orbit, demonstrating that trajectories can be followed with a high accuracy necessary to derive profound biological models from recorded traces.
To challenge the exemplary tracking performance of the herein presented MINFLUX microscope, a broad and extensive study of the stepping motion of the motor protein kinesin-1 (from now on referred to as kinesin) was conducted and is presented in chapter 5. By recording 1762 traces of four kinesin constructs labeled at different protein posi-

tions, 16 nm steps and 8 nm substeps were observed. Evaluating the dwell times between steps allowed to derive kinesin's ATP binding state. By fueling the protein with a slowly hydrolizing ATP analogue, the mechanochemical stage of ATP hydrolisis was additionally concluded. By individually tracking the front, middle and back of kinesin's catalytic motor domain (head) and matching single traces along the microtubule cross section, the 3D-orientation of the unbound state of the labeled head could be reconstructed, allowing for inferences about kinesin's stepping mechanism. Overall, the herein presented MINFLUX microscope employing an LS minimum achieved between 1.5 nm and 3.5 nm precision within 0.63 ms sampling time, requiring only 20 - 100 fluorescence photons per localization and dimension. This outperforms by far other single fluorophore tracking experiments of kinesin by around two orders of magnitude in terms of the measurement speed without sacrificing precision.

Most of the single molecule localization and tracking data and all of the kinesin-tracking results presented in this thesis were also summarized to prepare a manuscript (see Publications), that was uploaded as a preprint on *bioRxiv* and is submitted for peer-review.

Chapter 1

Imaging and Tracking Below the Diffraction Limit

Until the late 90s, optical microscopy was thought to be eventually limited in resolution by diffraction. As light is an electromagnetic wave, it is diffracted while propagating through a microscope, causing a blurring of the original structure. Light with a wavelength λ, originating from a point sources in the object plane, transfers to nearly Gaussian shaped discs in the image plane with concentric dark and bright rings around it. The radius of the first dark ring is called Airy radius and it provides one measure for the smallest distance resolvable in a regular microscope [19]

$$r_{\text{Airy}} = \frac{0.61\lambda}{NA}. \tag{1.1}$$

Here NA denotes the numerical aperture of the optical system. This limit holds for light emitted from the sample to an image plane, as well as for light focused into the object plane to scan the sample.
However, since around the millennium new techniques have emerged in fluorescence microscopy, that were able to circumvent this physical limit with different approaches. These are similar in the fact that they use some kind of mechanism to switch fluorescent molecules between an observable on- and a non-observable off-state, such that ideally only one molecule within a diffraction limited area is in the on-state. Thereby the diffraction limit is not influencing the localization process. Most super-resolution techniques can be split up into coordinate-targeted and stochastic processes.

1.1 Coordinate-Targeted Super-Resolution

Generally speaking coordinate-targeted approaches use a single pixel detector and a structured, focused light beam (typically with a central intensity minimum) to illuminate a specific, well known point in the sample and record the fluorescence signal caused by excited fluorophores. This is repeated at different positions in the sample, generating a map of detected fluorescence signal. This map represents the distribution of fluorophores in the sample. But since light can not be focused to a spot much smaller than the wavelength nearby fluorophores will get excited simultaneously and therefore can not be distinguished.
In 1994 Stefan W. Hell proposed and later also demonstrated a method called STED [3] to reduce the area in which fluorophores are contributing to the fluorescence signal by utilizing stimulated emission depletion. This is done by overlaying the excitation beam with a second so-called depletion beam, which has a no intensity in its center and high intensity on a ring around it. Excited fluorophores being exposed to this ring are deexcited leaving only the ones in the center in an excited state to contribute to the fluorescence signal. The spatial width of fluorophores that remain in the excited state can be approximated by [20]

$$\sigma_{\mathrm{STED}} \propto \frac{\sigma_{\mathrm{PSF}}}{\sqrt{1 + I/I_S}} \tag{1.2}$$

with σ_{PSF} being the $1/\sqrt{e}$-radius of the focused excitation beam, I denoting the intensity of the deexcitation beam and I_S describing the intensity at which half of all fluorophores are deexcited.
The on- and off-state of STED are the first excited state of the molecule and the ground state. Switching between these states is driven by excitation (off to on) and emission of photons or depletion (on to off). Other techniques utilizing the coordinate-targeted approach are reversible saturable optical fluorescence transitions (RESOLFT) [21] and ground state depletion (GSD) [22].

1.2 Stochastic Super-Resolution

In contrast, stochastic approaches use a uniform illumination of the sample and a multi-pixel detector in an equivalent plane to detect the fluorescence signal. Each fluorophore generates a diffraction limited spot on the camera, causing the signal of adjacent molecules to overlap and makes them indistinguishable.

However, some fluorophores exhibit a long-lived, so called dark state where they do not show fluorescence. They can switch between this dark state and a fluorescent state either stochastically or induced by light. This property can be tuned by experimental parameters such that at any point in time only one fluorophore is in an excitable state within a diffraction limited region. Those can then be excited and generate non-overlapping spots on the camera. The position of each fluorophore can then be determined by centroid fitting. Since each spot is generated by a finite number of fluorescence photons N the precision of such a position is given by

$$\sigma_{\text{centroid}} = \frac{\sigma_{\text{PSF}}}{\sqrt{N}}. \tag{1.3}$$

Both coordinate-targeted and stochastic super-resolution approaches show an inverse square root dependency on either the number of illumination or fluorescence photons. Therefore a 10 times improvement in localization precision demands 100 times the amount of photons. In practice this causes a lower limit to the localization precision because of bleaching or limited photon rates. On a regular basis those techniques reach a localization precision of around 30 nm however the development of very photostable fluorophores, elaborate buffer systems and background suppression has also enabled measurements in the single nanometer regime [10].
The main super-resolution techniques with a stochastic switching approach are PALM, STORM and points accumulation for imaging in nanoscale topography (PAINT) [23]. They mainly differ in the specific realization of the dark state and the method by which the switching to the fluorescent on-state occurs.

1.3 Single Particle Tracking

Beyond the static observation of emitters with high precision, these concepts also play an important role in studying cellular processes, from the movement of whole cells [24–26] to the nanoscale dynamics of compartments [27] or even single proteins [28]. By engaging the temporal changes, studying their function as well as understanding underlying biophysical mechanism [29] is enabled. Contrary to discerning densely packed labels by photo-switching, tracking requires single emitters per diffraction limited region with stable emission rates. A multitude of techniques have emerged, that either gather information of ensemble kinetics like fluorescence correlation spectrocopy (FCS) [30, 31] or fluorescence recovery after photo-bleaching (FRAP) [32], or target the motion of individual particles [33]. The latter allows for direct observation of individual trajectories, thereby providing a much more direct visualization of the studied dynamics

A race for increasing temporal resolution and spatial precision has inspired the development of various tracking techniques, which in themselves provide a variety of STP and different degrees of parallelization. A straightforward approach is to label the particle of interest with a fluorescent dye or protein and monitor the signal of single emitters on a camera. Over a field of view (FOV) of up to $50\times\ 50\,\mu m^2$ this typically yields a lateral precision of down to 20 nm at a few 10 ms temporal resolution. By decreasing the temporal resolution to several 100 ms, sufficient photons can be collected to achieve nanometer precision [18]. However, as evident from equation 1.3 when replacing the number of detected photon by the fluorescence rate R and the measurement time τ

$$\sigma_{\text{centroid}}\sqrt{\tau} = \sigma_{\text{PSF}}\sqrt{R}^{-1}, \tag{1.4}$$

precision and temporal resolution cannot be changed independently from each other without changing the emission rate.

A higher STP can be achieved, when targeting individual molecules with a stationary illumination and collecting photons from different spatially-separated positions (typically in a tetrahedral arrangement). This can either be done by several spatially-separated detection volumes [34], or directly by generating multiple excitation spots [35]. The exact position of the emitter is then calculated based on the ratio of detected photons from the individual exposures and the sample is re-centered by for example a piezo-electric stage. Those techniques have reached below 10 nm lateral precision at 5 ms temporal resolution [35].

Instead of probing only a fixed number of positions, the molecule coordinates can also be extracted from a continuous scan around the last estimate. In orbital tracking [36], a confocal laser beam is moved on a circular orbit, while simultaneously collecting photons. If the emitter is not located in the center of that orbit, the detected signal will be modulated, due to the varying distance to the beam center. By the means of fast Fourier transformation, the displacement can be calculated and the orbit is recentered accordingly. Thereby single digit nanometer lateral precision was accomplished at the millisecond timescale.

Although targeted approaches have facilitated higher STP by injecting the well known laser position, they remained limited by the finite fluorescence rate of single molecules or proteins. Fluorescent beads have pushed the boundaries further, but the rate is still low compared to the number of photons per time generated by the excitation laser. To harvest the virtually unlimited supply of photons from the laser, techniques have emerged utilizing scattered light from 20 - 500 nm sized gold nanosphere [37]. Now, due to the much higher photon flux, these techniques can employ camera-based detection and even use high speed cameras with sub-millisecond recording times, thereby achieving around 2 nm precision within only 10 µs [38]. Again slight improvement can be made, when inducing

the position of a laser beam, that traps a transparent bead inside an optical gradient [39–41], which employing novel, improved beads have provided sub-nanometer precision at 10 µs temporal resolution [42].
Albeit the use of beads for labeling has significantly improved the STP of single particle tracking, it entails possible distortions of the observed dynamics due to their comparably large size, susceptibility to laser-induced heating [43] and hydrodynamic drag. Overall the challenge remains to strike a balance between minimally invasive labeling and high STP.

One very recent development in the field of super-resolution microscopy was the introduction of MINFLUX [15], which probed single emitters with a donut-shaped intensity distribution. By overlapping the emitter and the central intensity minimum of the donut, MINFLUX minimized emission rates needed for a precise localization. As a consequence, it increased the PIC and achieved unprecedented precision at a fixed number of photons. Following publications have employed MINFLUX for tracking [16, 17, 44], however a comprehensive study of dynamics utilizing MINFLUX was missing until today.

Chapter 2

MINFLUX - Beyond Conventional Super-Resolution Microscopy

The following sections are devoted to explaining the key features of MINFLUX and give a theoretical framework for the interferometric MINFLUX approach used in this work. As mentioned before, MINFLUX is a new super-resolution technique [15] that uses a coordinate-targeted localization scheme on switchable fluorophores, thereby combining key features of previously published conventional super-resolution methods. Each individual molecule is probed by several spatially shifted exposures, covering an area with diameter L, using a donut shaped excitation beam in two dimensions (2D) or 3D. Its position is then calculated from the detected photon counts (typically by a maximum-likelihood estimator), requiring precise knowledge of the excitation intensity distribution and the position of the beam center. Balzarotti et al. were able to reach a localization precision of 1 nm for 2D-localizations [15] and around 2 nm for 3D-localizations [16]. Further two-color MINFLUX experiments have shown to be able to clearly resolve distances of 10 nm. The color separation was done by spectral identification of individual on-events. The high localization precision of MINFLUX is achieved by an iterative localization scheme and harvesting the increased PIC close to the molecule position.

One recently published localization scheme, that also iteratively approaches the molecule position is called MINSTED [45]. Instead of directly targeting the fluorophore with a local intensity minimum, MINSTED orbits around the dye with an excitation beam, overlaid with a STED beam. By continuously decreasing the orbit diameter and the effective width of the excitation spot (by increasing the STED power), this technique has enabled sub-nanometer precision [46].

Besides, further camera-based super-resolution techniques have emerged that show an increased localization precision by probing the molecule position with an intensity minimum. Those have been termed as MINFLUX-like localization schemes, which shows that

the main paradigm change of MINFLUX has yet to be better understood. While these techniques have shown remarkable results, they are still limited by a pure inverse square root dependency between the achievable precision and the detected number of photons.

2.1 Overcoming the Inverse Square Root Dependency

Increasing the PIC means to gain resolution faster than in conventional super-resolution techniques, thus overcoming the inverse square root dependency. Taking a closer look at the shape of the inverse square root function one can see that it decays fast in the beginning and then flattens out causing a further increase in localization precision to strongly increase the demand for recorded photons. In other words the first few detected photons already allow for a fair position estimate. Meanwhile a lot of photons are needed to precisely pin down the exact position.

MINFLUX is exploiting this fast initial decay by combining the single localization to an iterative procedure of subsequent localizations, each following the inverse square root dependency, but only collecting a few highly informative photons. Harvesting this, the localization precision increases much faster than for a single measurement.
The individual localizations consist of probing the molecule with a well known excitation pattern. Typically this pattern is chosen to a have a local intensity minimum with strong curvature to achieve high contrast however this is not the only possible form. An estimate for the molecule position is derived from the detected signal and after each iteration the pattern is adjusted to a smaller probing region around this location. Iteratively the position estimate is refined until the dye bleaches.

2.2 One Dimensional MINFLUX Localization

In this work 2D-localizations are performed by two independent, orthogonal localizations along one dimension (1D) each employing an excitation pattern featuring an intensity minimum along the axis of localization. The major advantages of this approach are the reduced complexity for creating the excitation pattern and the higher curvature around the local minimum both enabling a higher curvature to offset ratio. Following sections will show that this ratio is in practice one limiting factor of MINFLUX concluding that the 1D MINFLUX localization should outperform the 2D-donut. This section will therefore treat the mathematical framework for the case of a single one dimensional localization

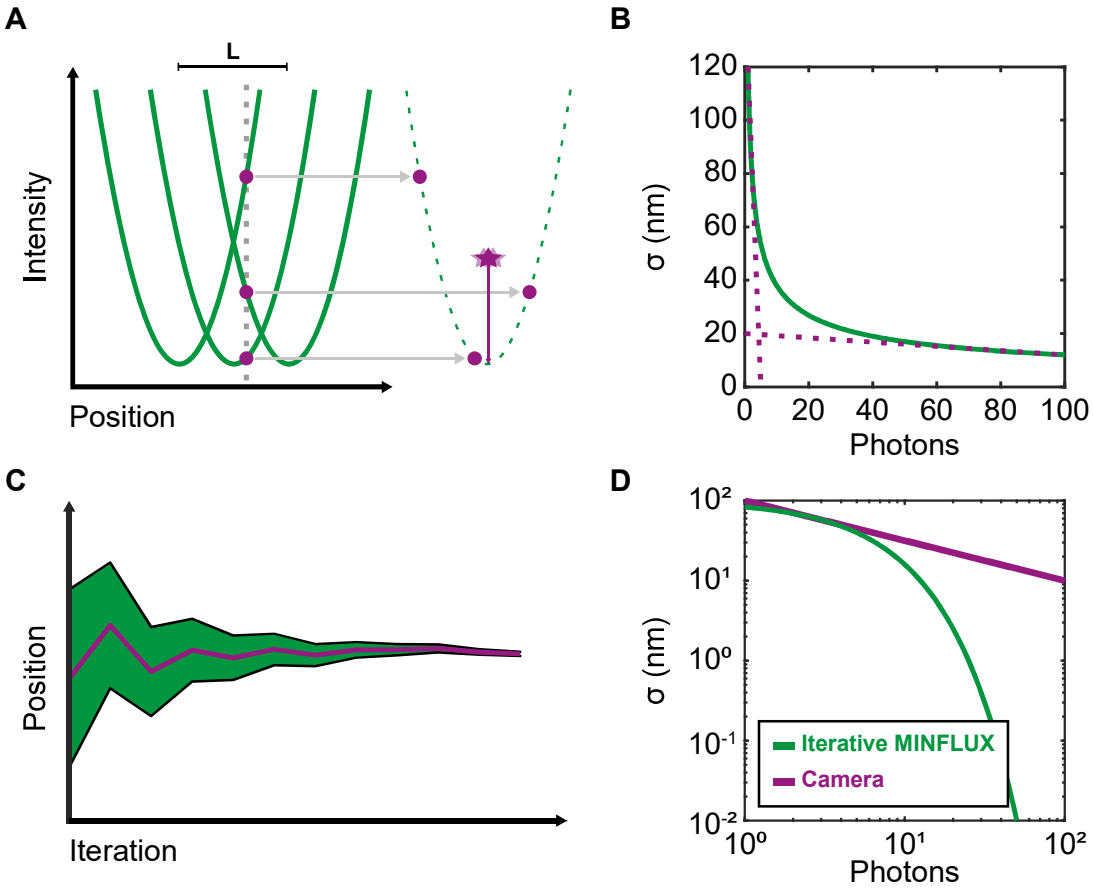

Figure 2.1: **Conceptual MINFLUX localization**, **(A)** An emitter probed by three shifted exposures separated by distances of $L/2$, employing a parabolic intensity distribution. The reconstruction of the parabola from the measured photon counts yields the emitter position. **(B)** Inverse square root dependency (green) with the purple dashed lines highlighting the fast initial decay and the flattening towards the end. **(C)** Procedure of an iterative localization of a single emitter with a stepwise reduction of L. The purple line depicts the position estimate and the green shaded area denotes the measurement interval $\pm L/2$. **(D)** Exponential gain in precision for iterative MINFLUX (green) versus camera-based precision (purple).

with a parabolic excitation

$$y(x) = a + b(x - x_m)^2 \tag{2.1}$$

with x_m being the true molecule position relative to the intensity minimum of the parabola, b the curvature of the parabola and a the offset. Higher dimensions can then be treated as multiple applications of the one dimensional case.

In order to find the molecule position, three points close to the molecule are probed by the parabola centered at $x = [-L/2, 0, L/2]$, yielding a total beam displacement L. As

the number of fluorescence photons is proportional to the excitation intensity

$$N \propto I(x_m) \tag{2.2}$$

the average photon counts at these points are given by

$$\begin{aligned} n_0 &= a + bx_m^2 \\ n_1 &= a + b(x_m - L/2)^2 \\ n_2 &= a + b(x_m + L/2)^2. \end{aligned} \tag{2.3}$$

The curvature is for example influenced by the fluorescence quantum yield and the excited state lifetime. Factors influencing the background are residual laser intensity in the minimum, fluorescence background and detector dark counts.
This set of equations is sufficient to retrieve all three unknown parameters. Solving the set of equations directly is possible, but here a more general way featuring least-squares regression is chosen. Therefore, the parabolic shape of the excitation function is described by its linear form

$$y(x) = \beta_1 + \beta_2 x + \beta_3 x^2 = \begin{pmatrix} \beta_1 & \beta_2 & \beta_3 \end{pmatrix} \begin{pmatrix} 1 \\ x \\ x^2 \end{pmatrix} \tag{2.4}$$

that can be transformed back to equation 2.1 by the following relations

$$\begin{pmatrix} a \\ b \\ x_m \end{pmatrix} = \begin{pmatrix} \beta_1 + \frac{\beta_2^2}{4\beta_3} \\ \beta_3 \\ \frac{-\beta_2}{2\beta_3} \end{pmatrix}. \tag{2.5}$$

Invoking this linear form of the set of equations, a linear regression analysis

$$\hat{\beta} = \arg\min_{\beta} \sum_i (n_i - y(\beta, x_i))^2 \tag{2.6}$$

can be performed. Together with the transformation relations, this gives an analytic expression for the position estimate x_{GLSE} based on the beam displacement L and the measured photon counts

$$x_{\mathrm{GLSE}} = \frac{L}{4} \frac{n_2 - n_1}{n_1 + n_2 - 2n_0}. \tag{2.7}$$

This estimate is equal to the generalized least-squares estimator (GLSE), which weights each exposure by the inverse of the corresponding photon counts to approximate the Poisson noise. For a more detailed mathematical description of the least-squares approach refer to section A.1.

This estimation works well, as long as the contrast between the different exposures and the excitation minimum is sufficient. Otherwise the denominator of equation 2.7 will be close to zero, causing noise to have a strong impact on the calculated position. The precision of this estimates can be approximated by consulting the covariance matrix of the linear parameters $\Sigma_{\hat{\beta}} = \left(X^T \Sigma_y X\right)^{-1}$ and Gaussian error propagation

$$\sigma = \frac{L}{2} \frac{\sqrt{(n_2 - n_1)^2 n_0 + (n_2 - n_0)^2 n_1 + (n_1 - n_0)^2 n_2}}{(n_1 + n_2 - 2n_0)^2}. \tag{2.8}$$

Further was assumed that the photon noise is Poissonian. If the molecule is located at $x_m = 0$ and assuming zero background ($a = 0$) this formula can be simplified to

$$\sigma = \frac{L}{4\sqrt{N}} \tag{2.9}$$

by evoking the exact shape of the parabola 2.1. The value $N = \sum_i n_i$ accounts for the total number of photons measured. The uncertainty scales with the distance L of the exposures and improves with the inverse of the square root of the number of photons.

2.2.1 Background Considerations

For non-zero background ($a \neq 0$) inserting equation 2.3 into equation 2.8 at $x_m = 0$ and substituting the total photon number $N = \sum_i n_i$ yields

$$\sigma = \frac{L}{4\sqrt{N}} \sqrt{1 + \frac{5}{2\mathrm{SBR}} + \frac{3}{2\mathrm{SBR}^2}}. \tag{2.10}$$

Here the expression

$$\mathrm{SBR} = \frac{bL^2}{4a} \tag{2.11}$$

has been redefined as the signal-to-background ratio (SBR). It represents the average ratio of background subtracted photons collected at a distance $L/2$ from the molecule (signal) and the number of photons detected at the molecule position (background). While the precision could be improved arbitrarily for the background free case by reducing L this is not possible with background. Simply setting the derivative of equation 2.10 in terms of L to zero and considering the L dependency of the SBR results in an expression for the smallest feasible L-value and therefore also in a optimal value for the SBR. When reducing L such that

$$\mathrm{SBR}_{\mathrm{opt}} = \sqrt{\frac{3}{2}} \tag{2.12}$$

the precision achieved with a fixed number of recorded photons is highest. This criteria is more useful than directly calculating $L_{\min}$ since it does not require knowledge of the curvature and offset of the parabola, two parameters that are usually unknown under experimental conditions.
Still, inserting the calculated $L_{\min}$ and $\mathrm{SBR}_{\mathrm{opt}}$ into equation 2.10 yields the optimal precision

$$\sigma_{\mathrm{opt}} \approx 1.11\sqrt{\frac{a}{bN}} \tag{2.13}$$

that can be achieved with a given parabola and number of photons. Without surprise, the lowest achievable precision scales with the inverse square root of the number of detected photons N. However it further only depends on the curvature b to offset a ratio of the parabola. Therefore substantial improvement in the localization precision of MINFLUX is directly linked to improving this ratio by either reducing residual laser intensity in the minimum or by an excitation beam with higher curvature.

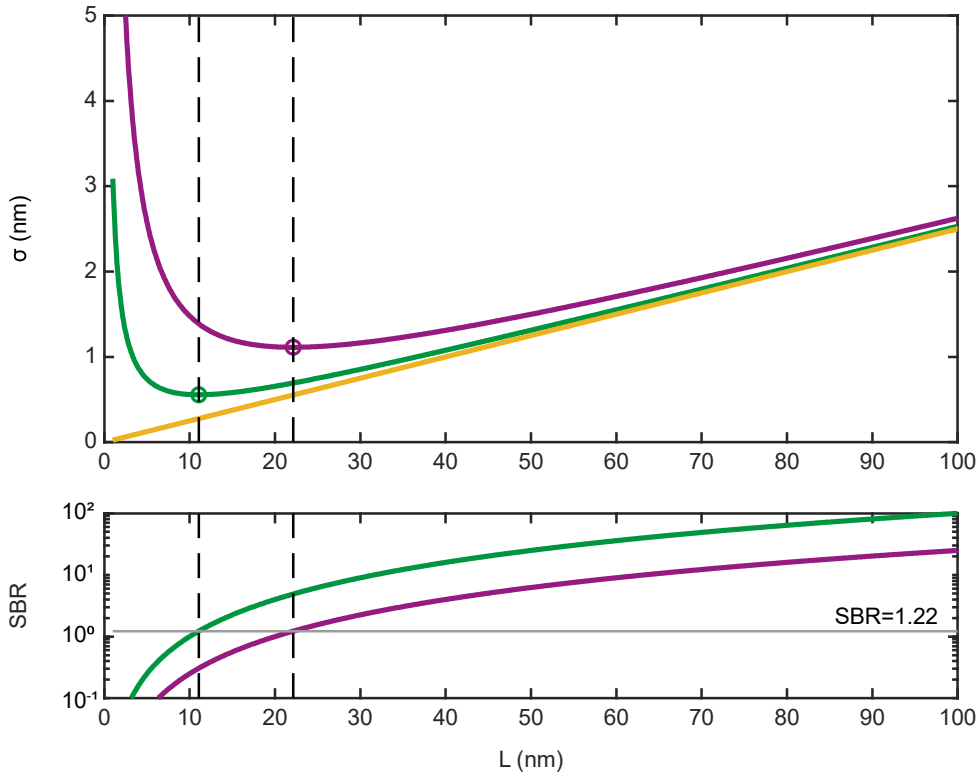

Figure 2.2: **Localization precision and SBR for one dimensional localization as a function of L**. The upper plot shows the localization precision as a function of beam displacement L for a parabolic excitation and different background contributions. The bottom plot shows the corresponding SBR as a function of L. The SBR for the yellow curve is ∞ and therefore not shown.

2.2.2 Iterative MINFLUX Imaging Precision

As mentioned before, one main characteristic of MINFLUX is overcoming the inverse square-root dependency by iteratively zooming-in closer on the molecule position. This aspect is especially useful for imaging applications, where only a limited fluorescence photon budget per molecule is available. This section shall derive a possible procedure for this zooming-in process and give a mathematical description of the precision to photon relation. For a more detailed description of the derivation refer to section A.2.
Assuming again a background free localization with a precision given by equation 2.9, the calculated position is then used to zoom-in on the molecule, by starting a new measurement with reduced L centered around the previous position estimate.
One easy comprehensible way to set the reduced L-value is to set it proportional to the uncertainty of the previous measurement

$$L_{k+1} = \alpha\sigma_k. \tag{2.14}$$

The regularization parameter α thereby defines the speed of performing the zoom-in process, while ensuring that a large fraction of molecules is located within the probed region of the next iteration. Combining this procedure with equation 2.9 and starting at the diffraction limited precision σ_0, the precision after k steps is given by

$$\sigma_k = \frac{\alpha\sigma_{k-1}}{4\sqrt{N_k}} = \sigma_0 \frac{\alpha^k}{4^k\sqrt{\prod_{i=1}^{i=k} N_i}}. \tag{2.15}$$

This equation leaves three parameters for optimization, the number of iterations k, the amount of detected photons per iteration N_i and the scaling value α for reducing L. Mathematically optimizing N_i and k in terms of highest precision with a fixed number of total photons N_{tot} simplifies equation 2.15 to

$$\sigma_k = \sigma_0 e^{-8N_{tot}/e\alpha^2}. \tag{2.16}$$

With this iterative approach it is possible to replace the inverse square-root dependency for the localization precision with an inverse exponential dependency. This decays significantly faster than the square-root law, enabling single nanometer precision with less than 100 recorded photons (see figure 2.1 **(D)**).

2.2.3 MINFLUX Tracking Precision

In tracking applications, besides the spatial precision, the temporal resolution becomes relevant for studying dynamics. Equation 1.4 discloses that the STP for camera-based tracking in fundamentally limited by the diffraction limited size of the emission spot and the fluorescence detection rate. The reduced number of photons needed with MINFLUX, will surpass these limitations, but MINFLUX tracking offers an even more substantial advantage over camera-based tracking. As MINFLUX directly targets the molecule position with the precisely known minimum of the excitation laser beam, it makes repetitive zooming-in obsolete, if the speed of movement is not significantly larger than $L/\tau \approx 30\,\mu\mathrm{m\,s}^{-1}$. Under this weak constraint, the molecule position of the following localization will be in close proximity to the last estimate allowing for continuous measurements with the smallest L and hence exploiting the maximal available PIC. This even reduces the number of fluorescence photons needed to achieve a given tracking precision as the photons needed to zoom-in only need to be spend once and do not contribute to further localizations.
This allows to simply use equation 2.9 for estimating the localization precision, instead of equation 2.16. By substituting the number of detected photons N with the fluorescence rate R and the measurement time τ

$$\sigma\sqrt{\tau} = \frac{L}{4}\sqrt{R}^{-1} \tag{2.17}$$

yields a STP for MINFLUX, which depends on the spacing of exposures L and the detection rate. Hence, the precision and temporal resolution can in fact be adjusted independently, by varying the spacing of exposures L, theoretically resulting in infinite STP in the limit $L \to 0$.
In practice, unlike for camera-based techniques, the lower bound to the STP is not only given by the emission rate, but also by the depth of the intensity minimum, as this determines the smallest usable L. When assuming equal emission rates and an L of 30 nm, which has been routinely applied throughout this thesis, MINFLUX is expected to achieve an around ten-fold improvement in STP compared to camera-based tracking. This significant increase facilitates tracking of for example proteins with millisecond temporal resolution and nanometer precision, whilst only requiring a small fluorophore for labeling instead of a bulky bead. In comparison to fluorescence imaging with one nanometer accuracy (FIONA) [18] measurement times are reduced more than 100-fold at similar spatial precision, making single fluorophore tracking compatible with optical traps and scattering microscopy.

2.3 Wavelength Dependency in MINFLUX

As stated by equation 2.9 an ideal background free MINFLUX localization does not depend on the excitation wavelength. Although the curvature of the parabola in fact does depend on the wavelength, its changes can simply be compensated by increasing the laser power. However, in practice MINFLUX measurements will become wavelength dependent because of the finite background in the intensity zero of the excitation profile, because of sample background and ultimately due to detector dark counts. The difference in curvature can then not be counteracted by the laser power, without also increasing background. As stated by equation 2.13, the localization precision will be limited by the SBR. Independent of the background source the SBR (equation 2.11) scales with the curvature b of the parabola. This curvature scales inversely with the wavelength, causing shorter wavelengths to have a higher curvature.
Nevertheless, also the background is wavelength dependent, since most samples exhibit more autofluoresce, when excited with shorter wavelengths. Further, different dyes emit at different fluorescence rates, thus making sample background more or less relevant. Last but not least the residual intensity in the excitation minimum depends on the coherence length of the laser. This is a manufacturing problem which is handled best for lasers around 550 nm.
All these factors combined prevent stating a preferred wavelength for MINFLUX. The wavelength has to be chosen individually based on technical limits of the microscope and restrictions from the sample.

Chapter 3

A Phase Scanning MINFUX Microscope Designed For Tracking

This work uses a custom built MINFLUX microscope, employing a so-called phase scanner to interferometrically synthesize an excitation intensity distribution featuring an LS minimum. By alternating 1D-localizations along the x- and y-direction, it records the 2D-trajectory of an emitter with nanometer precision and down to microsecond temporal resolution. The microscope described in this section is included in a submitted manuscript (see Publications).

3.1 Setup

All excitation lasers are placed on a second smaller optical table preventing heat transfer into the microscope. Further, different sections of the microscope were separated by darkening walls reducing air flow. Also drivers, the computer and power supply were installed on a rack above the optical table allowing for short cables while decoupling vibrations caused by fans used for cooling. The basic structure of the microscope and its components are depicted in figure 3.1.
The light from up to three different single frequency laser sources with wavelength 642 nm (Bolero, Cobolt AB, Solda, Sweden), 561 nm (Jive, Cobolt AB, Solda Sweden) and 488 nm (Calypso, Cobolt AB, Solda, Sweden) are overlapped by a long-pass (LP) and a short-pass (SP) filter and, before being coupled into a single mode fiber (P1-405BPM-FC-5, Thorlabs Inc., Newton, USA), power controlled by an acousto optical tunable filter (AOTF) (97-01776-0, EQPhotoncs, Paolo Alto, USA). The light and fiber polarization angle are matched by a half-wave plate. By a second half-wave plate and a Glan-Thompson

polarizer (GT) the polarization state after the fiber is again cleaned up, to a assure a single polarization state and maximal power output. An additional half-wave plate is included on a motorized rotation mount (PRM1, Thorlabs Inc., Newton, USA), which modulates the power distribution between the beamlets and thereby optimizes the depth of interference.
Then the laser beam travels through the phase scanner described in section 3.2, which forms four beamlets with defined amplitude and phase. The non-matching polarization state of opposing beamlets after the phase scanner are aligned by a custom built segmented half-wave plate such that each beamlet is polarized orthogonally to the axis of displacement from the center of all beamlets.
The transmitted beamlets of a 90:10 (R:T) non-polarizing beam splitter cube (BS076, Thorlabs Inc., Newton, USA) are again divided by non-polarizing beam splitter cubes and recorded by a powermeter (S121C, Thorlabs Inc., Newton, USA) and with cameras (Basler Ace acA1920-155μm, Basler AG, Ahrensburg, Germany) in planes conjugated to the BFP the focal plane (FP), which are used for the calibration of the phase scanner.
A quad band dichroic mirror (ZET 405/488/561/640nm-TRFv2, Chroma Technology, Bellows Falls, USA) guides the other 90 % of the laser power into the galvanometer scanner. This is built up of four digitally encoded galvanometric scanning mirrors (GM-1015 with Ag mirrors, Canon Precision Optical Industry Co. Ltd., Tokyo, Japan) in a custom designed QuadScanner arrangement [47]. The galvanometric scanners are driven by two controllers (Canon GC-211). In order to establish a similar power load between both controllers, each steers one x and one y mirror. At the given 100-fold magnification between the galvanometer scanner and the sample space, the precision of the digital encoders translate into a resolution of less than 1 nm and a FOV of $35\times35\,\mu m^2$. Also a positional jitter of below 1 nm is produced by the feedback loop.
Then the laser is coupled into a Leica DMi8 microscope body (Leica Microsystems, Wetzlar, Germany) through the rear infinity port and directed towards the objective lens (Leica HCPL Apo 1.4 100x OIL STED white, Leica Microsystems, Wetzlar, Germany) by a mirror. The stage consists of a custom built glass holder for the sample that, by piezo actuators (SLC1730, Smaract GmbH, Oldenburg, Germany), can be moved over the range of several millimeters in 3D with nanometer resolution.
Fluorescence light emitted by the sample is descanned by passing backwards through the galvanometer scanner and, at the quad band filter, gets decoupled from the excitation beam. A $f = 400\,mm$ achromatic lens is used to focus the light onto a motorized pinhole (MPH16-A. Thorlabs Inc., Newton, USA). The pinhole can be varied in size between 35 µm and 2 mm which at a total magnification of 200x, compared to the FP of the objective, translates to 125 nm to 10 µm in the sample space. The pinhole size is routinely chosen to be larger than the periodicity of the interference pattern in the FP to 350 nm. After the motorized pinhole (MPH) fluorescence light is collimated and passes a cascade of

dichroic filters towards one of three spectrally separated avalanche photo diode detectors (SPCM-AQRH-13-ND, Excelitas Technologies Corp., Waltham, USA). The exact filters used can be found in 3.1.

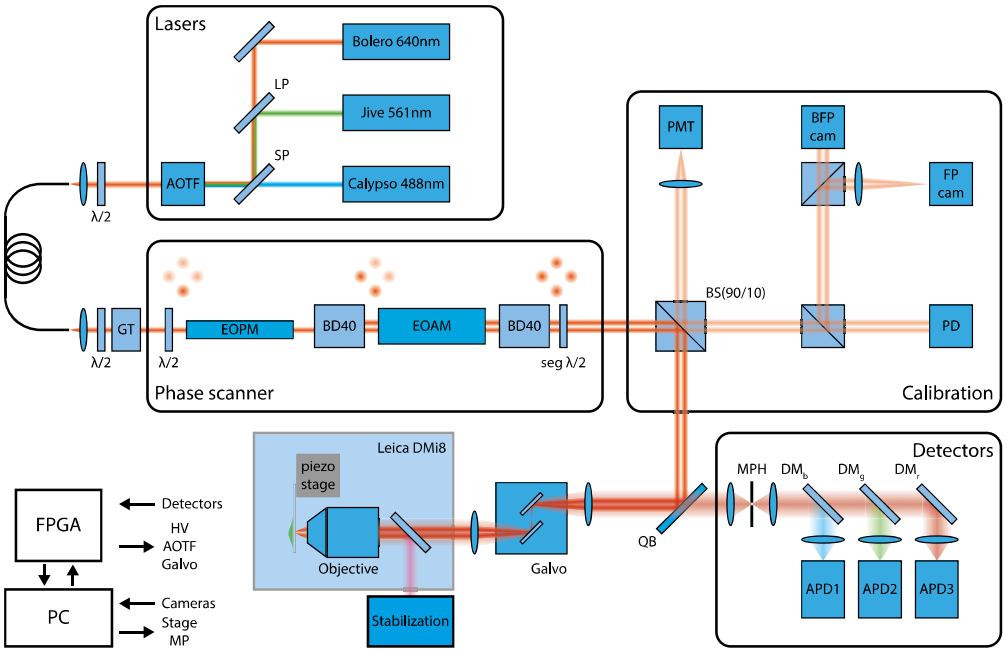

Figure 3.1: **Compact representation of the MINFLUX microscope** with all components except mirrors. Light from three different single frequency lasers is overlapped by a long-pass (LP) and a short-pass (SP) filter and power controlled by an AOTF before coupling into a single mode fiber. After the fiber the polarization is cleaned up by a half-wave plate ($\lambda/2$), Glan-Thompson polarizer (GT) combination and the laser beam passes the phase scanner (see section 3.2.2). Ten percent of the beamlets are split from the main beam path to the calibration section used for diagnostics and calibration of the phase scanner. The main power of all beamlets passes through the galvo scanner and enters the Leica DMi8 microscope body trough the rear port. Fluorescence signal emitted from the sample is collected by the objective, descanned, passes the quad-band filter (QB) and is focused on to the MPH. After the pinhole, the light is spectrally split by a cascade of dichroic mirrors (DM) and focused on an avalanche photodiode (APD). The microscope is controlled by USB (PC) as well as digital and analogue outputs from the field programable gate array (FPGA) used for real time data processing. The infrared light of the stabilization unit (see section 3.4) is overlaid with the excitation beam by a short-pass filter below the objective lens. (EOPM-electro optical phase modulator, EOAM-electro-optical amplitude modulator, BD40-polarization dependent beam displacer, PMT-photomultiplier tube, BFP cam-camera in plane conjugated to the BFP, FP cam-camera in plane conjugated to the FP, PD-photo diode, HV-high voltage)

Further the reflected light of the excitation laser, also travels backwards through the mi-

croscope and, after the 90:10 (R:T) non-polarizing beam splitter cube, is focused onto an independent 25 µm pinhole in front of a photon multiplier tube (H14119-40, Hamamatsu Photonics, Hamamatsu, Japan). Besides utilizing this signal to match the axial position of the sample with the excitation laser focus, it also reports about reflection or local scattering processes.
The data acquisition and time-critical processing, such as hardware control, is done by a field programmable gate array board (FPGA, PCIe-7852R, National Instruments, Austin, USA), which ensures exact timing down to 10 ns. Several analog outputs (AO) with 16 bit precision and megahertz update rates, analog inputs as well as digital inputs and outputs (DIO) are employed by the FPGA board at a 100 MHz clock. LabView (National Instruments) is used to program the FPGA. During measurements, the galvanometer scanner (by DIO) and the phase scanner (by AO) are directly controlled by the FPGA. It also records detected photons (by DIO and AI), computes new estimates of the molecule position and transfers results to the host computer via first-in-first-out (FIFO) memories.
For long term measurements, lasting from several minutes up to hours, the sample can be stabilized by measuring the position of an aluminum grating on the objective facing side of the cover glass and actively counteracting occurring drift with the piezo-electric stage. For this purpose an infrared (IR) laser is coupled into the microscope body below the objective lens via a shortpass filter. A detailed description see section 3.4.

Table 3.1: **List of bandpass filters used in the detection cascade.** The filters were manufactured from Idex Crop., Lake Forest, USA and used at low incident angles.

Abbrevation	**Wavelength range**	**Product name**
DM_b	525±50 nm	Semrock 525/50 Brightline HC
DM_g	600±52 nm	Semrock 600/52 Brightline HC
DM_r	731±137 nm	Semrock 731/137 Brightline HC

3.2 Phase Scanning

The setup built and used within this thesis comprises a phase modulation based scanning system for addressing positions with an intensity minimum within the size of a diffraction limited spot. This is implemented by illuminating the back aperture of the objective with four individual laser beams. Those beamlets can be modified in intensity and phase by electrooptical amplitude and phase modulators. In contrast to combining phase masks and an electro optic deflector (EOD), which were used in previous MINFLUX publications, to generate and move the intensity minimum around the molecule position, the phase scanner combines generation and movement of a local intensity minimum without being restricted to a single operating wavelength. Our phase scanning approach can easily

be combined with other scanning devices, because it only changes the phase but not the position or direction of the beam. This also means that the beam is correctly descanned at any timepoint without further losses.
The principal behind the scanning mechanism is controlling the interference pattern of multiple overlapping beams. Consider for example two parallel beams in the BFP. They are interfering in the FP to create an intensity pattern with interference fringes in the direction of separation. If the two beams are 180° phase shifted they will interfere destructively within the plane perpendicular to the separation of the two beams. Outside of this plane the path length difference between the beams changes causing the intensity to rise. By varying the phase difference between the beams destructive interference can be created an any point and thereby shifting the LS minimum of destructive interference. By controlling the phase difference one can hence address defined lines in the diffraction limited spot with the intensity zero. Figure 3.2 shows the intensity pattern and profiles for different phase lags.

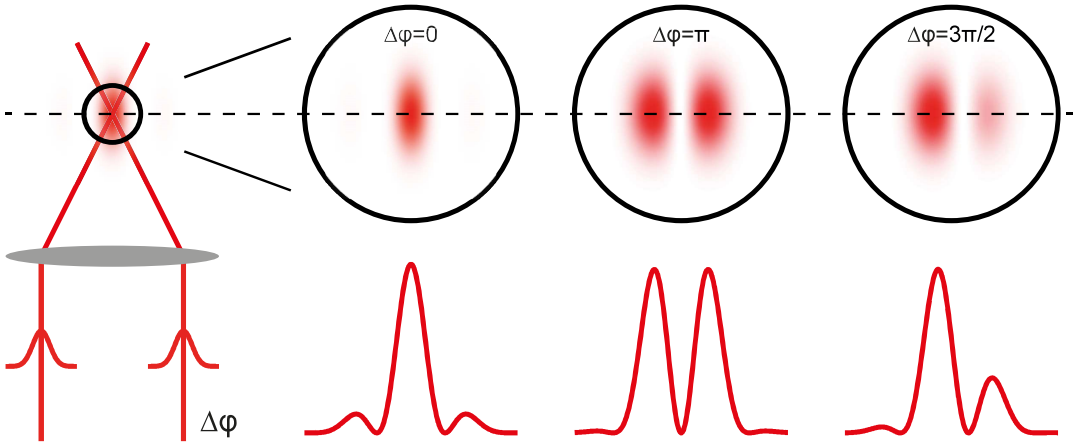

Figure 3.2: **Phase scanner concept** sketched by the interference of two beamlets in the FP of a lens. Changing the phase difference between the two beams moves the minimum of the intensity pattern along the axis of beam displacement. The normalized intensity profiles are displayed below the corresponding 2D-patterns.

The phase scanner is particularly useful for MINFLUX, where a molecule is localized by probing its position with at least two intensity minima and then iteratively reducing the probing width around the molecule position. With the phase scanner this procedure can be repeated without having to consider inertia of e.g. scanning mirrors. This increases the response time by 3 orders of magnitude compared to mechanical scanners. The limited scan range of the phase scanner is not considered a disadvantage since the localization precision is expected way below the diffraction limit. To achieve large fields of view, a different scanning system like a galvanometer or a tip tilt mirror can be added to the

system. Intrinsically the phase scanner includes control over the excitation pattern. In particular it can switch between an excitation spot and the donut pattern in the order of microseconds which could also be done by switching between different beampaths but requires precise alignment of these beampaths and is susceptible to beam drift.
Further the phase scanner is not restricted to operation at only a single wavelength. Since it is based on interference any coherent light source can be used. Switching between different wavelength is mainly limited by the on and off switching time of the laser, making this approach significantly faster than for example a spatial light modulator.

3.2.1 Electro-Optical Modulators

One way the phase difference of the two beams can be modulated is by electro-optical devices. Those allow phase changes on the timescale of microseconds and even down to nanoseconds, mainly limited by the electric rise and fall times of electrical amplifiers. The physical concept of these electro-optical modulators is the Pockels effect. It describes a change in refractive index of birefringent crystals caused by an electric field [48]. For the dominant linear electro-optical effect the change in the refractive index matrix [49]

$$\Delta(1/n^2)_{ij} = \sum_k r_{ijk} E_k \tag{3.1}$$

scales with the electro-optical coefficient r_{ijk}. This tensor links the individual electric field components E_k to the axes of the refractive index matrix. Typically the electric field is applied in direction of one of the crystal axes which reduces the amount of coefficients needed significantly. In practice modulators are characterized in terms of the so called half-wave voltage

$$V_\pi = \frac{\lambda d}{n^3 r l} \tag{3.2}$$

defining the voltage causing a phase difference of π.

3.2.2 Implementation

As described in section 2.2 this setup performs 2D-localizations by successive 1D-localizations with an excitation pattern featuring an LS minimum. These orthogonal excitation patterns are created by two sets of beamlets in the BFP, one consisting of two horizontally displaced beams and the other consisting of two vertically displaced beams. Our phase scanner can switch electro-optically between these two sets and further modulated the phase difference between the two beamlets.
A straightforward approach of splitting a single beam into multiple beamlets modulating

them in phase and later recombining them, bears the problem that the different beam paths cover a large area and therefore are susceptible to temperature differences, air flow and local beam drift causing the phase difference to be very unstable. In this setup we designed a very compact phase scanner employing commercial calcite beam displacers (BD) (BD40, Thorlabs Inc., Newton, USA) and custom built electro-optical modulators made from rubidium titanyl phosphate (RTP) crystals (custom manufactoredby Crystal Laser, P.A. du Breuil, France). Those BD are also birefrigend crystals that displace orthogonally polarized beams by a defined distance. The electro-optical modulators consist of two orthogonal oriented crystals with electrodes mounted along the axis of highest electro-optical coefficient. The combination of two crystals reduces the temperature dependence of the phase shift by exposing the beam to both refractive indices of the crystal.

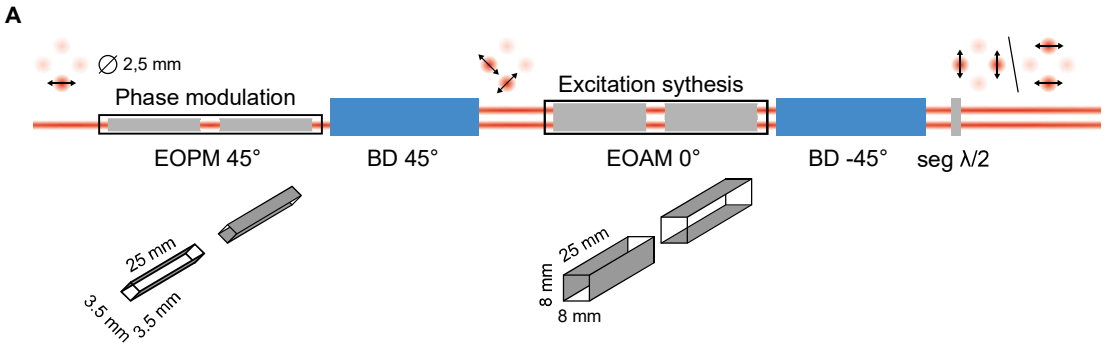

Figure 3.3: **Technical implementation of the Phase Scanner** consisting of two electro-optical modulators each made from two orthogonal RTP crystals and two BD. The two diagonal polarization component of the incoming horizontal polarized laser beam are modulated in phase against each other by the phase modulator. These components then are separated by the first BD. The polarization of these two beams can then either be rotated 90 deg or kept constant before being again displaced by the second 90 deg rotated BD. The remaining pattern either consists of two horizontally displaced or two vertically displaced beamlets with a phase difference defined by the phase modulator.

Figure 3.3 shows the sequence of components used. A singe horizontal linear polarized laser beam enters the first electro-optical modulator, later referred to as electro optical phase modulator (EOPM), at a 45 deg angle to the crystal orientation. A modulation of the applied voltage induces a phase modulation in the two polarization components along the crystal axes. Those polarization components are then split up by the first BD creating two beamlets with controllable phase difference. The two beamlets then enter the second modulator, later referred to as electro optical amplitude modulator (EOAM), again at a 45 degree angle. This modulator is used as a binary amplitude modulator either maintaining the polarization state or rotating it by 90 deg. The two beamlets then pass a second BD oriented orthogonal to the first one. If the polarization state was rotated this again displaces the previously shifted beamlet. Otherwise it displaces the unshifted

beamlet. This enables to switch between either two horizontally displaced beamlets or two vertically displaced beamlets in the BFP.

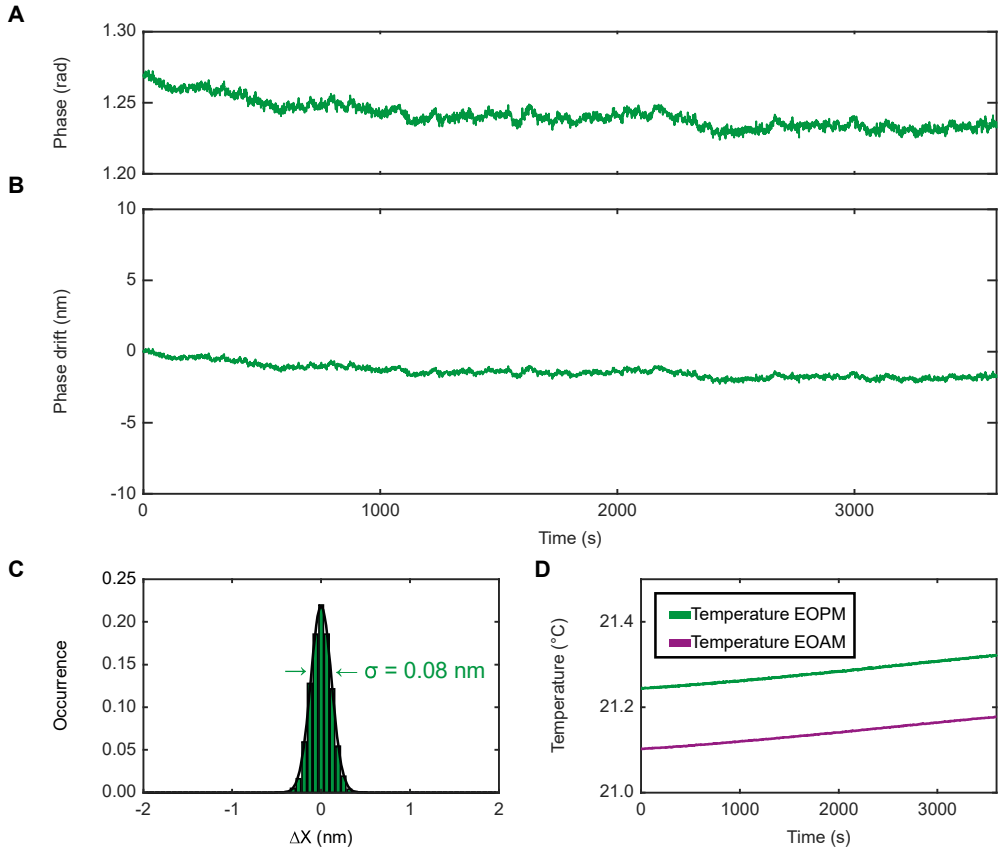

Figure 3.4: **Drift of the intensity minimum over the course of 1 h due to phase drift** as measured from the intensity profile on a camera in a plane equivalent to the FP. **(A)** Phase drift in radiant, evaluated by the Fourier transformation of the intensity profile along the axis of intensity modulation. **(B)** Position drift calculated from the phase, translated into the FP of the objective. **(C)** Population normalized histogram of the differences between adjacent positions together with a Gaussian fit yielding a underlying short-term localization precision of 0.08 nm. **(D)** Temperature close to the two electro-optical modulators during the course of the measurement.

Please note that other ways of generating four beamlets with variable phase and amplitude are possible. This implementation however is irreducible in terms of electro optical components, as the lowest degrees of freedom for the phase modulator are two (switching between x/y and controlling the phase) and each degree of freedom has to be controlled by one active device. Therefore presumably not much more compact implementations are possible. The increased compactness also permits all beamlets to pass through the same optical components. This not also minimizes alignment errors but also provides the best possible phase stability resulting in the low drift of the LS minimum.

In order to quantify the stability of the phase scanner, the focal intensity distribution was recorded on a camera at 5 fps over the course of one hour. By a Fourier transformation along the axis of intensity modulation, the phase was extracted at each time point and averaged to reach a time resolution of 1 s (see figure 3.4 **(A)**). Invoking the calibration described in the following section, the phase was converted into the corresponding position of the excitation pattern equivalent to the microscope focus. The extracted drift of the intensity minimum displays a below 3 nm drift with a precision of around 1 Å (see figure 3.4 **(B,C)**). Simultaneously, the temperature was recorded close to the electro-optical modulators yielding an overall increase below 0.1 K (see figure 3.4 **(D)**).

3.2.3 Calibration

The phase scanner requires calibration of the voltage to phase shift for both the amplitude and phase modulator. This is done by coupling 10 % of the beam into the calibration section of the microscope, where two cameras are placed in planes conjugated to the BFP for calibrating the EOAM and conjugated to the FP for calibrating the EOPM. For both modulators the calibration is performed by sweeping the applied voltage over a pre-defined range and simultaneously recording the corresponding camera images.

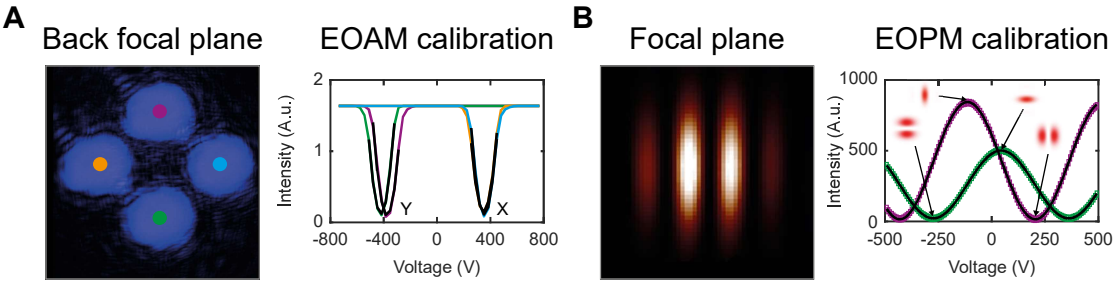

Figure 3.5: **Phase Scanner calibration curves** recorded by varying the voltage applied to the EOAM **(A)** and EOPM **(B)** and evaluating the camera images in planes equivalent to the BFP and FP respectively. Specific intensity distributions at different voltages are depicted as inlays.

For calibration of the EOAM the laser power is adjusted such that the beamlets on the BFP camera are slightly saturated. Next, camera images are recorded, while ramping the voltage applied to the EOAM from −800 V to 800 V. The positions of the four beams are identified from the stack of all images by finding the leftward and rightward center-of-mass along both line profiles though the image center. The intensity at each positions is evaluated to find the voltage with minimal intensity by a parabola fit around

the global minimum. These voltages then correspond to the two excitation patterns used for interleaved localizations in x- and y-direction.
Calibration of the EOPM is performed accordingly by setting the excitation pattern first to the LS minimum in x-direction and varying the voltage applied to the EOPM between $-500\,\mathrm{V}$ and $500\,\mathrm{V}$ and recording a stack of camera images in the FP. This stack is analyzed to find the center-of-mass and evaluate the intensity at this pixel throughout the stack. The data-points are fitted with a sin^2-function to extract the period V_π and phase V_0 of the sine. The same procedure is subsequently performed in y-direction.

3.3 MINFLUX Tracking Routine

As described in section 2.2, for each MINFLUX localization the excitation intensity minimum is, in each dimension, repeatedly addressed to positions at $[-L/2, 0, L/2]$ centered at the current molecule position estimate with the phase scanner. Based on the detected photon counts at the individual exposures, this estimate is then adjusted according to equation 2.7, which has been implemented directly on the FPGA board. For MINFLUX tracking this procedure is simply repeated, processing a pre-defined sequence of measurement parameters varying the total spacing between exposures L, the laser power and the number of repeats under these conditions. To first zoom-in on the molecule position, typically up to four MINFLUX iterations with decreasing L are performed to bring the excitation intensity minimum close to the actual molecule position. The repeats for each iteration are set between three and ten to allow centering the molecule even if single localizations have failed. Until photobleaching, all further localizations were performed with the smallest L.
As mentioned in section 2.2, for small fluorescence photon numbers and low SBR the position estimator can generate large outliers by the denominator being close to zero. To account for this and to prevent the molecule position from being lost, each localization has to pass a adjustable photon threshold and the curvature of the fitted parabola

$$b = 2/L^2\,(n_+ + n_- - 2n_0) \tag{3.3}$$

has to be positive. Finally any new position calculated by the FPGA is limited to have a maximum distance of $L/2$ to the previous position. If the calculated correction is $> L/2$, no adaption to the position is performed. The individual photon counts and the consequent molecule position estimate of each localization are transferred from the FPGA to the host computer, allowing for further post-processing.

3.3.1 Rate-limited tracking

The phase scanner is capable of addressing positions with the LS minimum at micro- to nanosecond temporal resolution. As the tracking speed is in any case rate-limited, a sufficient detection rate allows for sampling above 10 kHz, depending on the desired precision. In figure 3.6 **(A)** the recorded position of a 40 nm gold bead with 1.3 MHz detection rate with an L of 20 nm is shown. Since the central exposure, probing the emitter with the excitation minimum, does not substantially contribute to the total signal, the detection rate at outer exposures was even above 2 MHz. Sampling at 14 kHz the position was recorded with 0.6 nm precision, achieving the theoretical predicted optimum under the given conditions. During the measurement the galvo scanner was moved by 10 nm, which is apparent in the data at around 0.2 s. The extremely high STP allowed to perform an exponential fit of the form $A(1-\exp(-t/t_{rise}))$ to the data, yielding a rise-time of 0.48±0.03 ms and an amplitude of 10.20±0.02 nm. The approximate millisecond rise-time arises from inertia when suddenly rotating the mirrors. Further the measured step size is only 2 % larger than expected, which can be contributed to small calibration errors in both the galvo and the phase scanner, or might arise from sub-nanometer inaccuracies in the galvo encoders.

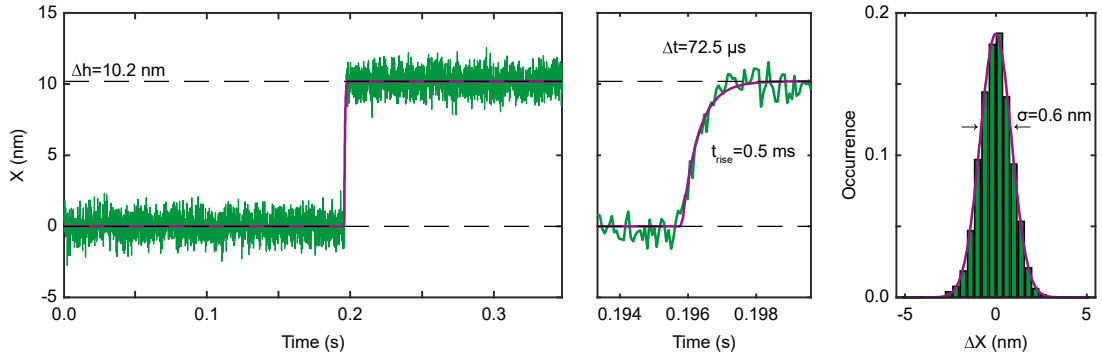

Figure 3.6: **High-speed MINFLUX tracking** of a 40 nm gold bead at megahertz detection rate. Left: Full-length MINFLUX position trace recorded at 72.5 µs temporal resolution with an L of 20 nm and detecting 100 photons per localization. At around 0.2 s the stage was moved by 10 nm. The raw data is overlaid by a exponential fit ($A(1-\exp(-t/t_{rise}))$) of the step. Center: Zoom-in of the step showing the 0.5 ms rise-time. Right: Histogram of the differences between adjacent localizations, yielding 0.6 nm precision.

The high detector count rate points towards a new technical limitation for the highest feasible tracking speed, as the APD detectors typically saturate at several megahertz. However, such emission rates are not expected for single molecules and thus those measurements will not be limited by the instrument speed, but only by the attainable emission

rate of the dyes and photobleaching. Concludingly, these high-speed measurements not only underline the extremely precise tracking potential of MINFLUX, but also highlight the stability and accuracy of the phase scanner.

3.4 Active Sample Stabilization

Coverslips coated on the objective facing side with a thin ($\sim$ 3 nm) aluminum grating were illuminated by two oppositely tilted collimated IR laser beams to actively stabilize the coverslips with sub-nanometer precision and without the need of introducing fiducial makers in the sample plane. The two beams are generated by deflecting two segments of a single beam with a specially cut glass plate and coupled into the microscope body below the objective lens with a short-pass filter. Two spatially separated images of the grating, created by reflected light of the two illuminating beams, were recorded by a camera (Basler Ace acA4112-20um, Basler AG). The tilt of the beams causes the camera images to shift laterally when moving the sample in z-direction. Because the beams are tilted in opposite directions, the individual segments shift in opposite directions, enabling direct measurement of the axial displacement. The camera frames, acquired at 20 fps, were aggregated for 500 ms before being evaluated. In doing so, the accumulated image was split in two and rotated, separating the different segments and aligning the grating with the camera axes. Mean profiles along the x- and y-direction of each segment were computed and Fourier transformed. The phase of the basic frequency component describing the grating was used to calculate the individual position of each segment. These coordinates were rotated back into the sample coordinate system and the corresponding 3D-camera drift

$$\begin{pmatrix} x_{\text{cam}} \\ y_{\text{cam}} \\ z_{\text{cam}} \end{pmatrix} = \begin{pmatrix} x_1 + x_2 \\ y_1 + y_2 \\ y_1 - y_2 \end{pmatrix} /2 \tag{3.4}$$

is retrieved from the drift of the two segments. The average lateral drift of both segments accounts for lateral drift of the pattern and the difference in drift between the segments originates from the axial displacement. To translate this camera drift into the true movement of the coverslip a calibration matrix M_{3x3} was introduced. This considers the magnification between the sample and camera plane as well as possible imperfections in the camera to stage alignment

$$\begin{pmatrix} x_{\text{sample}} \\ y_{\text{sample}} \\ z_{\text{sample}} \end{pmatrix} = M_{3x3} \begin{pmatrix} x_{\text{cam}} \\ y_{\text{cam}} \\ z_{\text{cam}} \end{pmatrix}. \tag{3.5}$$

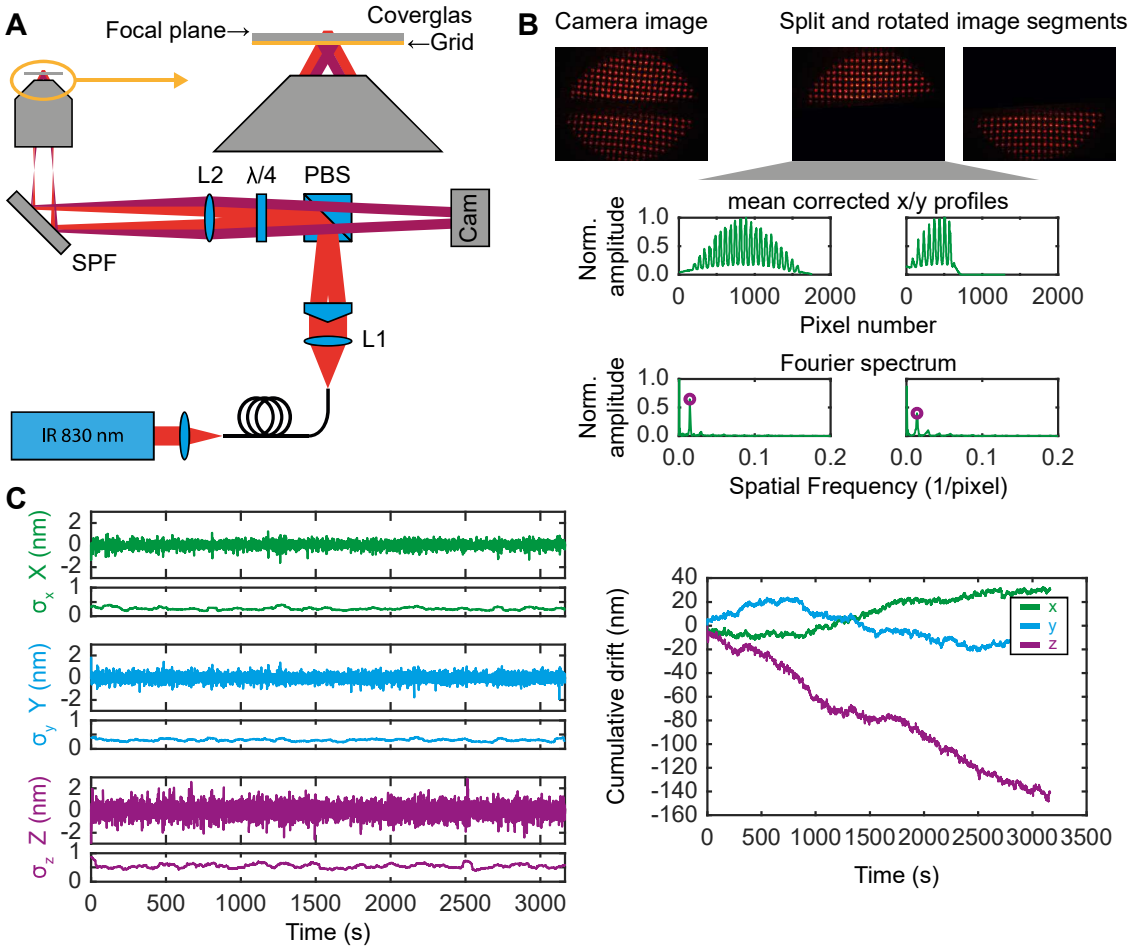

Figure 3.7: **Layout and workflow of the active stabilization unit. (A)** Light from 830 nm infrared laser diode is coupled into a single mode fiber. Afterwards the polarization is horizontally aligned by a $\lambda/2$-plate. A rooftop shaped glass plate divides the beam into two, oppositely tilted parts. Those are reflected by a polarizing beam splitter (PBS), pass a $\lambda/4$-plate (generating circular polarized light) and are focused into the BFP of the objective. Light reflected from the aluminum grid gets collected by the objective and after passing the $\lambda/4$-plate is vertically polarized. It then passes the PBS and is recorded by a camera (cam). **(B)** Workflow for extracting the 3D-position from the camera frames. (Top) Each frame is split into two segments, separating the two created images. At the same time the grid is aligned with the camera axes. (Middle) For both segments and along both axes average line profiles are calculated, which are the Fourier-transformed (bottom) to evaluate the phase at the fundamental frequency of the grid. By the grid periodicity the phases are translated into two sets of 2D-positions on the camera. The lateral sample drift is extracted from the mean x/y-drift while the axial location is given by the distance between the segments. **(C)** Left: Typical sample displacement to its target position as measured by the camera under standard measurement conditions over the course of 50 min. For each dimension the precision is evaluated by a 1 min sliding window, yielding around 0.25 nm lateral and around 0.5 nm axial precision. Right: Corrected 3D-drift throughout the measurement.

Finally a discrete low-pass filter ($x_{LP,i} = x_i \frac{dt}{RC+dt}$), depending on the recording time dt and with a decay constant of $RC = 1\,\mathrm{s}$, was applied to the correction value. This on the one hand increases the precision by a factor of three but on the other hand decreases the ability to correctly account for fast changes in the sample position. Typical drift due to changes in temperature are usually slow ($1\,\mathrm{nm\,s^{-1}}$), therefore the low-pass filter is not expected to significantly impact the quality of the stabilization.
With this approach the sample position could be maintained with a lateral precision of 0.3 nm and an axial precision of 0.6 nm (see figure 3.7). It shall be noted that possible drift of the camera itself, drift of the excitation laser beam and a phase drift between the beamlets are not accounted for. Those are mainly temperature dependent drift sources that can be reduced passively by enclosing the microscope components and thereby slowing down temperature modulations of the room itself. A true stabilization for MINFLUX and also other super-resolution techniques would comprise also actively stabilizing these parameters, not only in the sample plane but throughout the microscope. Some might be dealt with by an active temperature control, which in itself is a difficult task, since temperatures can only be controlled locally and large microscopes will comprise temperature gradients likely requiring different layers of encapsulation. Nevertheless, on short time scales ($\ll 1\,\mathrm{h}$) temperature drift should be negligible ($\ll 1\,\mathrm{K}$, for example see figure 3.4), making a movement of the sample relative to the objective the main source of drift.

Chapter 4

Single Molecule Tracking Experiments

Characterizing the MINFLUX microscope described in chapter 3, surface-immobilized single fluorescent ATTO 647N molecules were repeatedly localized to extract the achievable localization precision of stationary emitters and to demonstrate the ability to follow a pre-defined trajectory imposed by moving the piezo-electric stage. These measurements represent a close to ideal case for localizing single emitters, as ATTO 647N is well known for its high brightness and photostability and the sample can be prepared introducing minimal background. They therefore set a baseline for the achievable performance of later experiments in terms of PIC and position accuracy. The surface-immobilization follows a protocol similar to [50], that has been optimized for single molecule experiments by Lukas Scheiderer[1]. The localization and tracking of single molecules with the phase scanning MINFLUX approach, is also included in the submitted manuscript (see Publications).

4.1 Surface-Immobilization of ATTO 647N

To minimize background from contaminated surfaces and optimize the surface coating by removing fatty contaminations, coverslips (170 µm, No 1.5H, Paul Marienfeld GmbH & Co. KG, Lauda-Königshofen, Germany) were sonicated in isopropanol and afterwards rinsed with milli-Q water. Then, a flow chamber was constructed to enable an uncomplicated medium exchange by attaching the coverslip to an objective slide with double-sided adhesive tape (Scotch Double Sided Tape, 3M, Saint-Paul, USA). The chambers were incubated for 15 min with a pre-mixed solution of $0.2\,\mathrm{g\,L^{-1}}$ biotinylated poly-

[1] Max-Planck Institute for Medical Research

L-lysine-polyethylene-glycol (PLL-PEG-bt) solution (PLL(20)-g[3.5]-PEG(2)/PEG(3.4)-biotin, Susos AG Inc.) with 1 % (v/v) Tween 20 (P9416, Sigma Aldrich). After rinsing with 60 µL of a phosphate buffer saline (PBS) solution, the chamber was incubated with 10 µg/ml neutravidin (NVD; 31000, Thermo Fisher) in PBS for 5 min and rinsed again with 60 µL PBS.
The 1 mM stock solution of biotinylated ATTO 647N (AD 647N-71, ATTO-TEC) was sonicated for 15 min before diluting it in PBS to a final concentration of 1 fM in order to achieve single molecule conditions in the sample. The diluted fluorophore was then flushed into the flow chamber and incubated for 5 min, before rinsing a final time with PBS. An imaging buffer (1 mM methyl viologen (75365-73-0, Sigma Aldrich), 1 mM ascorbic acid (50-81-7, BioVision Inc.) in PBS) was added before conducting measurements to reduce the time the fluorophore spends in its non-fluorescent triplet state, thereby increasing the fluorescence rate and decreasing photo bleaching. Finally the flow chamber was sealed with picodent twinsil speed 22 (picodent Dental-Produktions- und Vertriebs GmbH) to prevent evaporation of the imaging medium.

4.2 Data Analysis

Online- and post-processing of MINFLUX position traces was programmed in LabView 2019 by directly processing the data transferred from the FPGA. For further evaluation individual traces were exported, containing the re-evaluated position estimate and the individual photon counts of each exposure. Processing and evaluation of traces, like determination of the localization precision, was performed in custom-written matlab scripts.

4.2.1 Fixed-Curvature Estimator

For the surface immobilized ATTO 647N molecule the MINFLUX position estimate was re-calculated employing a so called fixed-curvature estimator (FCE). This is based on the assumptions that all localizations are generated by the same parabolic excitation profile and the brightness of the fluorophore is constant. Then, the curvature of the excitation intensity profile can be derived from the average curvature

$$\langle b \rangle = \frac{2}{KL^2} \sum_i \left(n_{+,i} + n_{-,i} - 2n_{0,i} \right) \tag{4.1}$$

of all K localizations. Substituting equation 4.1 into equation 2.7 results in the FCE

$$x_{\mathrm{FCE}} = \frac{n_- - n_+}{2\langle b \rangle L}, \tag{4.2}$$

which is highly efficient in terms of retrieving the optimal precision, especially for low photon numbers. However, for traces where the total number of detected photons per localization changes, due to for a example a changing detection efficiency at different positions relative to the detection pinhole, this estimator is not applicable. A comparison between the FCE and the GLSE is given in section A.3.

4.2.2 Estimation of the Localization Precision and SBR

To extract information about the tracking precision σ and the SBR of each trace, they were loaded into matlab. Instead of simply calculating the spread of localizations, which would comprise small remaining drift or disturbances and therefore rather represent an imaging precision, the tracking precision was estimated by evaluating the differences between consecutive localizations $\Delta_i = x_{i+1} - x_i$. As each position x_i originates from a normal distribution with spread σ, the differences will also form a normal distribution but with spread $\sqrt{2}\sigma$. The underlying tracking precision can hence be extracted by fitting the distribution of distances with a Gaussian function and dividing the spread by $\sqrt{2}$.
The average SBR can directly be evaluated from the mean photon counts of the three exposures

$$SBR = \frac{n_+ + n_-}{2n_0} - 1. \tag{4.3}$$

4.2.3 Step-Finding Algorithm

The MATLAB function *ischange* was used to detect steps in MINFLUX position traces. It performs an iterative change point search [51] minimizing the objective function

$$\sum_{i=1}^{m+1} \left[C(x_{\tau_{i-1}+1:\tau_i}) \right] + \beta m \tag{4.4}$$

for m steps, with a cost function C for individual segments i separarated by changepoints τ and a penalty factor β for adding single steps. Typically the residual sum of squares (RSS) is used as the cost function. For traces with a constant mean, adding an artificial step would cause a RSS reduction close to σ^2 (see section A.4). This can be used to control the overfitting rate by choosing the penalty factor according to σ.
To select a sufficient scaling, numerical simulations with different noise levels, trace lengths and a penalty factor between $1\sigma^2$ and $20\sigma^2$ were performed (see figure 4.1). The simulations in **(A)** entail different magnitudes of normally distributed noise level for 5000 traces of 500 data points with constant mean, whereas in **(B)** the trace length N was varied

while keeping the noise level constant. The number of traces generated was adjusted such that the total number of data points is kept constant. For both cases the *ischange* function was applied while changing the penalty factor. The overfitting rate was determined as the number of artificial steps per data point. The simulations confirmed no significant dependence between the overfitting rate and the localization precision or the total number of data points, validating the simple quadratic scaling between the penalty factor and the localization precision. The overfitting rate yet depends strongly on the penalty factor itself. Choosing the penalty factor as $12\sigma^2$ results in $< 0.01\,\%$ overfitting (one false positive step per 10,000 localizations) which should be sufficient to exclude any noise based overfitting. As described in section 4.2.2, the localization precision of individual traces can be estimated without any prior knowledge about steps, which enables choosing the penalty factor accordingly.

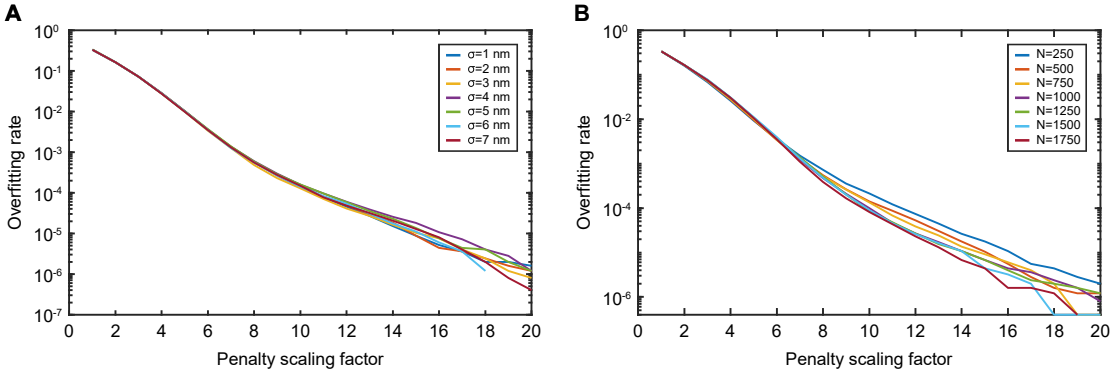

Figure 4.1: **Numerical simulations of the overfitting rate** for various penalty factors. **(A)** Semi-logarithmic plot of the overfitting rate as a function of the penalty factor for different noise level. 5000 traces of 500 data points with constant mean and the specified noise level were generated and subjected to the *ischange* function of matlab, varying the penalty factor proportional to the noise level. **(B)** Semi-logarithmic plot of the overfitting rate as a function of the penalty factor for different trace lengths N. For each trace length the number of traces that were genreated was adjusted such the total number of datapoints stayed constant. All traces have constant mean and a noise level of 1 nm and were subjected to the *ischange* function of matlab, varying the penalty factor proportinal to the noise level.

The detected step function is further edited by first employing a moving median filter to remove steps originating from spikes in the data and second by removing steps of step sizes smaller than a certain threshold. The width of the moving median filter was set to 9 to remove any spikes of width four or smaller. Note that this filtering does not remove short plateaus of progressive movement. As steps imposed by the piezo-electric stage were programmed to be 10 nm, the step size threshold was set to 5 nm.
To benchmark the limitations of the step finding algorithm, the probability of detecting an intermediate plateau between two steps of a given step size was numerically evaluated.

At a given localization precision σ, 256 traces with a temporal resolution of 0.6 ms were generated, each including two successive steps of a fix step size of 4 nm, 8 nm or 16 nm and varying temporal separation. Each trace then was subjected to the step-finding algorithm with the moving window size being set to nine and the minimal step size being set according to the simulated step size. The intermediate plateau was counted as detected if the algorithm had found exactly two equally directed steps. The resulting plateau detection probability is given in figure 4.2. For a constant step size-to-σ-ratio of two, the step-finding algorithm detected nearly all plateaus, if they were longer than 8 ms. If the ratio was set to four, even plateaus as short as 2 ms were reliably detected. Overall the plateau detection probability will not only depend on the step size, σ and the duration of the plateau but also on the temporal resolution of the data. This is comprehensible, as changes in the mean can more easily be detected when averaging more data points. However, as most MINFLUX measurements are performed with a temporal resolution of ~ 0.6 ms, no large deviation from the simulated detection probability is expected.

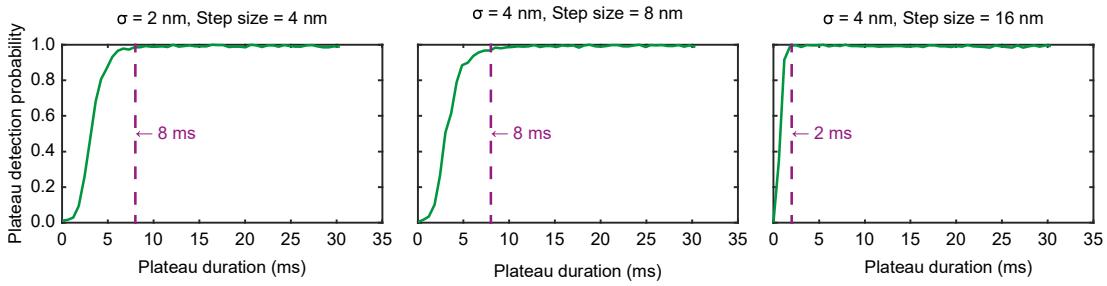

Figure 4.2: **Numerical evaluation of the plateau detection probability** for different step sizes and noise level. 256 traces with a position noise σ were generated, including two steps of a given size with a varying temporal spacing. The traces were subjected to the step-finding algorithm and it was evaluated, whether two equally directed steps were detected. The rough dwell time at wich confidently above 95 % of intermediate plateas was detected, is depicted by the purple dashed lines.

4.3 Localizing Surface-Immobilized Emitters

Surface-immobilized ATTO 647N molecules were pre-localized by confocally scanning a $10\times10\,\mu m^2$ FOV with 50 nm pixel size and identifying single emitters with an iterative spot-searching algorithm. The galvanometer scanner then sequentially addressed these positions to perform the MINFLUX tracking measurements with a final L of either 30 nm or 16 nm (see section 3.3). The exposure time at each probing position was set to 100 µs, which combined with a 5 µs waiting-time for switching between exposures and 500 ps for

calculating the new position estimate results in 631 µs for a complete 2D-localization.

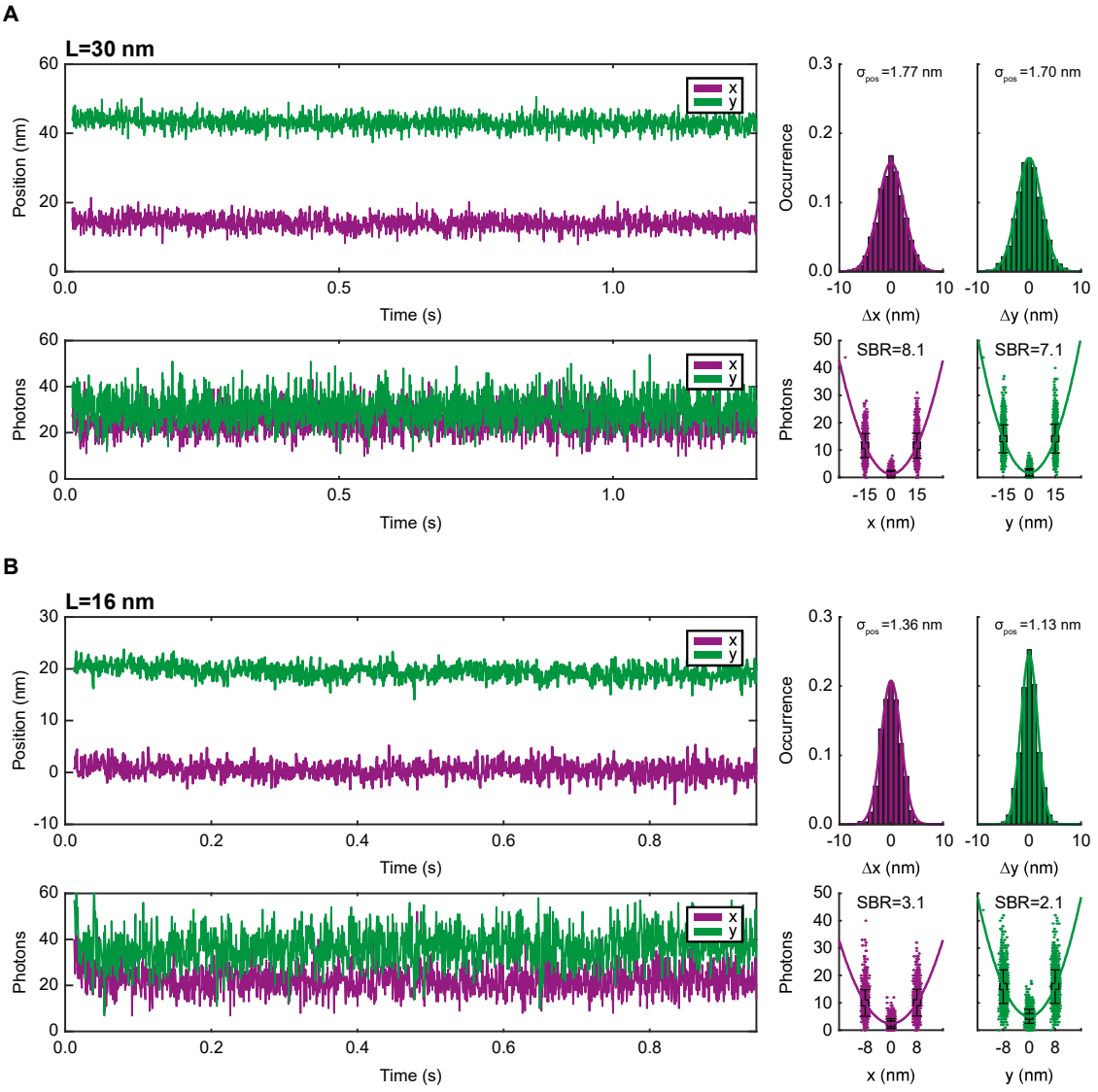

Figure 4.3: **Tracking data of single surface-immobilized ATTO 647N molecules** recorded with an L of 30 nm **(A)** and 16 nm **(B)**. (Top) Each panel shows the x position (purple) and y position (green) as well as the histogram of differences between adjacent localizations. (Bottom) Further the total number of photons used for each localization and the photon distribution of the individual three exposures are given.

Individual position traces were filtered and screened in LabView 2019, before exporting a manual selection based on a good SBR. Filtering was done by requiring a minimum of five detected photons per localization in each dimension to exclude background, a maximum of 60 detected photons per localization in each dimension to exclude multiple emitters and at least ten successive localizations surpassing the minimum photon threshold.
In figure 4.3 two exemplary traces, recorded with an L of 30 nm (**A**) and an L of 16 nm

(**B**), displaying a high SBR, are shown. Each panel displays the position and photons recorded in x- and y-direction over time (left) and the corresponding histogram of differences between neighboring localizations as well as a Gaussian fit to the data (right). Further the recorded photons are separated by their corresponding exposure and are depicted together with the estimated parabola relative to the molecule position. Following the procedure described in 4.2.2, yields a localization precision for $L = 30\,\text{nm}$ of 1.77 nm in x-direction and 1.70 nm in y-direction, at only around 30 detected photons and a SBR above seven in both dimensions. This is close to the theoretical limit of 1.61 nm given by equation 2.10 indicating that the remaining position noise is mostly limited by the photon noise. The trace recorded with $L = 16\,\text{nm}$, yielded a localization precision of 1.36 nm in x-direction and 1.13 nm in y-direction, also utilizing only around 20 to 40 detected photons. For the trace shown, the SBR was above two, which results in a best possible precision of 1.02 nm, still very close to the measured value.

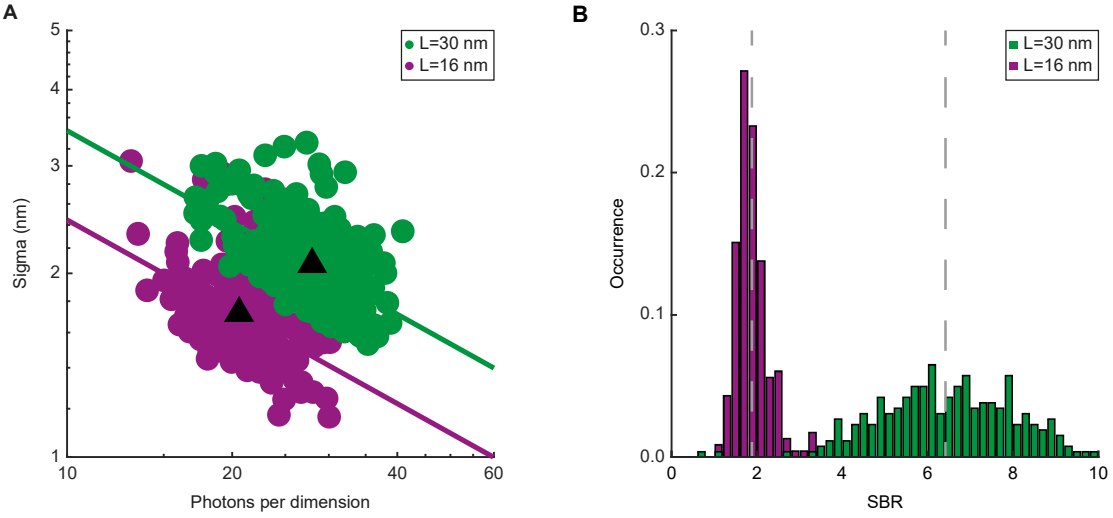

Figure 4.4: **Localization precision and SBR of single surface-immobilized ATTO 647N molecules. (A)** Localization precision of individual traces along a single dimension for $L = 30\,\text{nm}$ (green, 263 traces) and $L = 16\,\text{nm}$ (purple, 232 traces) together with a fit of L_{eff} by equation 2.10. The mean precision and mean photon counts are depicted by black triangles. **(B)** Population normalized histograms of the SBR together with the mean SBR depicted by the grey dashed line

In total 263 traces at $L = 30\,\text{nm}$ and 232 traces at $L = 16\,\text{nm}$ were processed concerning their localization precision σ, their mean fluorescence photon count (figure 4.4 **(A)**) and their SBR (figure 4.4 **(B)**). The localization precision, photon counts and SBR were estimated in x- and y-direction separately and finally averaged to represent the mean performance along a single dimension. For both L, a σ of 2 nm was achieved, consuming as little as 30 photons. By employing the average SBR, equation 2.10 was fitted to the

measured localization precision to retrieve an effective displacement L_{eff}. This parameter was in both cases around 20 % larger than the true L. Anyway, an increased L_{eff} is expected since any disturbances will cause the localization precision to decrease thereby shifting L_{eff} to larger values. The best precision per given number of detected photons achieved for individual molecules reaches the theoretical optimum.
As the achieved localization precision with $L = 16\,\text{nm}$ is higher than for $L = 30\,\text{nm}$, this might suggest picking the smaller L for tracking measurements. However the also reduced SBR makes individual localizations much more susceptible to varying background contributions and fluorophore brightness. Therefore, a moving object will not necessarily perform equally to stationary emitters and might not create sufficient contrast to allow measurements with the smallest L. Nevertheless, these measurements show the enhanced performance of phase scanning MINFLUX over conventional, donut-based MINFLUX implementations and especially when compared to camera-based techniques.

4.4 Tracking Surface-Immobilized Emitters

To characterize the tracking capabilities of the phase scanning MINFLUX approach in terms of spatial precision, accuracy and temporal resolution, surface-immobilized ATTO 647N molecules were moved by the piezo-electric stage while tracking. First, molecules were moved on a circular trajectory with 15 nm radius and a 2 Hz repetition rate. The molecule position was recorded with $L = 30\,\text{nm}$ at 631 µs temporal resolution for around 1.2 s, as shown in figure 4.5 **(A)**. Each localization is depicted in a 3D-scatter plot with the third dimension denoting time. The data-points are overlaid with the estimated stage trajectory (red line) retrieved from sinusodial fits of the x- and y-position. The fitted diameter ($D_x = 29\,\text{nm}, D_y = 30\,\text{nm}$) and the estimated repetition rate ($f_x = f_y = 1.99\,\text{Hz}$) are in good agreement with the programmed stage movement, highlighting the high accuracy of the method. Under these conditions a SBR of eight was achieved in x-direction and a SBR of four in y-direction, yielding an average localization precision of 1.84 nm at only 30 detected photons per dimension, in no way falling short of the precision achieved with stationary emitters.
Besides following a continuously moving object, the MINFLUX microscope was being challenged by abrupt changes when moving the stage back and forth in a stepwise manner. Five steps of 10 nm were performed in the same direction with 100 ms waiting time in-between steps, before changing to the opposite direction. The position of the fluorescent molecule was again recorded with $L = 30\,\text{nm}$, this time at 607 µs temporal resolution for around 2.5 s (see figure 4.5 **(B)**). The localizations are depicted as before, resolving the individual plateaus, as evident from the temporally color coded xy-scatter plot. For

the trace shown the localization precision was calculated to be 1.64 nm at on average 35 detected photons per dimension and an SBR of 5 in x-direction and 6 in y-direction, again matching the expected precision close to the theoretical limit.

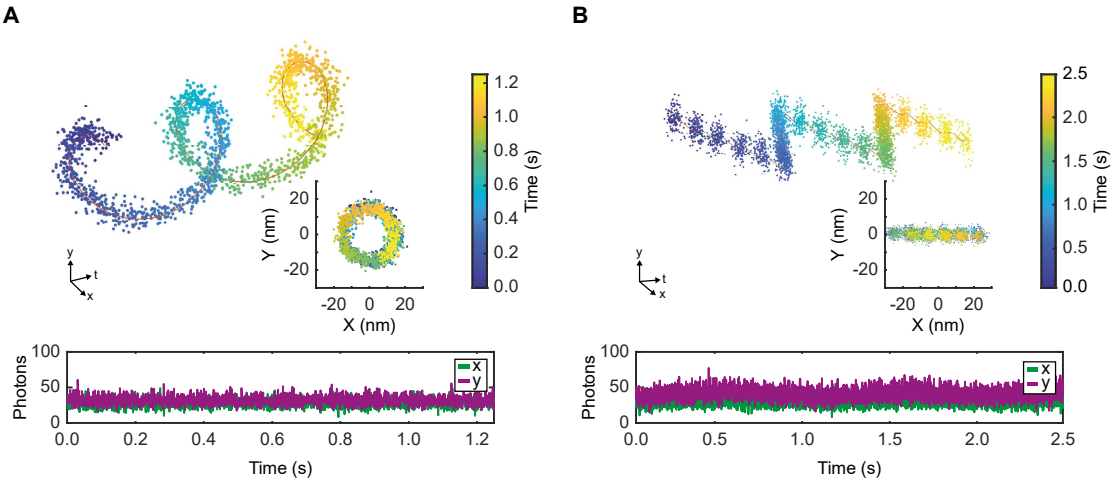

Figure 4.5: **Position tracking of single surface-immobilized emitters.** **(A)** 3D-scatter plot of the lateral position of a single surface-immobilized ATTO 647N molecule over time. The fluorescent molecule was moved by the piezo-electric stage on a circular trajectory with radius 30 nm at a frequency of 2 Hz. The recording time is additionally color-coded. The inlay scatter plot shows the lateral position with the same temporal color-coding. The corresponding photon counts over time are given in the bottom plot. **(B)** same as in (A) but this time the ATTO647N molecule was moved in a stepwise manner each 100 ms with 10 nm stepsize.

In order to identify the individual steps, the position trace was subjected to the step-finding algorithm described in section 4.2.3 with a minimum step size of 5 nm. The retrieved step-function was overlaid with the 3D-scatter plot (red line) and used to analyze the measured trajectory and quantify its accuracy. First the dwell times between steps and the stepsizes were evaluated from the step-function and displayed as histograms in figure 4.6 **(A,B)**. As evident from panel **(A)** most steps were separated by around 100 ms as expected. However, some steps also were separated by only a few milliseconds, a feature that combined with the observed stepsizes around 5 nm (see figure 4.6 **(B)**) originated from the algorithm splitting single steps into two. The reason for this apparent overfitting is the finite rise-time it takes the stage to address its new position. This becomes evident when averaging all aligned position traces from single steps (see figure 4.6 **(C)**). Evaluating the step motion with an exponential-fit of the form $A(1 - \exp(-t/t_{rise}))$, yielded a rise-time of around 4 ms, which, based on the noise, can be sufficient to be detected by the step-finding algorithm. This rise time was around three orders of magnitude slower than any electro-optical response time of the microscope, thereby discarding the possibility of microscope induced errors, even at millisecond timescales. Further, closer observation re-

vealed that the measured average stepsize was around 9.5 nm, smaller than the expected 10 nm. This five percent deviation can at least partly be caused by the finite encoder precision of the piezo-electric motors and hysteresis effects originating from the fraction occurring, when moving the stage back and forth. On the other hand, calibration errors in the single percentage range are inevitable, since any potential systematic errors in the ruler will become inherent to following measurements.

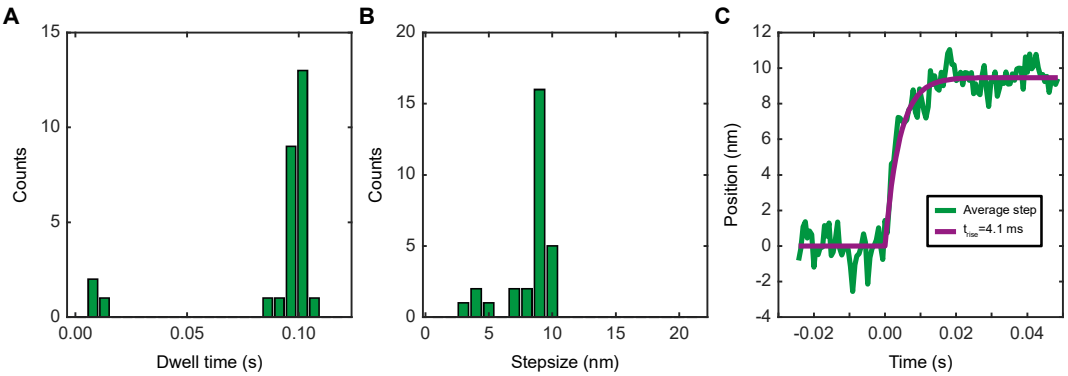

Figure 4.6: **Detailed evaluation of the stage stepping trace. (A)** Histogram of the dwell times between steps detected by the step-finding algorithm. **(B)** Histogram of the stepsizes detected by the step-finding algorithm. **(C)** Average position trace of a single step (green) overlaid with a exponential fit of the form $A(1 - \exp(-t/t_{rise}))$.

4.5 State of the Art MINFLUX Tracking

The preceding chapter demonstrated the precision and accuracy of the phase scanning MINFLUX implementation featured in this thesis. Localizing single, surface-immobilized ATTO 647N molecules with an L of 16 nm, demonstrated below 2 nm precision at only around 20 detected photons per localization and dimension. The PIC of these measurements was about three times higher compared to previous MINFLUX studies [17] and ten times higher compared to FIONA [18]. Note that since the precision scales with the inverse square root of the number of photons, this translates into a reduction of the number of photons needed to reach a given precision by a factor of ten and 100, respectively. At an L of 30 nm, a similar precision was reached requiring the average detection of 30 photons per localization and dimension, still yielding an around nine-fold increase in the PIC compared to camera-based tracking. The improvement in comparison to previous MINFLUX tracking studies can predominantly be explained by the reduced L, facilitated by the steeper intensity minimum of the LS minimum. Still, the mean evaluated precision was for both L around 20 % larger than the predicted optimal precision achievable.

This is not surprising, since any additional fluctuations in the data, that are not solely due to photon statistics, will increase, but never decrease, the position noise and thereby reduce precision. Those additional fluctuations can be caused by vibrations of the stage, a significant linker flexibility or small-scale position jitter of the excitation beam. While those contributions have been thoroughly minimized, they might still cause observable contributions at up to the nanometer scale.

Moving single emitters on a pre-defined trajectory with the piezo-electric stage and recording their trajectory with an L of 30 nm and 0.63 ms temporal resolution, validated no reduction in the achieved localization precision or PIC. The evaluated tracking precision was around 1.7 nm at 30 - 35 detected photons per localization and dimension, outpacing camera-based tracking techniques of single molecules with nanometer precision by two orders of magnitude. In the course of following a continuous circular trajectory and a stepwise back-and-forth motion, above 95 % accuracy in reference to the movement of the stage was demonstrated. Since on these scales hysteresis effects or imperfections of encoders distort the calibration, accomplishing higher accuracies is only possible by employing more precise references, with in themselves nearly perfect scaling. This inherently becomes more and more complicated as those devices again need even more accurate devices for verification.
Further, tracking the abrupt changes in the stage position, MINFLUX disclosed a 4.1 ms rise time of the piezo-motors at a step size of 9.5 nm, highlighting the ability to measure detailed nanometer-sized motion of a single fluorescent molecule at the millisecond timescale.

Chapter 5

MINFLUX Tracking of Kinesin-1

The demonstrated high spatial precision and temporal resolution of phase scanning MINFLUX tracking was utilized to investigate the stepping behavior of kinesin in an extensive *in vitro* study. Kinesin is a homo-dimeric motor protein responsible for anterograde axonal transport of vesicles along microtubules and various other cellular functions [52], that has long and broadly been studied both *in vitro* and *in vivo*. Each monomer consists of a catalytic motor domain (head), coupled, via the so called neck linker, to an α-helical neck domain [53]. At this region, the monomers interconnect and their neck domains form a coiled-coil domain [54], which binds cargo. A schematic drawing of kinesin, with its heads bound to a microtubule protofilament, is shown in figure 5.1 **(A)**. By consuming the energy of a single ATP [41], the heads take alternating 16 nm steps along single microtubule protofilaments to the next free binding site in a hand over-hand-manner [18] (see figure 5.1 **(B)**). Thereby the protein coiled-coil domain, and thus the transported cargo, is moved in the same direction by 8 nm [39, 41], generating forces in the range of a few piconewton [53]. As the amount of ATP controls the number of steps kinesin takes, the walking speed depends on its concentration. However, at physiological ATP concentrations of 0.5 mM to 5 mM [55], for which the binding kinetics are saturated, the speed maxes out at above $600\,\mathrm{nm\,s^{-1}}$ [41]. The overall chemical cycle of kinesin comprises binding of ATP to a single head, followed by hydrolization of ATP to adenosine 5'-diphosphate (ADP) and a remaining phosphate at the same head. Sequentially, this phosphate and ADP are then released leaving the head in an empty, so called apo state [56].

An important study, visualizing the motion of individual heads with camera-based position detection, disclosed the discrete 16 nm steps, labeling with only a single Cy3 fluorophore [18]. Achieving the desired 1 nm precision required the detection of more than 4000 photons at sampling times of 330 ms. Thus, the walking speed of kinesin needed to be substantially slowed down to around one step per second at 340 nM ATP concentration

to resolve individual steps.
Additionally, indirect studies of the head motion by Förster resonance energy transfer (FRET), measuring the distance between a donor and an acceptor fluorophore, each attached to one head, strongly suggested that individual 16 nm steps actually include a succession of two 8 nm substeps [57, 58]. By the same studies, this intermediate state was shown to be ATP-dependent, but a clear interpretation of this state in the context of the mechanochemical cycle of kinesin still lacked information about the motion of individual heads.
Since these early studies, the STP of kinesin tracking has been substantially improved, by employing light scattering of beads attached to the kinesin head. Thereby, for the first time, the 8 nm substeps to and out of an intermediate unbound state of the labeled head could be directly observed [59, 60], even at physiological ATP concentrations. Strikingly, although labeling with similar sized beads, two opposing explanations of the mechanochemical reason behind these substeps emerged. One study concluded that the intermediate state is awaiting ATP binding [59], whereas the other derived that ATP is hydrolized in the intermediate state [60].
As recently as 2021, substeps have also been clearly resolved by tracking of the coiled-coil domain, utilizing newly developed germanium nanospheres for optical trap measurements [42]. Further, due to the application of forces, this study proposed that upon detaching from microtubules, kinesin, at first, enters a so-called slip state. During this, the heads are not bound to the microtubule surface, but only weakly associated. This enables kinesin to rebind and rescue its mobility.
Besides the plethora of research articles published about kinesin, the intertwining of biochemical reactions and mechanical motion remained unsolved. In addition to the previously mentioned controversy over the role of the intermediate state in the mechanochemical cycle [61], a debated question is, whether kinesin walks in a symmetric hand-over-hand manner, causing a unidirectional rotation of the coiled-coil domain [62] and therefore torsion, or if the heads pass each other on alternating sides in an asymmetric hand-over-hand walking behavior [63, 64]. Despite the continuous improvement towards smaller-sized beads for labeling and the breakthroughs of scattering based techniques, some of these ambiguities might inherently originate from the still comparably large labels (200 times the volume of the kinesin head) altering or obscuring the true motion of the protein [65].

By switching back to a small, considerably less invasive fluorescent dye for labeling, MINFLUX is well suited for tackling these open questions. Its STP of nanometer precision and millisecond temporal resolution is sufficient to study the stepping motion of both the coiled-coil domain and the heads under load- and force-free conditions. This work presents MINFLUX as the first and so far only single molecule tracking technique that is capable of visualizing substeps (*in vitro*), even at physiological ATP concentrations. The

data presented in this chapter is also available as preprint (see Publications).
Note that in parallel to this thesis, MINFLUX tracking of kinesin in live cells has been realized [66] with a commercial MINFLUX microscope. The results of this study have been published as a not peer-reviewed preprint and will be discussed further below.

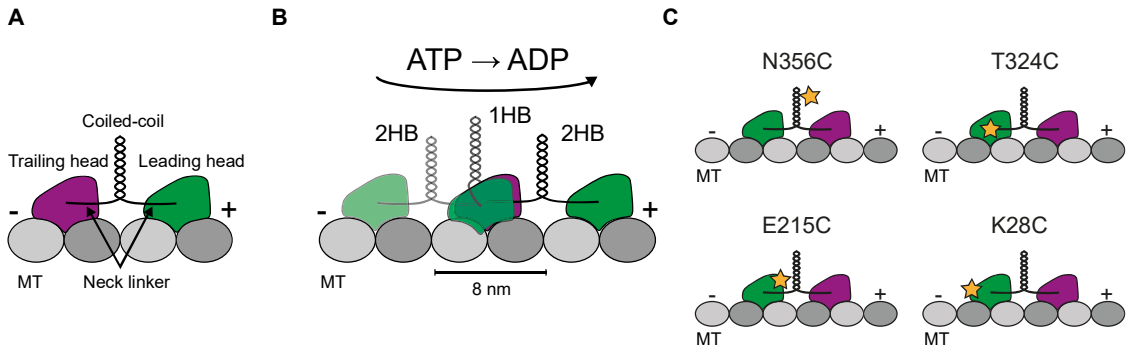

Figure 5.1: **Sketch of kinesin walking on microtubules** and labeling positions of different constructs used in this thesis. **(A)** Kinesin binding to microtubules (MT) with its leading and trailing head. The heads are connected via a neck linker to the interconnecting coiled-coil domain. **(B)** Sketch of kinesin walking along microtubule protofilaments by detaching with the trailing head and entering a one-head-bound (1HB) intermediate state, before completing the full 16 nm step and being again bound to the microtubule surface with both heads (two-head-bound, 2HB). The process of a full step consumes one ATP. **(C)** Sketch of the labeling positions of the constructs used in this thesis. The label is located at the coiled-coil domain (N356C) or at various positions on the head (T324C, E215C, K28C).

The following sections describe the protocols for preparing the samples, recording the data and processing them. Afterwards, MINFLUX tracking of kinesin, labeled at the coiled-coil domain, is presented, followed by an exhaustive investigation of the substep behavior of different protein constructs labeled at various positions on the kinesin head. The use of the model protein kinesin was proposed by Lukas Scheiderer (L. S.)[1]. L. S. also did the labeling design, as well as establishing, optimizing and preparing samples. The adaptation of measurement routines, to enable the MINFLUX recording of kinesin traces, the data recording itself and the creation of sophisticated evaluation software were performed by Jan Otto Wolff (J. O. W.). The data were evaluated and discussed by L. S. and J. O. W., whereas L. S. provided a biochemical and J. O. W. a physics and mathematical view-point.

[1] Max-Planck Institute for Medical Research

5.1 Preparation of *In Vitro* Samples

Kinesin was labeled via maleimide coupling at individual amino acid positions point-mutated to cysteines at the coiled-coil domain (N356C) or at various positions on the head (T324C, E215C, K28C). To specifically label a single cysteine, all other solvent-exposed cysteines were removed via site-directed mutagenesis.

5.1.1 Expression of Point-Mutated Kinesin

Cysteine-light truncated (amino acid position 560) human kinesin-1 constructs were expressed in E. coli with different plasmids (see Table 5.1). Point mutations were introduced via QuikChange site-directed mutagenesis (employing PfuUltra HF polymerase (600380-51), Agilent) [67]. All plasmids were checked by DNA sequencing. For labeling, each construct featured a different single solvent-exposed cysteine and a C-terminal His6-Tag for purification (via 5 mL HisTrap FF (GE17-5255-01, Cytiva)). The proteins were aliquoted in 25 mM piperazine-N,N'-bis(2-ethanesulfonic acid) (PIPES; P-1851, Sigma Aldrich) pH 6.8, 2 mM MgCl2 (1.05833.0250, Merck), 1 mM ethylene glycol-bis(2-aminoethylether)-N,N,N',N'-tetraacetic acid (EGTA; E3889, Sigma Aldrich), 0.1 mM ATP (BP413-25, Fisher Scientific), 0.2 mM TCEP (J60316, Alfa Aesar), $\sim$ 300 mM NaCl (1.06404.1000, Sigma-Aldrich) and 10 % (m/v) sucrose (S1888, Sigma Aldrich), then flash-frozen in liquid nitrogen and afterwards stored at 80°C.

Table 5.1: **List of kinesin plasmids** containing the plasmid name, the amino acid position of the single solvent-exposed cysteine, an approximate location of the label and the provider of the plasmid.

Plasmid	**Amino acid position**	**Approximate label position**	**Provider**
K560CLM T324C	aa324	head, center right	Addgene (# 24460)
K560CLM E215C	aa215	head, front	Yildiz Lab (University of California, Berkeley)
K560CLM K28C	aa28	head, back	produced from CLM RP HTR (# 24430, Addgene)
K560CLM N356C	aa356	coiled-coil domain	produced from CLM RP HTR (# 24430, Addgene)

5.1.2 Maleimide Labeling of Kinesin

ATTO 647N maleimide (AD 647N-41, ATTO-TEC) was used to label kinesin over night at 4°C. The reaction mixture was cleared from leftover dye by size-exclusion chromatography (PD MiniTrap G-25, 28-9180-07, Cytiva), following the manufacturer's protocol. Employing UV-Vis spectroscopy (DS-11+ Spectrophotometer, DeNovix) and mass spectrometry (ESI, maXis II ETD, Bruker) were used to determine the degree of labeling (DOL) ensuring that each dimer carried at most one fluorophore. The labeled protein was mixed with sucrose in a concentration of 10 % (w/v) and aliquots were flash-frozen in liquid nitrogen and stored at -80°C.

5.1.3 Preparation of Microtubules

Microtubules were polymerized from 88 % cycled tubulin (032005, PurSolutions, LLC), 10 % biotinylated tubulin without a fluorophore (033305, PurSolutions, LLC) and 2 % biotinylated tubulin labeled with Alexa Fluor 488 (048805, PurSolutions, LLC). PEM80 buffer (80 mM PIPES, 0.5 mM EGTA, 2 mM MgCl2, pH 7.4) with 1 mM guanosine-5'-[(α, β)-methyleno]triphosphate (GMPCPP; NU-405S, Jena Bioscience) was used to suspend the lyophilized tubulin variants for 30 min at 37°C. After incubation, the polymerized microtubules were centrifuged at 21,000x g in a bench-top microcentrifuge (Fresco 21, Thermo Scientific) for 15 min. Then, microtubules were washed with PEM80 and again centrifuged at 21,000 × g for 15 min. Microtubule pellets were resuspended in PEM80 before being aliquoted, flash-frozen in liquid nitrogen and stored at -80°C.

5.1.4 Sample Preparation

A flow chamber with PLL-PEG-bt / NVD surface functionalization was prepared, as described in section 4.1, incubated with diluted microtubules (in PEM80 with 10 mg L^{-1} cabazitaxel (FC19621, Biosynth Carbosynth) in PEM80) for 5 min, rinsed with PEM80 and afterwards incubated with biotinylated bovine serum albumin (BSA-bt100 µg mL^{-1} in PEM80, BSA-bt; A8549-10MG, Sigma Aldrich) for 5 min to saturate free binding sites. Then, the flow chamber was rinsed with PM15 buffer (15 mM PIPES, 2 mM MgCl2, pH 7.4). Labeled kinesin was pre-mixed with the measurement buffer containing 1 mM 1,4-dithiothreitol (DTT; 6908.1, Carl Roth), 1 mM paclitaxel (10-2095, Focus Biomolecules), 10 µg mL^{-1} BSA-bt, 1 mM methyl viologen (75365-73-0, Sigma Aldrich), 1 mM ascorbic acid (50-81-7, BioVision Inc.) and 10 µM/100 µM/1 mM ATP (A3377-1G, Sigma Aldrich) or 1 mM of the slowly hydrolizing ATP-analog ATPγS (NU-406-5, Jena Bioscience) in

PM15 buffer and added to the flow chamber in an InvivO2 Plus Hypoxia Workstation (0.3 % O2, 0.1 % CO2, 99.6 % N2; Baker Ruskinn) before being sealed with picodent twinsil speed 22 (picodent Dental-Produktions- und Vertriebs GmbH) or nail polish.

5.2 Acquisition of Kinesin Position Traces

In order to record phase scanning MINFLUX traces of walking kinesin, $5\times5\,\mu m^2$ confocal xy-scans with a pixel size of 50 nm were performed with the 488 nm laser, to excite the Alexa Fluor 488 labeled microtubules. On single microtubules, one to three pixels were manually selected and sequentially multiplexed with 10 ms exposures of the 640 nm laser to identify ATTO 647N labeled kinesin walking into the detection volume. By addressing multiple positions almost simultaneously, the active area for detecting events was significantly increased, which in turn improved the number of traces recorded per time. For automatically triggering the MINFLUX tracking routine, described in section 3.3, the photon threshold was set to around 5 kHz, depending on the walking speed expected for the respective sample. For all MINFLUX measurements of kinesin, the last and smallest L was set to 30 nm and the temporal resolution was below 2 ms. The tracking duration varied between around 1 s for measurements at $\geq$100 µM ATP concentrations and up to 3 s at 10 µM ATP concentrations and at 1 mM ATPγS, a slowly hydrolizing ATP analogue.
To further increase the active area for detecting slowly walking kinesin consuming ATPγS, the triggering routine was adapted. Instead of multiplexing only a few positions on individual microtubules, a $10\times10\,\mu m^2$ FOV was recorded with the 488 nm laser. All visible microtubules were manually segmented and the same FOV was repeatedly scanned with the 640 nm laser. Emission spots in the kinesin channel that colocalized with the segmented microtubules were addressed by the galvo-scanner and a MINFLUX tracking measurement was performed.

5.3 Analysis of kinesin traces

Online- and post-processing of MINFLUX position traces was performed similar to the single molecule data analysis described in section 4.2. As kinesin was walking for a significant distance within the detection volume, the detection probability could not be assumed constant and therefore the fixed-curvature estimator could not be used. Instead the position was estimated employing a sliding-curvature estimator (SCE) described in the following section. Traces were selected manually based on their SBR and a visi-

ble stepwise movement. Further, the exported traces were aligned by a simple rotation matrix to extract the positions along the microtubule axis (on-axis position) and perpendicular to the on-axis (off-axis position). The on-axis position was then subjected to the step-finding algorithm described in section 4.2.3 with a step size threshold of 5 nm. The detected change-points were subsequently applied to the off-axis position to extract also the off-axis step-function. Based on the step-function, the step sizes and the times between steps were extracted as well as the average photon count and position standard deviation within each plateau. Those values were then automatically saved in excel sheets for further processing.
Data from individual kinesin constructs and ATP concentrations were pooled for evaluation. First, the excel sheets for single traces were loaded and the step sizes were aligned such that the kinesin motion pointed in positive x direction. Traces with less than three steps or an average plateau standard deviation larger 6 nm were excluded from further analysis.

5.3.1 Sliding-Curvature Estimator

Kinesin is walking unidirectionally along microtubules, which, in contrast to the performed single molecule tracking experiments (see section 4.4), results in a changing photon detection efficiency, depending on the protein position relative to the stationary detection volume. As a consequence the apparent curvature b changed over time and the FCE was not applicable. At the same time, the GLSE does not achieve optimal precision at low photon counts, as the individually obtained curvature produces large outliers. However on short timescales, on the order of several tens of milliseconds, the position of kinesin did not change significantly, allowing for a more robust determination of the current curvature. This concept was implemented in the so-called sliding-curvature estimator (SCE)

$$x_{\mathrm{SCE,i}} = \frac{n_{-,i} - n_{+,i}}{2L \sum_{k=i-w}^{i+w} b_k/(2w+1)}, \tag{5.1}$$

which calculated the mean curvature $\langle b \rangle = \sum_{k=i-w}^{i+w} b_k/(2w+1)$ (b_k was calculated according to equation 3.3) from a sliding window around the current localization i and then retrieved a position estimate similar to equation 4.2. This approach improved the localization precision, especially at low fluorescence photon numbers and low SBR. At the same time, it could respond to changes in the apparent curvature, inherent to long range tracking. The improvement depended on the total number of photons used to define the curvature and thus also on the width $2w+1$ of the sliding window. Based on numerical simulations, the deviation of the SCE precision from the theoretical optimum was continuously decreasing and dropped below 5 % at around 300 photons for a SBR of one.

When employing the SCE for kinesin tracking data, first all localizations with less than seven detected photons were rejected to exclude background. Next, for establishing the current curvature of each localization, the width of the sliding window was adapted based on the mean photon count, realizing on average 300 photons. At an average photon count of 20 photons per localization, this concluded a width of 15 localizations, yielding a temporal smoothing of the curvature over around 10 ms. Finally any localizations with negative curvature or an emitter position farther than L from the excitation intensity minimum were discarded. For more details on the SCE please refer to section A.3.

5.3.2 Hidden Markov Model

During walking, the labeled kinesin head alternates between a microtubule bound (B) and microtubule unbound (U) state. These vary in duration and were not directly accessible from the position traces. Still, as complete steps to the next free binding site on the microtubule are known to be around 16 nm and steps to the intermediate U state therefore measure around 8 nm, it was possible to extract the most likely sequence of states from the succession of step sizes with a five state Hidden Markov Model (HMM). The two main transitions in this model include progressions from a B to an U state and from an U back to a B state. However, due to the finite temporal resolution and spatial precision, not all of these transition could be observed, leading to apparent direct transitions from B to B or U to U states. Finally, the fifth transition accounts for previously observed so-called slip states [42]. If through these the heads are exchanged, an unpaired 8 nm step will occur, as the labeled head switches between B and U state without any on-axis displacement. To incorporate this detail in the HMM, rare 8 nm B to B transitions were allowed. For constructing the HMM, the step sizes were assumed to be normally distributed around 8 nm and 16 nm, with a full width at half maximum (FWHM) of 4.71 nm. Further, the probability matrix for consecutive transitions allowed the labeled head to switch states only when taking steps. An overview of the state transitions and their succession is given in table 5.2.

Table 5.2: **Transitions included in the Hidden Markov Model** containing the initial and final state (bound B, unbound U), the average assumed step size, the biological reasoning and the possible following transitions.

Number	Transition	Step size	Source	Next transition
1	B to U	8 nm	Substep	2 (99 %), 4 (1 %)
2	U to B	8 nm	Substep	1 (49.5 %), 3 (49.5 %), 5 (1 %)
3	B to B	16 nm	Missed U state	1 (49.5 %), 3 (49.5 %), 5 (1 %)
4	U to U	16 nm	Missed B state	2 (99 %), 4 (1 %)
5	B to B	8 nm	Slip state	1 (49.5 %), 3 (49.5 %), 5 (1 %)

5.3.3 Model for the Dwell Time Distribution of the Bound and Unbound State

The HMM allowed to retrieve the dwell times spent in the B and U state by the labeled head. As only one head is labeled, half of the protein motion is unobservable. To assess the underlying kinetics of kinesin being bound to the microtubule with either one or two heads (one-head-bound (1HB), two-head-bound (2HB)), the distribution of dwell times in the B and U state were fitted simultaneously, assuming equal kinetics for both heads. In the U state, the labeled head is detached from the microtubule and thus the U state and the 1HB state of kinesin are identical. Consequently, the distribution of dwell times should follow a single exponential with the characteristic time $\tau_{1\mathrm{HB}}$

$$p_U(t) = p_{1\mathrm{HB}}(t) = \frac{e^{-t/\tau_{1\mathrm{HB}}}}{\tau_{1\mathrm{HB}}}. \tag{5.2}$$

The B state, however, comprises the sequence of the 2HB state with the labeled head leading, the 1HB state with the unlabeled head detached and the 2HB state with the labeled head trailing. Each of these states is exponentially distributed with the characteristic times being $\tau_{1\mathrm{HB}}$ for the 1HB state and $\tau_{2\mathrm{HB}}$ for the 2HB state. The dwell times in the B state are thus described by a convolution of three exponential processes

$$\begin{aligned} p_B(t) &= \int_0^t p_{2\mathrm{HB}}(t-\tau) \int_0^\tau p_{1\mathrm{HB}}(\tau - t') p_{2\mathrm{HB}}(t') dt' d\tau \\ &= \frac{1}{\tau_{2\mathrm{HB}} \left(\tau_{2\mathrm{HB}} - \tau_{1\mathrm{HB}}\right)} \left(t e^{-t/\tau_{2\mathrm{HB}}} - \frac{\tau_{1\mathrm{HB}}\tau_{2\mathrm{HB}}}{\tau_{2\mathrm{HB}} - \tau_{1\mathrm{HB}}} \left(e^{-t/\tau_{2\mathrm{HB}}} - e^{-t/\tau_{1\mathrm{HB}}} \right) \right). \end{aligned} \tag{5.3}$$

Note that steps before or after backsteps likely exhibit kinetics different than those part of the continuous forward stepping, and were thus, together with the backsteps, excluded from the temporal analysis. As stated in section 4.2.3, due to the finite spatial precision and temporal resolution of the recorded data, there was a lower limit to the reliable detection of the B and U state. Numerical simulations invoking the substep size of 8 nm and a plateau standard deviation of 4 nm, as commonly achieved in this kinesin tracking study, yielded a reduced detection probability for states shorter than 8 ms. To exclude this evaluation bias, only plateaus longer than 8 ms were included into the fit of the 1HB and 2HB dwell times.

5.4 Precise Protein Tracking with MINFLUX

At first, MINFLUX tracking experiments of the coiled-coil-labeled kinesin construct N356C were conducted. Note that by tracking the position of the coiled-coil domain, the pro-

tein center-of-mass was followed and thus regular steps and substeps measured as 8 nm and 4 nm on-axis displacements, respectively. As kinesin is known to walk at several hundred nanometers per second, one 8 nm step each 10 - 30 ms was expected. Substeps were assumed to appear on an even shorter timescale. The MINFLUX tracking data of immobilized ATTO 647N molecules has confirmed a sufficient STP to resolve these steps. However, as the kinesin samples exhibited higher background signal, the number of required photons was increased to meet this performance. In order to increase the number of detected photons while maintaining a high measurement speed, the MINFLUX tracking routine was reduced to only one dimension, aligned with the microtubule axis and thus exclusively recording the on-axis positions. Simultaneously the recording time of a single localization was doubled, rendering again millisecond temporal resolution. As the phase scanner cannot selectively measure along arbitrary dimension, microtubules aligned with the x-axis of our microscope were selected to perform measurements solely along this dimension.

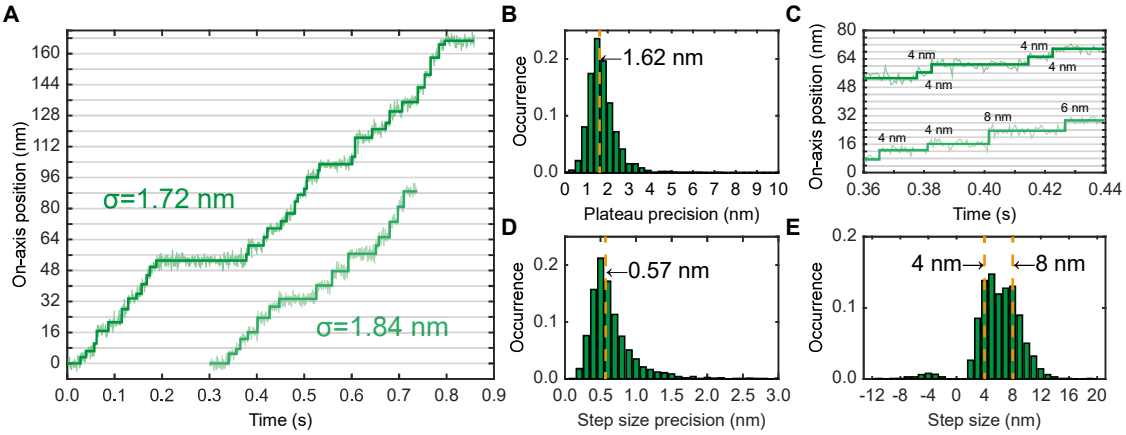

Figure 5.2: **Kinesin substeps visualized by tracking the coiled-coil domain** at 10 µM ATP concentration. **(A)** Two MINFLUX position traces of the construct N356C labeled with ATTO 647N (semi-transparent lines) overlaid with the calculated step-function (solid lines). A localization precision of around 1.8 nm was achieved in both traces. **(B)** Histogram of the localization precision of all 1975 plateaus detected within 155 traces. The median localization precision is given by 1.62 nm. **(C)** Zoom-in of the traces shown in (A) highlighting clear 4 nm substeps, a regular 8 nm step and one unexpected 6 nm step. **(D)** Calculated precision of all detected step sizes based on the standard error of the mean for each plateau. The median precision is given by 0.57 nm. **(E)** Histogram of all 1821 detected step sizes (including 55 backsteps), showing steps in the range of 3-11 nm with large fractions of 4 nm substeps and 8 nm regular steps (dashed orange lines).

Figure 5.2 **(A)** shows two exemplary traces that were recorded at 10 µM ATP concentration, with a walking speed of around 200 nm s^{-1} and a clear stepwise movement. The raw data points (semi-transparent lines) are overlaid with the step-function generated

according to section 4.2.3. Both traces exhibit an average localization precision of around 1.8 nm, which required the detection of 40 - 100 photons per localization. As the galvo scanner position was kept constant within single MINFLUX measurements, the large distance traveled by kinesin caused the photon count to decline at the periphery of the detection volume. Since the localization precision scales with the number of photons, the precision also varies within single traces. Evaluation of all 154 traces recorded at 10 µM ATP concentration and calculating the localization precision for each of the 1975 detected plateaus, yielded a median precision of 1.62 nm (see figure 5.2 **(B)**) requiring a median number of 101 detected photons.
Taking a closer look at the traces shown in figure 5.2 **(A)** disclosed clear steps of 4 nm and 8 nm corresponding to substeps and regular steps, respectively (see figure 5.2 **(C)**). Further, the precision of detected step size was calculated based on the standard error of the mean for the plateaus before and after each step and was found to be $\leq$1 nm for above 90 % of all steps, with its median reading 0.57 nm (see figure 5.2 **(D)**). Plotting all 1821 step sizes in a histogram substantiated the almost equal occurrence of regular steps and substeps (see figure 5.2 **(E)**). Overall, the majority of step sizes was between 3 nm and 11 nm, while only a very small number of steps (55) having a negative step size.
Strikingly, a significant number of 6 nm steps was also observed, that do not match the 8 nm periodicity of microtubules. On the one hand, the occurrence of these step sizes could have been caused by additional off-axis displacement or errors in the microtubule lattice. On the other hand, the non-negligible (with respect to the localization precision) label and linker size might reflect in the data as artifact. A pure evaluation error shall be excluded at this point, as the precision of detected step sizes was much smaller than the actual distribution of step sizes. A possible explanation for the occurrence of these 6 nm steps will be given over the course of the following section.
It shall be further emphasized, that this work is the first to directly observe substeps of kinesin by only labeling with a single fluorescent molecule. Accessing these timescales with single digit nanometer precision has so far been exclusive to studies exploiting the high scattering signal of beads, either via optical traps or by light scattering. By improving the STP by around one order of magnitude compared to camera-based single fluorophore tracking [18], MINFLUX is enabling the minimally invasive and load-free investigation of protein dynamics.

5.4.1 Visualization of a Coiled-Coil Rotation

Having proven that MINFLUX tracking can unambiguously resolve substeps at low ATP concentrations, further experiments were conducted at physiological concentrations of 1 mM ATP. At this concentration, the kinetics of kinesin are typically saturated [41],

meaning that increasing ATP does not yield higher speed. Despite the average walking speed of around 550 nm s^{-1} for the recorded MINFLUX data, steps and substeps could still be resolved. However, the fraction of detected substeps decreased compared to the data measured at 10 µM ATP. As the localization precision and temporal resolution were comparable between the two data sets, this observation hints towards a change of the substep kinetics, making them faster and hence less likely to detect. The histogram of step sizes, as displayed in figure 5.3 **(A)**, further shows surprisingly large amounts of 6 nm and 10 nm steps. To fathom the origins of these, the step sizes were plotted against the size of the previous step in a 2D-histogram, uncovering a clear correlation. Seemingly the coiled-coil domain progressed by an alternating sequence of 6 nm and 10 nm steps, totaling up to the 16 nm distance expected for a complete mechanochemical cycle of kinesin taking one step with each head.

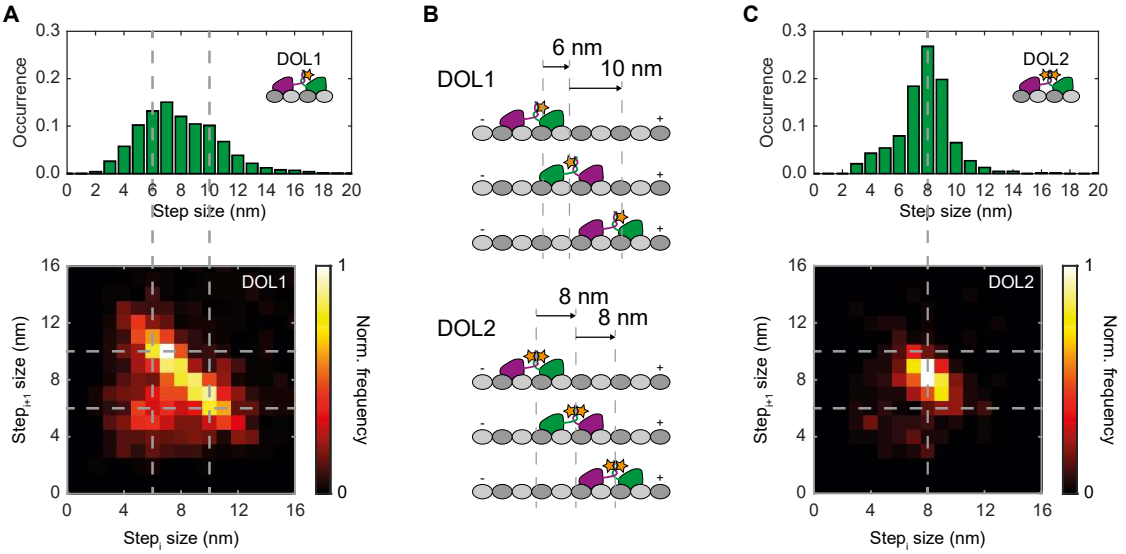

Figure 5.3: **Rotation of the coiled-coil domain** upon kinesin stepping. **(A)** Top: Population normalized histogram of the evaluated step sizes at 1 mM ATP concentration for a single fluorescent label (DOL1, inlay), showing large fractions of 6 nm and 10 nm steps. Bottom: Normalized 2D-histogram of step sizes for successive steps showing alternating 6 nm and 10 nm steps (see dashed grey lines). A total of 1810 steps of 136 traces were evaluated. **(B)** Sketch of the proposed model for the rotation of the coiled-coil domain of kinesin and the implications on the measured step sizes for tracking a single-labeled (top) or double-labeled (bottom) protein. **(C)** Top: Population normalized histogram of the detected step sizes at 1 mM ATP concentration for a kinesin carrying two fluorescent labels (DOL2, inlay), showing one dominant fraction of 8 nm steps. Bottom: Normalized 2D-histogram of successive step sizes supporting the observation of mainly consecutive 8 nm steps (see dashed grey lines). A total of 630 steps of 130 traces were evaluated.

One possible explanation for this asymmetry is given by a rotation of the coiled-coil domain upon stepping in combination with a non-negligibly sized label and linker. Assuming

that the small, yet non-zero displacement of the fluorophore core from the coiled-coil axis had a significant component along the walking direction, the apparent step size should be increased/reduced by twice of that displacement (see figure 5.3 **(B)**, DOL1) upon a full step and a 180-degree coiled-coil rotation. The observed deviation of ±2 nm from the expected size of a regular step allows to conclude a fluorophore displacement of 1 nm, which lies within the plausible range given a coiled-coil radius of ∼ 1 nm and a linker length of ∼ 1 nm. To test this hypothesis, both copies of the kinesin monomer were labeled at the same position on the coiled-coil domain. Consequently, symmetry was restored as the center-of-mass of the fluorophores, which MINFLUX always tracks by default, coincides with the core of the coiled-coil domain (see figure 5.3 **(B)**, DOL2). To verify that the tracked kinesins were carrying two emitting labels, only steps between such plateaus were evaluated that had been measured with a photon rate exceeding a given photon threshold of 167 kHz. This threshold was set based on the histogram of detected photons of all plateaus recorded under the same conditions (see figure A.3), excluding those steps where one fluorophore already photobleached.

Figure 5.3 **(C)** shows the histogram of the evaluated individual step sizes and the 2D-histogram of step sizes of successive steps for kinesin carrying two fluorophores at the coiled-coil domain (DOL2). Supporting the hypothesis of a coiled-coil rotation, a sequence of successive 8 nm steps was dominant.

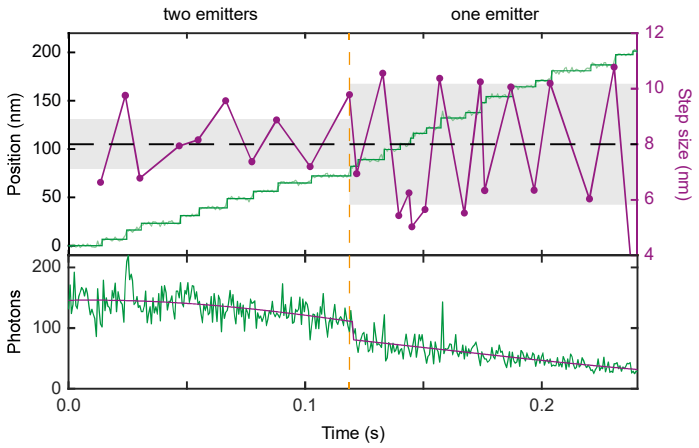

Figure 5.4: **MINFLUX trace of construct N356C (DOL2)** with one emitter bleaching at around 0.12 s. Top: Raw on-axis position data (semi-transparent green line), overlaid with the detected step function (solid green line, left axis). The evaluated step sizes are displayed in purple (right axis). The approximate spread of step sizes before and after the bleaching event is illustrated by grey boxes. Bottom: Corresponding photon signal (green line) of the trace above, overlaid with a Gaussian fit including a single bleaching step (purple line). The Gaussian-shaped decline in the photon signal is due to kinesin walking out of the confocal detection volume. The bleaching step at around 0.12 s is highlighted by the dashed orange line.

Further corroborating this finding, figure 5.4 displays a trace, during the recording of which one of the fluorophores bleached at around 0.12 s, as evident from the abrupt decline in the photon signal. Note that the overall decline in photon signal was due to kinesin walking towards the periphery of the detection volume, which decreased the photon detection probability. When taking a look at the on-axis position of this trace before the bleaching event, the recorded step sizes spread randomly around 8 nm, as expected for the coiled-coil domain carrying two emitters. After photobleaching, the step sizes started to systematically alternate (with one 10 nm step shortly before 0.15 s being detected as two substeps) between 10 nm and 6 nm, consistent with the observed behavior for the coiled-coil domain carrying only one emitter.
At this point, the observation of a significant number of 6 nm steps of single-labeled construct N356C at 10 µM ATP can possibly also be attributed to the alternating regular step sizes due to the coiled-coil rotation. Consulting these values, the expected apparent sizes for substeps are actually 3 nm and 5 nm. Additionally, 8 nm steps can occur due to a missed bound state. Overall 3 nm, 5 nm, 6 nm, 8 nm and 10 nm steps are possible with different occurrence and detection probabilities. The attained STP might not suffice to resolve this close distribution, which in practice was very likely also broadened by biological mobility of both the microtubule subunit spacing and fluorophore displacement from the coiled-coil domain.
Concluding, the analysis of over 4000 recorded steps of kinesin labeled at the coiled-coil domain uncovered a significant rotation of the latter upon stepping. Whether this is part of a continuous rotation during a symmetric hand-over-hand motion or a back-and-forth rotation during an asymmetric hand-over-hand motion cannot be derived from these results.

5.5 Resolving the Mechanochemical Cycle of Kinesin

As noted in the last section, the occurrence of kinesin substeps, observed by labeling of the coiled-coil domain, was ATP-dependent. To quantify the ATP-dependent kinetics of substeps, the kinesin construct T324C was labeled at one of its heads. The label position on the head was located at the center-right side with respect to the kinesin walking direction. Now tracking an individual head the steps and substeps measured as 16 nm and 8 nm, respectively. Traces of this construct were recorded at 10 µM, 100 µM and 1 mM ATP concentrations and the bound and unbound states were identified by the HMM described in section 5.3.2. In contrast to construct N356C, 2D-traces were recorded rendering the position along the microtubule (on-axis) and perpendicular to it (off-axis). Figure 5.5 **(A)** shows an exemplary trace recorded at 10 µM ATP concentration, resolving

individual 16 nm steps as well as 8 nm substeps. Note that the decreasing localization precision at the end of the trace is due to kinesin walking out of the detection volume, as described in the previous section.

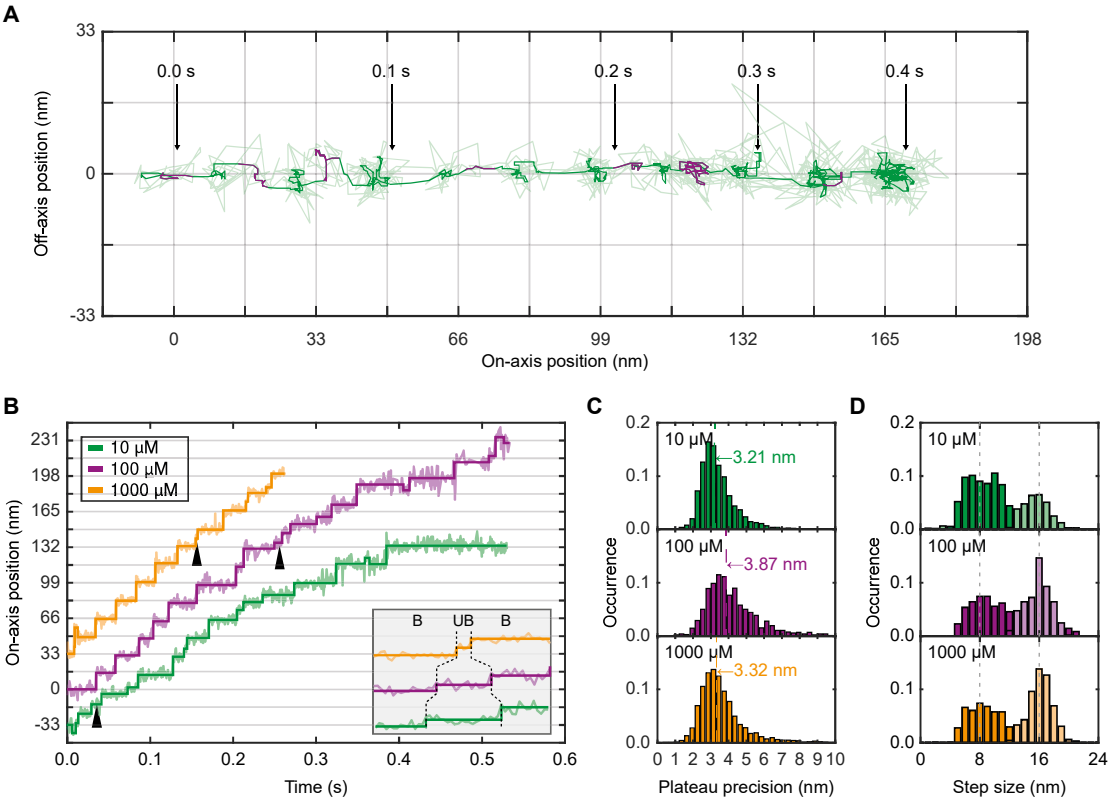

Figure 5.5: **Substeps of individual kinesin heads**, labeled with ATTO 647N, visualized at 10 µM, 100 µM and 1 mM ATP concentrations. **(A)** 2D-plot of the on-axis and off-axis position recorded at 10 µM ATP. The raw data (semi-transparent green line) are overlaid with a 5 ms moving median filter (solid green line) for visibility. For unbound states, detected by the HMM, the median filtered position is displayed in purple. Time points at each 0.1 s are shown by black arrows. **(B)** On-axis position traces (semi-transparent lines) overlaid with the detected step-function (solid lines) for different ATP concentrations. The inlay shows the unbound states highlighted by the black arrows aligned in time. **(C)** Population normalized histogram of the measured plateau precision at each ATP concentration together with the corresponding median. **(D)** Population normalized histogram of the evaluated step sizes at each ATP concentration. Steps that were identified as substeps by the HMM are displayed with solid filling. Step sizes of regular steps are displayed with semi-transparent filling.

The on-axis stepping motion of kinesin at different ATP concentrations is shown in figure 5.5 **(B)**. At each concentration, steps and substeps could be resolved and identified by the HMM. Despite the large variety of walking speeds between 250 nm s^{-1} (10 µM ATP) to 550 nm s^{-1} (1 mM ATP), which was in good agreement with the walking speeds observed for N356C, the tracking precision was consistently between 3-4 nm per 0.63 ms localiza-

tion (see figure 5.5 **(C)**). This precision was achieved by only detecting 10 - 30 photons per 1D-localization and could not be further improved, as increasing the laser power resulted in significantly faster photobleaching. At around half the excitation power of construct N356C, the achieved photon rate was only slightly reduced. However, the detected photons were now needed to localize in x- and y-direction. In total, the fluorescence photons available for localizing along a single dimension were reduced by more than a factor of three, explaining the two-fold decrease in localization precision. Yet, the precision was sufficient to detect substeps with similar probability, as the ratio of precision to step size remained constant. The step size histogram in figure 5.5 **(D)** shows a substantial decrease of the occurrence of substeps with increasing ATP concentration. In line with the results of construct N356C, this observation implies a change in the kinetics of the unbound state. The unexpectedly broad distribution of substeps will be discussed in a later section. Overall, 2474 regular steps and 3357 substeps were detected with a median step size precision of 1 nm within a total of 758 traces.

5.5.1 Kinesin Binds ATP in the One-Head-Bound State

Employing the assignment of bound and unbound states of the labeled head by the HMM, the time spent in each state was plotted in separate histograms for each ATP concentration separately. As apparent from figure 5.6 **(A)**, these times reduced with increasing ATP concentrations due to faster availability of ATP, concluding in the higher walking speed. In order to extract whether kinesin binds ATP in the 1HB or 2HB state, these histograms were fitted by the dwell time model described in section 5.3.3. As the model includes two characteristic times relevant for both distributions, the histograms of the bound and unbound state were fitted simultaneously, yielding one pair of dwell times (τ_{1HB}, τ_{2HB}). Figure 5.6 **(B)** depicts the extracted dwell times for each ATP concentration, showing a strong increase of τ_{1HB} from around 8 ms to above 30 ms with decreasing ATP concentrations, while τ_{2HB} stays nearly constant at around 8.2 ms. observation implies that access to ATP is the rate determining factor for the 1HB state and thereby controls the kinesin walking speed. The fact that τ_{2HB} does not exhibit any ATP dependence entails that ATP binds to kinesin exclusively in the 1HB state.

To further derive whether ATP binding is sufficient for kinesin to complete the full step to its next binding site on the microtubule, or whether ATP hydrolization is additionally required, MINFLUX tracking experiments were repeated at 1 mM of the slowly hydrolizing ATP analogue ATPγS. Under these conditions, the walking speed was reduced to below 50 nm s^{-1}, resulting in only two to three steps per second. Strikingly, besides the extremely slow walking of kinesin, the time spent in the unbound state was similar to that measured at 1 mM regular ATP and only the time spent in the bound state substantially

increased. This prompts the conclusion that binding ATP is sufficient for the unbound head to be forced to its next binding position, before ATP is actually hydrolized.

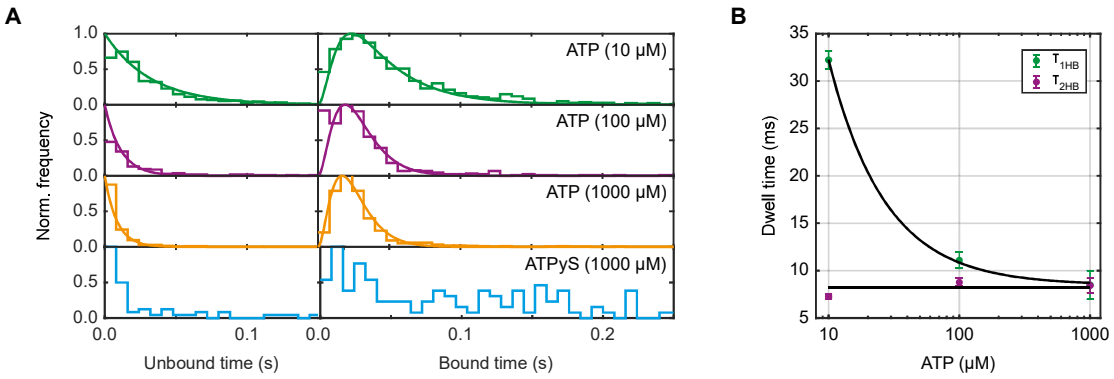

Figure 5.6: **ATP-dependent dwell times of the bound and unbound state** of the labeled head imply that ATP binds in the 1HB state. **(A)** Normalized histograms of the times spent in the bound and unbound state (stair function) overlaid with the fitted model (eq. 5.2 and eq. 5.3) for 10 µM, 100 µM and 1 mM ATP concentrations. The bottom histogram shows the dwell times recorded for ATPγS, a slowly hydrolizing ATP analogue. Due to the long time spent in the bound state and correspondingly low statistics the model failed to fit the data. **(B)** Dwell times of the 1HB and 2HB state as calculated from the fit. The ATP-dependent 1HB dwell times were fitted with a Michaelis-Menten kinetics ($\tau_{\mathrm{sat}}\,(1 + K_{\mathrm{M}}/\,[\mathrm{ATP}])$), yielding $K_{\mathrm{M}} = 28 \pm 2\,\mu\mathrm{M}$ and $K_{\mathrm{ATP}} = \tau_{\mathrm{sat}}^{-1} K_{\mathrm{M}}^{-1} = 4.2 \pm 0.4\,\mathrm{s}^{-1}\,\mu\mathrm{M}^{-1}$ and the ATP-independent 2HB dwell times were fitted with a constant function $\tau_{\mathrm{2HB}} = 8.2\,\mathrm{ms}$. The error bars denote the 64 % confidence interval of the fit.

5.5.2 Slip States Cause Unpaired Substeps

A closer inspection of the traces revealed the rare occurrence of unpaired substeps (see figure 5.7 **(A)**). The labeled head seems to have entered the unbound state via a substep, but have switched back into a bound state without any further on-axis or off-axis displacement. This behavior can be explained by so-called slip states. These have been recently reported under force, though the principle remains the same for the force-free case [42]. They describe a state in which kinesin is not bound, but weakly associated with the microtubule surface. From a slip state, kinesin can fully detach, but in most cases it will rescue itself by reattaching with one of its head to the microtubule. This procedure is depicted in figure 5.7 **(B)**. If kinesin reattaches with the same head to the same microtubule binding site, the temporary slip state won't be mapped in the recorded trace. However, if the heads upon reattachement are exchanged the labeled switches either from a bound to an unbound state, or vice versa, generating the observed unpaired substeps. In total, the number of slip states detected by the HMM accounted for around 2 % of all steps.

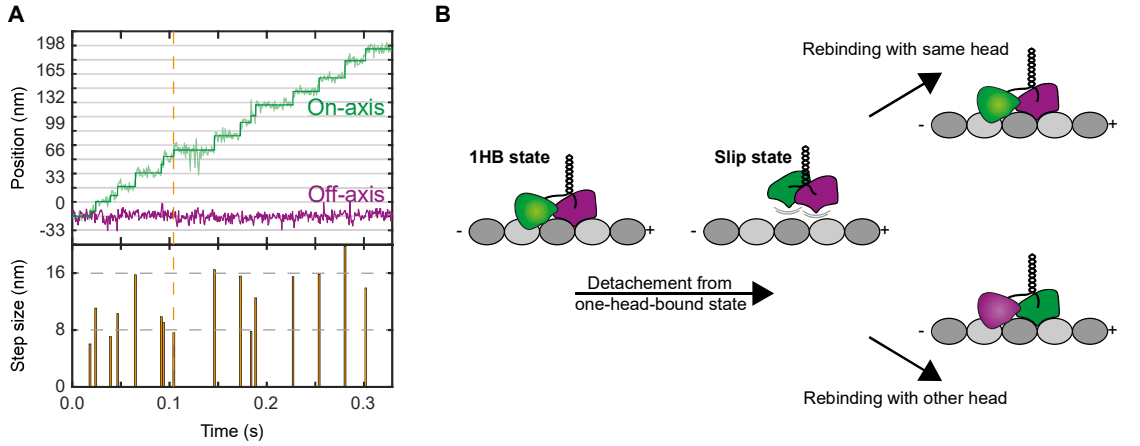

Figure 5.7: **Force-free slip states of kinesin** inferred from the observation of unpaired substeps. **(A)** Top: Exemplary on-axis and off-axis position trace of construct T324C labeled with ATTO 647N recorded at 1 mM ATP concentration. Bottom: Evaluated step sizes of around 16 nm and 8 nm. An unpaired substep at around 0.1 s is highlighted by the dashed orange line. **(B)** Sketch of kinesin entering a so-called slip state, during which it is only weakly associated with the microtubule surface, and recovering by either rebinding with the same head, leaving the walking pattern unaffected, or with the previously unbound head leading to the occurrence of unpaired substeps.

5.6 Dissecting the Unbound State of Kinesin

After having precisely tracked the center of the kinesin head (construct T324), in the next step, further constructs were investigated, carrying ATTO 674N either at the front (construct E215C) or the back (construct K28C) of the kinesin head with respect to the walking direction. The on-axis and off-axis positions were recorded at 0.63 ms temporal resolution, employing 10 µM, 100 µM and 1 mM ATP concentrations. Figure 5.8 **(A)** shows an exemplary trace for each of the two constructs recorded at 10 µM ATP concentration. Strikingly, the position traces of construct E215C displayed almost no substeps compared to the ones of construct K28C showing lots of clearly visible substeps. The absence of substeps for construct E215C cannot be explained by a reduced detection efficiency for substeps, as the precision of individual plateaus was comparable to that of construct T324C and only slightly lower than that of construct K28C (see figure 5.8 **(B)**). Consistently, all three head-labeled constructs yielded a median precision of around 3 nm, whilst only requiring around 20 fluorescence photons per localization and dimension. Taking a look at the step size histograms of both constructs E215C and K28C (see figure 5.8 **(C)**) underlines the strong reduction of substeps of construct E215C for all ATP concentrations. In addition, while construct K28C followed the same ATP-dependence of substeps that was observed with construct T324C, construct E215C merely exhibited an

increase in detected substeps for decreasing ATP concentrations. Moreover, when looking at the time spent in the unbound state, constructs T324C and K28C resembled each other, while the time in the unbound state of construct E215C was constantly short for all ATP concentrations (see figure A.4). This leads to the assumption that the few detected substeps of construct E215C might not represent the actual unbound state of the head, but rather originate from either overfitting due to position noise at the time of a step or the biological variability in the stepping behavior of kinesin.

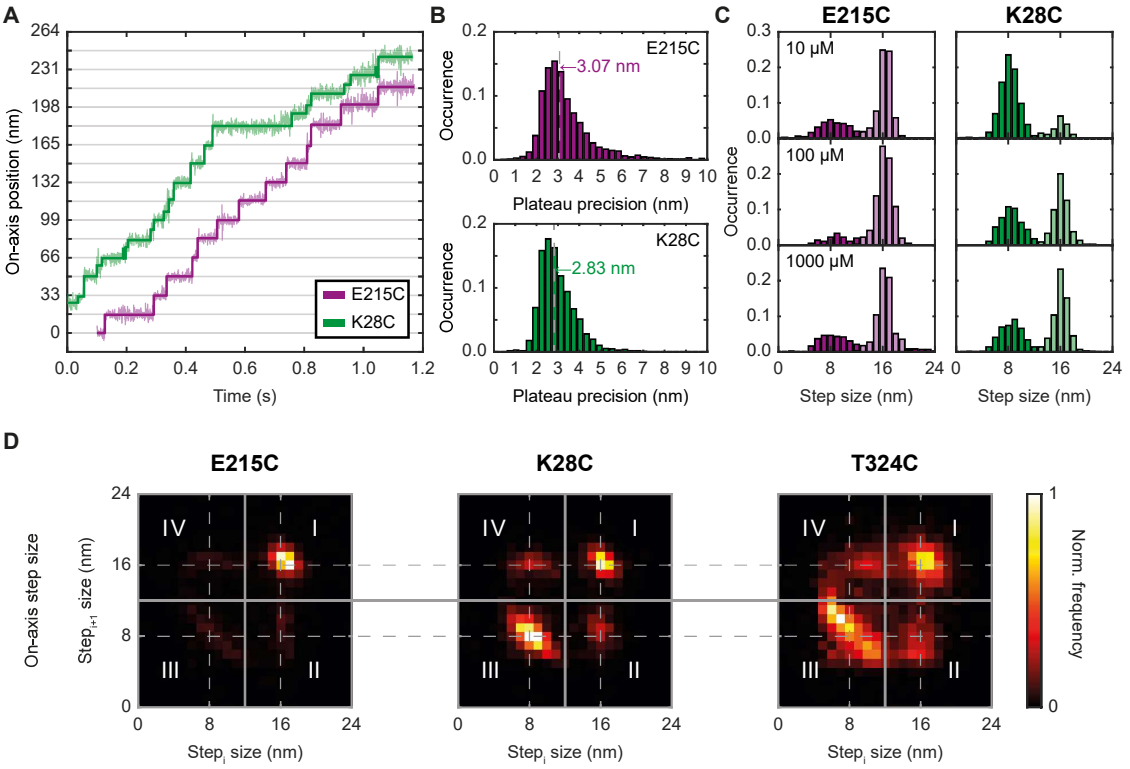

Figure 5.8: **Substeps recorded at different positions on the head** show a rotation of the head when entering the unbound state. **(A)** On-axis position traces of the constructs K28C and E215C recorded at 10 µM ATP concentration. **(B)** Population normalized histograms of the plateau precision of both constructs. The median precisions are given by the dashed lines. **(C)** Population normalized histograms of the step sizes of both constructs at 10 µM, 100 µM and 1 mM ATP concentrations. **(D)** Normalized 2D-histograms of the sequence of step sizes for all head-labeled constructs highlighting consecutive 16 nm steps (I), regular steps followed by substeps (II), successive substeps (III) and substeps followed by regular steps (IV).

To further comprehend the on-axis movement observed for the different parts of the head, the sequence of step sizes for all ATP concentrations combined was analyzed in individual 2D-histogram for each construct (see figure 5.8 **(D)**). The histograms can be divided into four segments, each representing a specific aspect of kinesin walking. Segment I contains consecutive 16 nm steps between binding sites on the microtubule, segment II

contains substep into an unbound state, segment III contains a series of substeps and segment IV contains transitions from the unbound state back to the bound state. Non surprisingly, construct E215 overwhelmingly showed successive 16 nm steps (segment I), as nearly no substeps have been observed. Construct K28C, in contrast, displayed clear 8 nm substeps, which also occurred sequentially, especially for low ATP concentrations. Further, for construct T324C, the in-depth analysis of step sizes revealed an asymmetry in substep sizes between transitions from a bound to an unbound state (segment II) and vice versa (segment IV). The former rendered around 6-7 nm substeps, whereas the latter resulted in 9-10 nm substeps. To conclude, the high STP of MINFLUX allowed to specifically label different regions of the kinesin head with only a single fluorophore and thereby enabled the visualization of different substepping characteristics of each part of the head (front, middle, back). Invoking these distances, an intrusive explanation for this observation is a rotation of the head around its front (represented by amino acid position 215), when entering the unbound state. To further pursue this hypothesis and derive a 3D-orientation of the unbound head, the off-axis displacements were investigated.

5.6.1 Off-Axis Displacement during the Unbound State

Close-up inspection of individual traces revealed a systematic off-axis displacement during the unbound state for construct K28C. Figure 5.9 **(A)** shows an exemplary trace during the recording of which the label was positively displaced by around 5 nm with respect to the laboratory system each time the head was in the unbound state. When transitioning back to the bound state, the head returned to its previous off-axis position assumed to align with the microtubule protofilament on which the exemplary kinesin walked along. Upon 16 nm steps, no off-axis displacement of the label was observed. In contrast, construct T324C did neither display off-axis displacement during substepping nor upon regular steps. This observation supports the hypothesis that the unbound head rotates when entering its unbound state, displacing mainly the back of the kinesin head away from the protofilament. To analyze the off-axis displacement of the fluorescent label during the unbound state at both the middle and back of the head, the sequence of off-axis substep sizes was examined from 2D-histograms.
Instead of just plotting successive off-axis substep sizes, which have to cancel out to preserve staying on the same protofilament, substeps were compared to their second to next substep. This way, bound to unbound and unbound to bound transitions were treated separately. As the latter were just inverse in sign to the former, unbound to bound transitions were inverted to match the direction of the off-axis displacement for bound to unbound transitions. Figure 5.9 **(B)** displays the succession of off-axis displacements as just described for all individual steps. For construct T324C, the histogram shows no

correlation within traces. However for construct K28C, the displacement appeared to be consistent in magnitude and direction for single traces and ranged up to 5 nm. Interestingly, oppositely directed displacement was observed between different traces. The strong correlation of sequential off-axis substep sizes is emphasized by a Pearson correlation coefficient of $\rho = 0.65 \pm 0.02$, which is rather high, taking into account that the magnitude of displacement is on the same order of magnitude as the noise. Furthermore, when decreasing the noise by averaging over single traces, a very small, yet prominent off-axis displacement of below 2 nm was revealed for the unbound state of construct T324C (Pearson correlation coefficient $\rho = 0.77 \pm 0.03$). Applying the same averaging to the data of construct K28C did not yield substantial changes in the conclusion, yet underlines the strong correlation ($\rho = 0.93 \pm 0.01$).

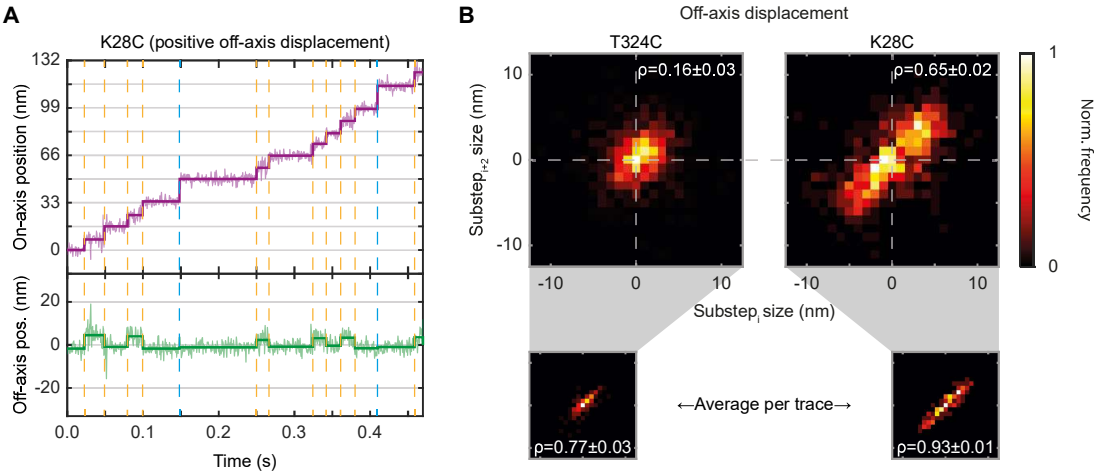

Figure 5.9: **Off-axis displacement during the unbound state** of constructs K28C and T324C. **(A)** On-axis (purple) and off-axis (green) position traces of construct K28C recorded at 10 µM ATP concentration showing strong positive displacement during the unbound state. Transitions between bound and unbound states are highlighted by orange dashed lines. Transitions of 16 nm between bound states are highlighted by dashed blue lines. **(B)** Top: Normalized 2D-histograms of the off-axis displacement for all consecutive bound to unbound and consecutive unbound to bound transitions together with the corresponding Pearson correlation coefficient ρ. Bottom: Same as in (Top), but bound to unbound and unbound to bound transitions were averaged for individual traces.

Considering the tubular structure of microtubules and the fact that the presented MINFLUX tracking measurements visualize the projection of the actual 3D-trajectory of each label onto the imaging plane, two possible explanations for the off-axis displacement arise. Figure 5.10 **(A)** depicts how an upward movement of the head away from the microtubule surface upon entering the unbound state would translate into the into different off-axis displacements depending on the microtubule position of the protofilament the observed kinesin walked along (see definition in figure 6.10 (A) and (B)). For kinesin walking along

the sides of a microtubule, an upward head movement would cause positive and negative off-axis displacement and, for kinesin walking along the top or the bottom of a microtubule, no off-axis displacement would be observed. In contrast, figure 5.10 **(B)** illustrates the projected off-axis displacement for the kinesin head being shifted rightwards along the surface of the microtubule upon entering its unbound state. Contrary to the upwards displaced head, only kinesin walking along center protofilaments will generate traces with clear off-axis displacement. However, for kinesins walking along top and bottom protofilaments this can be both positive and negative. For kinesins walking along protofilaments on the side of a microtubule, no off-axis displacement would be observed.
Unfortunately, both scenarios comprise positive, zero and negative off-axis displacement with similar spread and could not be discerned at this point. Note that because of the microtubule surface-immobilization by NVD and PLL-PEG-bt (see section 4.1), protofilaments at the bottom center were potentially blocked and kinesin was prevented from attaching to these, though the extent of blocking could hardly be assessed.

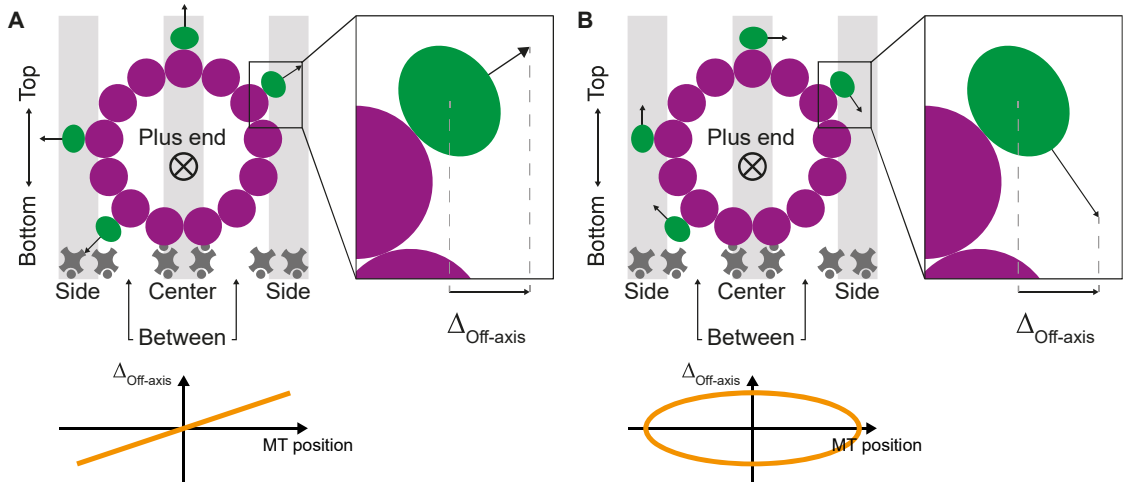

Figure 5.10: **Implications of upward or sideward head movement on the observed off-axis displacement** due to the projection onto the imaging plane. **(A)** Model of an upward movement of the kinesin head (green) away from the microtubule (MT) surface as indicated by the black arrows. Depending on the individual protofilament (purple), the projected off-axis displacement $\Delta_{Off\text{-}axis}$ can be positive (between and side right), zero (center) or negative (between and side left). **(B)** Model of a sideward movement of the kinesin head along the microtubule surface, exemplary shown in rightward direction. Depending on the individual protofilament, $\Delta_{Off\text{-}axis}$ can be positive (center and between top), zero (side) or negative (center and between bottom). Center bottom protofilaments are assumed to be partially blocked due to the surface-immobilization of the microtubules.

5.6.2 Reconstruction of the 3D Head Orientation during the Unbound State

In order to resolve the ambiguity pointed out at the end of the previous section, MINFLUX tracking measurements were performed with construct K28C while actively stabilizing the sample (see section 3.4) to allow for referencing multiple traces per microtubule relative to each other with respect to their off-axis distances and thus to different protofilaments per microtubule (without stabilization, distances between traces are distorted by drift). Employing these distances, 19 different microtubules could be identified, which allowed for matching individual traces along their cross section. The assignment was only possible for those microtubules with the distance of the outmost recorded traces being separated by around 30 nm, matching the, due to the finite size of the head and the labeling position of the fluorophore, slightly increased microtubule diameter of 25 nm.

Figure 5.11 **(A)** shows all traces recorded on one microtubule, with the outmost traces being separated by only slightly more than the expected 30 nm (grey horizontal lines). In contrast to these traces, those in the center of the microtubule display significant off-axis displacement during the unbound state. Aligning all the traces of the 19 data sets with respect to their on-axis position and microtubule orientation and plotting the detected off-axis displacement along the microtubule cross section revealed that traces at the sides consistently followed a single line, whereas traces at the microtubule center featured positive off-axis displacement of around 5 nm to the side (see figure 5.11 **(B)**). Traces that lay in-between center and side traces showed positive and negative off-axis displacement <5 nm. Strikingly, no leftward displacement was observed for central traces, suggesting that protofilaments at the bottom of the microtubule were indeed blocked due to the surface-immobilization. This breaking of symmetry, in turn facilitated the distinction between leftward and rightward displacement. Overall, while non-perfect overlap of the trace data sets might have caused small errors in the lateral position, the general trend agrees well with an **true rightward displacement** of the kinesin head during the unbound state (compare to figure 5.10 **(A,B)**, bottom). Fitting an ellipse to the data yielded an average microtubule diameter of 30 nm and an actual rightward displacement of 4.8 nm.

Combined with the observed variations in the on-axis substep size, these results allowed for the reconstruction of the 3D-orientation of the unbound head (see figure 5.11 **(C)**). When entering the unbound state, the head rotates around its front to the right side with respect to the walking direction. Thereby, the front of the head is fixed in space, while the back of the head is moved forward by 8 nm and rightward by $\sim$ 5 nm. The labeling position at the center of the head advances by around 6 nm, but is not strongly shifted to the side. Summarizing, this 3D-model of the unbound kinesin head is based on over 12,000 steps detected within 1338 traces.

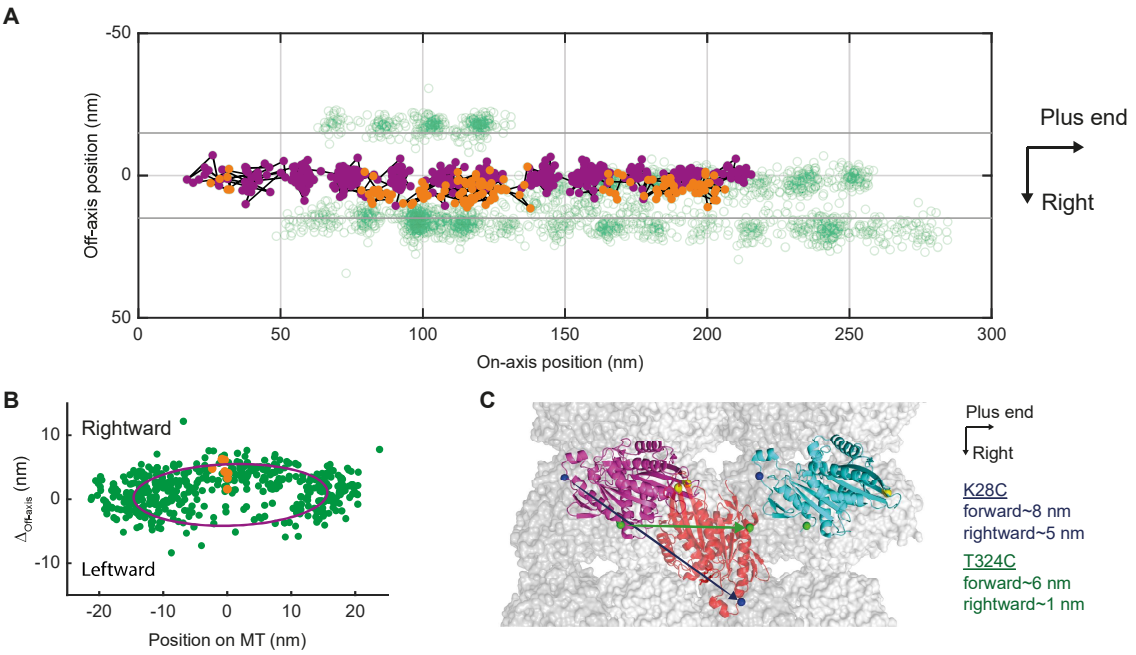

Figure 5.11: **Reconstruction of the 3D-orientation of the unbound head** invoking all measured kinesin constructs. **(A)** 2D-scatter plot of the on-axis and off-axis positions of all traces (green circles) recorded on an exemplary microtubule (MT) together with the expected MT outline (horizontal grey lines). The trace at the MT center (purple dots) displays clear rightwards displacement during the unbound state (orange dots). **(B)** Off-axis displacement of all detected substeps and their corresponding position along the MT cross section (green dots) together with an ellipse fit (purple ellipse). The off-axis displacement of the trace highlighted in (A) is marked by the orange dots. **(C)** Reconstructed 3D-orientation of the unbound head (orange; PDB: 1MKJ), as inferred from the on-axis and off-axis step sizes of all measured constructs. Arrows depict the displacement of the individual labeling positions from the trailing head's (dark magenta; PDB: 3J8Y) bound state. The leading head is depicted in its apo state (cyan; PDB: 4ATX). All heads are shown on the MT surface (alpha-tubulin in dark grey, beta-tubulin in light grey, PDB: 6DPU).

5.7 MINFLUX Tracking of Proteins

This chapter proved MINFLUX to be a powerful and reliable tool for studying protein movement under force- and load-free conditions at the nanometer and millisecond scale. For the first time 4 nm substeps of the coiled-coil domain of kinesin were visualized at 10 µM and 1 mM ATP concentrations without artificially pulling on the protein. The localization precision of below 2 nm further enabled the identification of a rotation of the coiled-coil domain upon stepping by resolving nanometer sized changes in evaluated step sizes. While these aspects have in principle been speculated by bead tracking studies

[59], the inherently large size of the label and consequently steric hindrance supposedly distorted or amplified the detected displacements significantly, questioning those observations. Labeling with a nanometer-sized fluorophore allowed for the simple introduction of a second dye on the protein and thus a symmetric labeling of the center of the coiled-coil domain to verify the hypothesis.

By further tracking constructs with one of their heads labeled, MINFLUX enabled an in-depth analysis of kinesin's 1HB state, concerning both its role in the mechanochemical cycle and deriving the average orientation of the unbound head. Applying a HMM to evaluate the times spent in the bound and unbound state revealed a negative correlation between the dwell time of the 1HB state and the ATP concentration. It was consequently followed that kinesin binds ATP in the 1HB state. Additionally replacing ATP by ATPγS, a slowly hydrolizing ATP analogue, not only confirmed the 1HB state to be ATP dependent, but disclosed that in fact the hydrolization of ATP occurs in the 2HB state. Although this conclusion has been drawn by a bead tracking study [59], a comparable study has simultaneously found contradicting results [60]. Due to their large size, beads are likely to display a distorted image of the true protein trajectory and consequently cause fallacious interpretations.

Recording the 2D-trajectories of three different kinesin constructs labeled at either the front, middle or back of the head allowed to derive a rotation of the trailing head around its front upon entering the unbound state. The orientation of the head could be refined even further by allocating individual traces along the microtubule cross section, based on the tracking data acquired with an actively stabilized sample. The results specified the rotation of the unbound head around its front to the directed to the right side with respect to the walking direction. This model differs significantly from previously models based on FRET experiments [57]. While in principle the presented experiments are also possible with bead labels, the size-induced influence of varying labeling positions on the apparent trajectory is not easily foreseeable [61]. In contrast, the single small fluorophore required for MINFLUX visualizes the track of the labeling position with much smaller linkage error and considerably reduced risk for artifacts due to steric hindrance. Taken together, the consistent rightward displacement of the labeled head during the unbound state (as labeling is stochastic and kinesin a homodimer, each monomer can be tracked) combined with the rotation of the coiled-coil domain upon stepping (which is expected to abolish the twist introduced when one head passes the other) strongly point towards a symmetric hand-over-hand model [62] with each head passing the other one on the right side. The walking model of kinesin is still a controversially debated part of kinesin research with opposing evidence. To this end, future MINFLUX measurements could provide further corroboration by increasing the fluorophore displacement from the coiled-coil domain and tracking the corresponding off-axis displacement during substepping.

Finally, it shall be noted that in parallel to this thesis, a MINFLUX tracking study of kinesin in both living and fixed cells also recorded data of the coiled-coil domain (fixed cells) and head movements (living cells) [66]. For 2D-tracking, this study employed L =75 nm, more than twice as large as the L used in this thesis, reducing the expected precision at a given number of detected photons by a factor of two in comparison to the presented work. Nevertheless, by recording many tracks of up to several micrometer in length, individual antiparallel microtubules could be discerned as close as 12 nm apart. Further, individual 16 nm steps could be clearly visualized in living cells and untreated, living primary neurons (mouse). In the last step, 3D-tracking was achieved in fixed U2OS cells with $L = 100$ nm. Please note that [66] is a not yet peer reviewed preprint and shall be treated with caution.
In good agreement, the *in cellulo* data of kinesin and the *in vitro* results of this work both reliably recognize the 16 nm steps of kinesin. However, in contrast to this work, no substeps have been reported at physiological ATP concentrations, which likely can be attributed to the increased mobility of microtubules in living cells and the presumably lower STP due to the larger L. While the walking speed in living cells and *in vitro* were comparable for the truncated, head-labeled constructs, the full-length kinesin constructs labeled at the coiled-coil domain displayed reduced walking speeds due to auto inhibition caused by the cargo-binding domain [68, 69], which was not present in the truncated constructs used else. Further, a significant fraction of the coiled-coil-labeled constructs disclosed alternating left and right moving trajectories in fixed cells, similar to the alternating sequence of 6 nm and 10 nm steps observed in this work, this very likely is an indication for the coiled-coil rotation.

Overall, the high STP of MINFLUX, especially at the small L enabled by the higher curvature of the interferometric excitation profile, allowed for this detailed and sophisticated analysis of kinesin steps and substeps. A broad range of topics central to kinesin research were tackled with a single technique, advocating MINFLUX as a new, vital tool for studying dynamics of not only kinesin, but the plethora of proteins relevant to the proper functioning of a healthy cell.

Conclusion and Outlook

The advanced MINFLUX microscope, designed and realized in this thesis, distinguishes itself from current MINFLUX implementations by dynamically synthesizing an excitation intensity distribution with a line-shaped (LS) minimum and by achieving near one nanometer precision consuming as little as 20 fluorescence photons per localization and dimension. These highly efficient localizations facilitated tracking of surface-immobilized ATTO 647N molecules with a record spatio-temporal precision (STP) of below 2 nm precision at 0.63 ms sampling time. Having verified the high STP and accuracy of the microscope, a comprehensive study investigating the stepping motion of the motor protein kinesin was conducted, which covered a broad range of topics central to kinesin research. As opposed to employing large beads to label the protein, MINFLUX provides a competitive STP by tracking just a single fluorescent molecule and thereby outperforms camera-based single fluorophore tracking speed by two orders of magnitude.

By matching the precisely known position of a local excitation intensity minimum with the location of a fluororescent molecule, MINFLUX minimizes instead of maximizes the fluorescence photons needed to obtain a high localization precision. Rather than actually uniting the minimum and the fluorophore position, it is sufficient to probe the molecule with a set of excitation beam coordinates, characterized by a total spacing of L, and extrapolate the distance to the molecule, knowing the shape of the excitation profile. This new approach of tailoring the excitation to a single emitter has by far not fully exploited its true theoretical limits and applications. As the photon information content (PIC) is increased through measuring close to the emitter position, MINFLUX qualifies for fast and precise single molecule tracking. In contrast to MINFLUX imaging, where many fluorescence photons are required in the zoom-in process and the highly informative fluorescence photons recorded at the smallest L contribute only to a small extent to the total fluorescence photon budget, MINFLUX tracking employs the smallest L nearly throughout the measurement, allowing to record a trajectory exclusively with the use of genuinely highly informative fluorescence photons. Thus, the crux to boost MINFLUX tracking is to enable the use of smaller L-values by increasing the curvature around the excitation minimum and/or by reducing background. This thesis replaces the excitation donut, typ-

ically used for MINFLUX, by two orthogonal excitation profiles with LS minima for the sequential performance of one-dimensional (1D) localizations in x- and y-direction. LS minima are known to have a steeper curvature compared to the donut profile [4] and therefore promise an enhanced MINFLUX performance.

Consequently, the development of the phase scanner, which generates and moves the LS minimum, was central to this work. The phase scanner forms and modulates four different beams regarding their amplitude and phase, such that two laterally or horizontally displaced beams interfere in the focal plane and generate two orthogonal excitation intensity distributions featuring LS minima. Changing the phase difference between the beams precisely shifts the position of the LS minimum along the axis of beam displacement. As the phase difference must be controlled and stable to less than 1 % of the wavelength, a very compact and, in terms of active components, also irreducible implementation of the phase scanner was envisioned and realized, yielding phase drifts in the order of a few nanometers per hour and a stability below 1 Å at 1 s temporal resolution.
Employing the phase scanner for tracking of surface-immobilized ATTO 647N molecules with an L of 16 nm provided an average precision of 1.7 nm with as little as 21 fluorescence photons collected in 0.63 ms. This experimental result is around 20 % above the theoretically predicted precision of 1.45 nm, as on the true nanometer scale disturbances by sample drift, external and microscope-internal vibrations and flexibility in the fluorophore immobilization can be minimized, but not fully excluded. Additionally, the ATTO 647N molecules were moved in different experiments on either continuous or stepwise trajectories while following their position with an L of 30 nm. Both experiments confirmed the absence of a compromise in the achievable localization precision for moving emitters and validated the high accuracy of the phase scanning MINFLUX microscope of above 95 %. This extraordinary performance in STP emphasizes the importance of reducing the L-value, in order to fully exploit the conceptual difference between MINFLUX and conventional super-resolution techniques.

In addition to developing the phase scanner, an important focus of this thesis was to demonstrate the applicability of MINFLUX tracking to relevant biological studies in the field of single particle tracking. The motor protein kinesin has been studied extensively with various techniques for decades. Nevertheless, insights into its mechanochemical cycle remain incomplete. Kinesin therefore represents an ideal model system for highlighting the strengths of MINFLUX tracking, while it at the same time still holds unsettled biological questions.
Tracking the movement of individual kinesin heads with around 3 nm precision and 0.63 ms temporal resolution directly visualized steps and substeps. Based on the reconstruction of the sequence of bound and unbound states of the head by a hidden Markov model

(HMM), the dwell times of these states were evaluated for different ATP analogues and ATP concentrations. Kinesin was found to bind ATP during its one-head-bound (1HB) state and to hydrolize ATP during the two-head-bound (2HB) state, answering a controversial question in the kinesin research field. By further focussing on the step sizes along the microtubule axis and perpendicular to it of three different kinesin constructs labeled at the front, middle and back of the kinesin head, recorded with a median precision of below 1 nm, a rotation of the labeled head during the unbound state was revealed. This result was refined into an average 3D-orientation of the unbound head by additionally assigning individual kinesin traces along the microtubule cross section. Complementary, 1D-measurements of the position of the coiled-coil domain along the microtubule axis with below 2 nm precision disclosed nanometer-sized variations in the observed step sizes, which were attributed to a rotation of the coiled-coil domain upon stepping. Taken together, the data support a highly symmetric stepping of kinesin, which suggests that kinesin walks in symmetric hand-over-hand manner with the trailing head always passing the leading head on the right side.

Based on the obtained results and the overarching experiences gained a follow-up experiment to directly record the symmetric or asymmetric walking behavior can be envisioned. Labeling the coiled-coil domain of kinesin with a fluorophore that is slightly, yet significantly, displaced from the coiled-coil core ($\geq$5 nm) is expected to cause a visible sideward shift of the trace during the 1HB state, which is compensated after the next substep with both heads being bound to the microtubule again. If the coiled-coil domain rotates unidirectionally, the shift will occur both to the left and to the right with respect to the kinesin walking direction. However, if the coiled-coil domain rotates back and forth from step to step, this shift will consistently occur only to one side for individual traces.
In order to achieve the highest possible STP for this proposed experiment, besides optimizing acquisition parameters, the MINFLUX data quality can be enhanced by further improving the re-evaluated position estimates during post-processing. As fundamentally no better fit of the parabola is possible, this approach will require the careful introduction of further assumptions, which allow for a more precise and robust position estimate (similar to the sliding-curvature estimator), without introducing systematic errors.

For enhancing the localization precision and stability of the microscope in general, it is recommended to further increase its compactness and add passive and active measures to ensure temperature stability. The microscope realized in this thesis required an adaptable arrangement during development to allow for project flexibility. However, sacrificing this flexibility by minimizing the beam length reduces the beam-susceptibility to air flow and ensures a more homogenic temperature throughout the microscope, thus decreasing drift. Additionally, it became evident that the stage and sample are the most relevant

points-of-entry for vibrations and especially vulnerable to temperature changes. In an improved design, special attention should be paid to these components by installing a profound encapsulation, as well as to passively reducing temperature influences by introducing increased symmetry. This can be for example achieved by directly mounting the stage to the objective and connecting the sample holder on opposite sites. In doing so, thermal expansion would be centered around the objective and hence would have less impact on the sample. Additionally, the temperature at the objective and throughout the rest of the microscope should be actively stabilized to diminish any remaining temperature influences. The long term stability can be increased by monitoring the excitation beam angle and correcting for slow drift. At the same time monitoring the phase on a camera would also enable to stabilize the position of the LS minimum. Finally, technical limitations caused by the finite precision of components can be improved at least gradually by for example changing the magnification of the galvo scanner, thereby trading the field of view for increased precision.

As the interference-based synthesis of the focal intensity distribution can be facilitated at any excitation wavelength with the phase scanner, deploying multi-color MINFLUX tracking would further exploit the microscope's potential. The switching speed between wavelengths is not limited by adapting the voltages to changed phase scanner calibration values, but rather by the laser intensity control of the acousto optical tunable filter (AOTF). The latter can be improved when optimizing the timing of signals by anticipating the speed of the sound wave in the crystal of the AOTF. Consequently, the phase scanner is capable of switching colors at the scale of microseconds instead of milliseconds as required by a spatial light modulator. A substantial advantage of excitation and detection based multi-color approaches is the possibility to almost eliminate cross talk. In the first step, a proof of concept should be demonstrated and both requirements and limits explored.

Through the implementation and optimization of the phase scanner, an improved setup for MINFLUX tracking at nanometer precision and millisecond temporal resolution using below 100 fluorescence photons per localization was realized. The ability to routinely apply a small L of 30 nm for non-technical samples allowed for a detailed study of kinesin, further advancing the biophysical understanding of its stepping motion. With the prospect of future multi-color tracking applications MINFLUX qualifies as a highly versatile tool for studying the biological dynamics at the molecular level and advances the field of single fluorophore tracking to hitherto unreached STP.

Appendix A

Appendix

A.1 Generalized least squares

Being given a typical multiple lineare regression model of order K and T data points

$$\{y_t, x_{tk}\}_{t\in[1,T],k\in[1,K]} \tag{A.1}$$

In the linear model the data can be described by the model paremeters β and the residual error vector ϵ

$$\begin{pmatrix} y_1 \\ \vdots \\ y_T \end{pmatrix} = \begin{pmatrix} x_{11} & \cdots & x_{1K} \\ \vdots & \ddots & \vdots \\ x_{T1} & \cdots & x_{TK} \end{pmatrix} \cdot \begin{pmatrix} \beta_1 \\ \vdots \\ \beta_3 \end{pmatrix} + \begin{pmatrix} \epsilon_1 \\ \vdots \\ \epsilon_3 \end{pmatrix} \tag{A.2}$$

This expression can be written in the compact form

$$y = x\beta + \epsilon \tag{A.3}$$

The error vector ϵ has the expectation value of zero $E(\epsilon) = 0$ however the covariance matrix $\Phi_\epsilon = E(\epsilon\epsilon^T)$ is in general a non singular positiv semidefinite Matrix of order T. If the data points are independent the non diagonal elements of Φ are zero. This case is called heteroscedastic.

$$\Phi = \begin{pmatrix} \sigma_{11}^2 & \cdots & 0 \\ \vdots & \ddots & \vdots \\ 0 & \cdots & \sigma_{TT}^2 \end{pmatrix} \tag{A.4}$$

The σ_{ii}^2 are the variances of the data points.
To estimate the regression parameters one uses a least squares estimator weighted by the

covariance matrix

$$b = \left(x^T \Phi^{-1} x\right)^{-1} x^T \Phi^{-1} y \tag{A.5}$$

This is called the generalized least squares estimator (GLSE). To calculate the precision of this estimator one has to consider the covariance matrix of the estimated parameters b

$$\Sigma_b = E\left((b - E(b))(b - E(b))^T\right) \tag{A.6}$$

With the GLSE (A.5) and the fact that $y - E(y) = \epsilon$ the covariance matrix becomes

$$\begin{aligned} \Sigma_b &= (x^T \Phi^{-1} x)^{-1} x^T \Phi^{-1} E(\epsilon\epsilon^T) \Phi^{-1} x (x^T \Phi^{-1} x)^{-1} \\ \Sigma_b &= (x^T \Phi^{-1} x)^{-1} x^T \Phi^{-1} \Phi \Phi^{-1} x (x^T \Phi^{-1} x)^{-1} \\ \Sigma_b &= (x^T \Phi^{-1} x)^{-1} \end{aligned} \tag{A.7}$$

The GLSE is best lineare unbiased estimator. This means that there is no other linear unbiased estimator with smaller covariance matrix.

Calculation of the GLSE

As described in the section before the GLSE is given by equation A.5. Now assuming three exposures at positions $x \in [-L/2, 0, L/2]$, measured counts $y = (n_2, n_0, n_1)^T$ and estimating the error-covariance matrix by possonian noise

$$\Phi = \begin{pmatrix} n_2 & 0 & 0 \\ 0 & n_0 & 0 \\ 0 & 0 & n_1 \end{pmatrix} \tag{A.8}$$

the GLS estimate and the covariance matrix become

$$\begin{aligned} b &= \begin{pmatrix} n_0 \\ \frac{n_1 - n_2}{L} \\ \frac{2}{L^2}(n_1 + n_2 - 2n_0) \end{pmatrix} \\ \Sigma_b &= \begin{pmatrix} n_0 & 0 & -\frac{4n_0}{L^2} \\ 0 & \frac{n_1+n_2}{L^2} & \frac{2(n_1-n_2)}{L^3} \\ -\frac{4n_0}{L^2} & \frac{2(n_1-n_2)}{L^3} & \frac{4(4n_0+n_1+n_2)}{L^4} \end{pmatrix}. \end{aligned} \tag{A.9}$$

From these results one can obtain the molecule position $x_m = -b_2/(2b_3)$ and its standard deviation $\Sigma_x = J^T \Sigma_b J$ (here $J = \nabla_b x_m$ denotes the Jacobian matrix of the molecule

position with respect to b). Position and standarddeviation are given by

$$\begin{aligned} x_{\mathrm{GLSE}} &= \frac{L}{4}\frac{n_2 - n_1}{n_1 + n_2 - 2n_0} \\ \sigma &= \frac{L}{2}\frac{\sqrt{(n_2 - n_1)^2 n_0 + (n_2 - n_0)^2 n_1 + (n_1 - n_0)^2 n_2}}{(n_1 + n_2 - 2n_0)^2}. \end{aligned} \tag{A.10}$$

A.2 Optimal MINFLUX procedure

Optimal Photon Distribution

The first aim is to calculate the optimal distribution of N photons over n steps in order to reach the best possible precision. This represents a maximization problem under boundary conditions and can be solved by employing Lagrange multipliers. The lagrangian fuction is given by

$$L(N_i, \lambda) = \prod_i N_i - \lambda(\sum_i N_i - N_{tot}) \tag{A.11}$$

Here λ is the so called Lagrange multiplier. To solve for N_i we need to look at the gradient of L.

$$\begin{aligned} (\nabla_N L)_j = \frac{\partial}{\partial N_j}\left(\prod_i N_i - \lambda(\sum_i N_i - N_{tot})\right) &= 0 \\ \frac{\prod_i N_i}{N_j} - \lambda &= 0 \\ \prod_i N_i &= \lambda N_j \end{aligned} \tag{A.12}$$

Since the left side of this equation is constant and it holds for all j it follows that

$$N_i = N_j = N_{tot}/n, \forall i, j \tag{A.13}$$

With this result the precision after n exposures is given by

$$\begin{aligned} \sigma_n &= \sigma_0 \frac{\alpha^n}{4^n \sqrt{N_{tot}/n}^n} \\ &= \sigma_0 \left(\frac{\alpha}{4\sqrt{N_{tot}}}\sqrt{n}\right)^n \end{aligned} \tag{A.14}$$

Optimal number of steps

Now, after having proven that in order to get the best possible precision after n steps and N_{tot} photons one has to distribute those photons equally over all steps, the question remains whether there is an optimal number of steps for a given number of total photons. Therefor one has to look at the derivative of σ_n

$$\frac{\partial \sigma_n}{\partial n} = \sigma_0 \left(\frac{\alpha}{4\sqrt{N_{tot}}} \sqrt{n} \right)^n \left[\ln \left(\frac{\alpha}{4\sqrt{N_{tot}}} \sqrt{n} \right) + \frac{1}{2} \right] = 0. \tag{A.15}$$

Since the first term is always positive, the derivative becomes zero for

$$\begin{aligned} \ln \left(\frac{\alpha}{4\sqrt{N_{tot}}} \sqrt{n_{opt}} \right) + \frac{1}{2} &= 0 \\ n_{opt} &= \frac{16 N_{tot}}{e\alpha^2}. \end{aligned} \tag{A.16}$$

This means that the optimal number of steps is directly linked to the total number of photons and the factor α that decides how fast the zooming-in process is made. Therefore the precision after n steps becomes

$$\sigma_n = \sigma_0 e^{-8N_{tot}/e\alpha^2} \tag{A.17}$$

Following this result, the precision increases exponentially with the number of photons. To get a feeling for the number of photons needed to reach $\sigma_n = 1$ nm precision, one assumes an initial precision given by the diffraction limited precision of the focal spot ($\sigma_0 = 100$ nm). With this values the total number of photons becomes

$$N_{tot} = \frac{e\alpha^2}{8} \ln \left(\sigma_0 / \sigma_n \right). \tag{A.18}$$

Now we have to assume a value for the regularization parameter α. Obviously, the number of photons needed quadratically scales with α. Assuming $\alpha = 0$ would therefore result in 0 photons to reach any desired precision. This obviously is not a physical result and only occurs because this theory assumes continous number of photons, to allow for taking derivatives.

One possibility to put constraints on the scaling factor is by requiring at least one photon per iteration step. From equation A.16 the number of photons per step is given by $N_i = e\alpha^2/16$. Employing this and setting $N_i = 1$ the minimal α is given by $\alpha_{min} = 4/\sqrt{e} \approx 2.4$. Another argument for choosing α is by requiring that on average 96 % of all localizations are withing the next step. Since localizations are normally distributed this means $\alpha = 4$. The total number of photons needed is then given by $N_{tot} = 25$.

In comparison, the number of photons need to reach the same precision in STORM is

100^2 =10,000, which is 400 times higher than for MINFLUX. Since there is no function decaying faster than an exponential, it seems like there is no fundamentally faster way to gain precision than MINFLUX.

A.3 Estimator Comparison

This section discusses the GLSE as well as the fixed-curvature estimator (FCE) and the sliding-curvature estimator (SCE) used throughout this thesis. The GLSE corresponds to fitting a parabola of the form $y(x) = a + b\,(x - x_{\mathrm{M}})^2$ to each measurement triplet. Thereby, changes to the parabola over time by for example photobleaching of one emitter for the double labeled coiled-coil, or changes in the detection efficiency, caused by kinesin walking towards the periphery of the confocal volume, are intrinsically accounted for. As three points can exactly be described by one parabola no better calculation of the three parameters can be achieved. However due to the simultaneous estimation of all three parameters, this becomes highly susceptible to noise, especially for low fluorescence photon numbers and SBR.

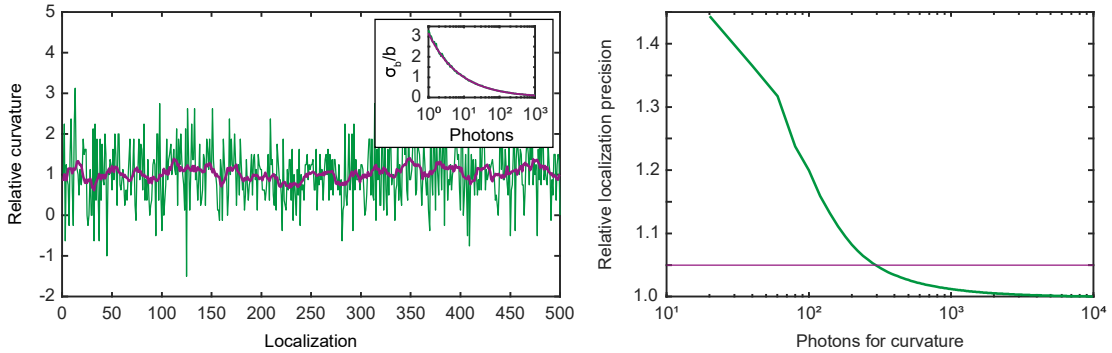

Figure A.1: **Precision of the sliding-curvature estimator (SCE)** depending on the width of the sliding window. Left: Poisson-distributed photon counts for 500 localizations were generated with a SBR of one and an average sum of 20 photons. For each localization the curvature was estimated based on equation 3.3 (green curve) and smoothed by a sliding-window of width 15 (purple curve). The inlay shows the relative precision of the curvature depending on the number of photons. Right: Numerical simulation of the localization precision, relative to the theoretical limit depending on the number of photons used to calculate the curvature of the parabola. Poisson-distributed photon counts of 100 traces were generated and evaluated with the SCE and varying window length. At a window length collecting around 300 photons the SCE approaches the theoretical limit to 5 %.

In order to increase the precision of position estimates, further assumptions about the

parabola need to be made. A straight forward approach is to fix the curvature of the position estimate by the mean curvature of many localizations. This approach was called SCE (see equation 5.1) and yields valid results, if the apparent curvature does not change significantly on the time scale on which the curvature is averaged. The window size of the SCE was optimized by simulating localizations of 100 traces with Poisson-distributed photon counts and processing them by the SCE. The precision of the SCE improves linearly with increasing window length and, when collecting over 300 photons for evaluatig the curvature, matches the theoretical limit by 5 % (see figure A.1).

Figure A.2 depicts the simulated precision relative to the displacement L for the GLSE, the FCE and the SCE for different number of photons and SBR. The window size of the SCE was selected such, that the curvature was determined with 300 photons on average. Due to the low contrast and thus frequent outliers caused by apparent near zero curvature of single localizations, the GLSE performs worse for small number of photons and low SBR. The FCE and SCE enable optimal precision independent of the SBR or the number of photons. For localizing stationary emitters the FCE provides optimal precision, whereas for kinesin tracking measurements the SCE is more suitable, as most tracks display significant decrease of the total photon counts when reaching the outer parts of the detection volume.

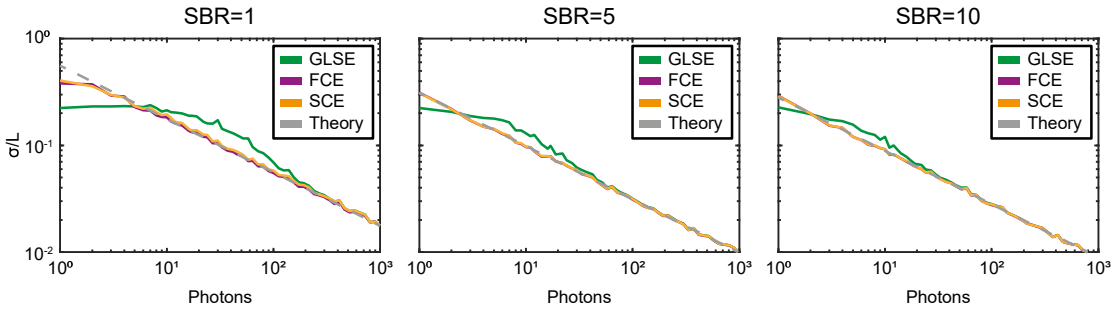

Figure A.2: **Precision of the generalized least-squares estimator (GLSE), the fixed-curvature estimator (FCE) and the sliding-curvature estimator (SCE)** depending on the SBR and the number of total photons. For each total photon number 1000 Poisson distributed photon counts, corresponding to the different exposures, were generated. Those were then filtered to have positive curvature and a maximum displacement of L. The remaining localizations were analyzed according to section 4.2.2 to retrieve the localization precision. The dashed grey line displays the best achievable theoretical precision.

A.4 RSS reduction by artificial steps

The step-finding algorithm described in section 4.2.3 finds steps by minimizing the RSS

$$RSS = \sum_{i=1}^{N} (x_i - \bar{x})^2 \tag{A.19}$$

while adding a penalty β for each step to prevent overfitting. This penalty factor should be larger than the RSS reduction in noisy traces with constant mean. Consulting the expectation value (E) of the unbiased estimator for the sample variance

$$E\left(\sum_{i=1}^{N} (x_i - \bar{x})^2\right) = (N-1)\mathrm{var}(x), \tag{A.20}$$

the expectation value of the RSS reduction $\Delta RSS = (RSS_{\text{Const.}} - RSS_{\text{Step}})$

$$\begin{aligned} E\left(\Delta RSS\right) &= E\left(\sum_{i=1}^{N} (x_i - \bar{x}_{1:N})^2 - \sum_{i=1}^{k} (x_i - \bar{x}_{1:k})^2 - \sum_{i=k+1}^{N} (x_i - \bar{x}_{k+1:N})^2\right) \\ &= (N-1)\mathrm{var}(x) - (k-1)\mathrm{var}(x) - (N-k-1)\mathrm{var}(x) \\ &= \mathrm{var}(x) = \sigma^2 \end{aligned} \tag{A.21}$$

of an artificial step at index k can be calculated. The term $\bar{x}_{a:b}$ denotes the mean value of all x_i for $i \in [a, ..., b]$. In detail, the first step uses the fact, that no actual steps are present in the data and hence that $\mathrm{var}(x)$ and $E(x)$ are constant for each of the considered segments.

A.5 Additional Figures

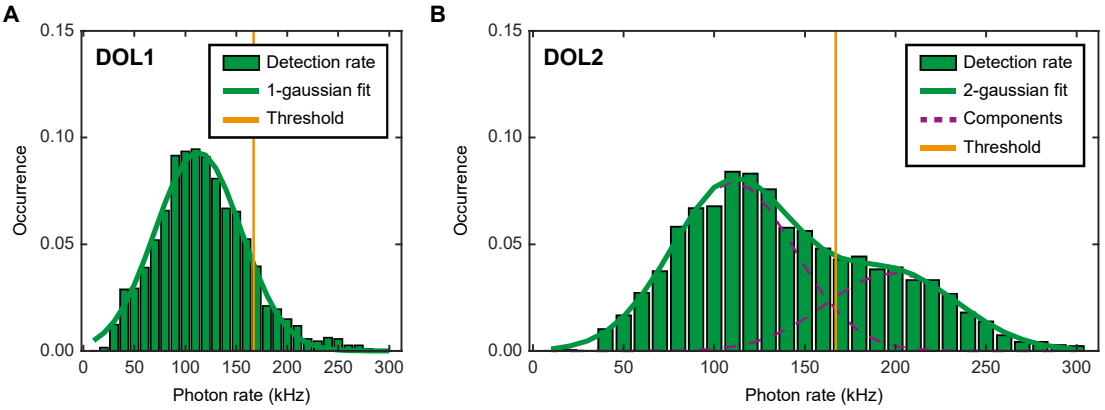

Figure A.3: **Histogram of the average photon rates of plateaus** for data recorded with the construct N356C. **(A)** DOL1: Population normalized histogram of the mean photon rate recorded in each plateau together with a Gaussian fit (green line) and the threshold for the DOL2 data (orange line). **(B)** DOL2: Population normalized histogram of the mean photon rate recorded in each plateau together with a two-component Gaussian fit (green line). The two components are shown by the dashed purple lines and the photon threshold at 167 kHz separating the two components is displayed by the orange line.

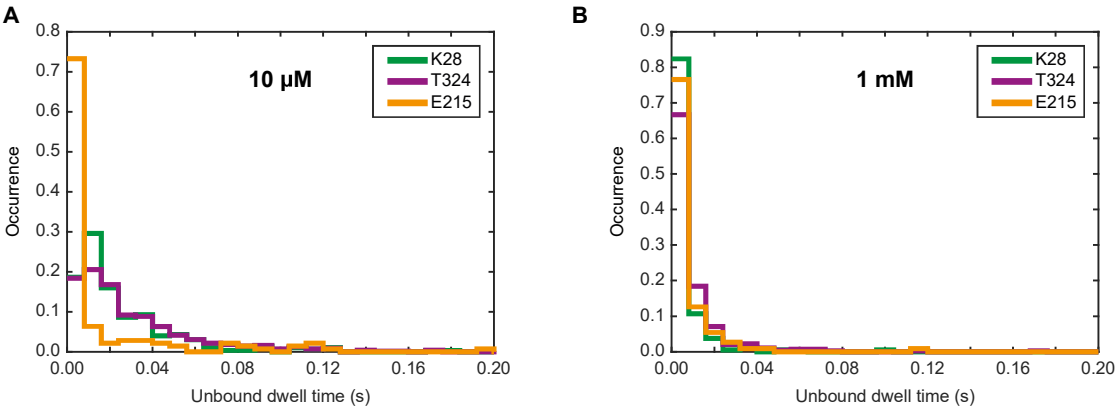

Figure A.4: **Histogram of the dwell times in the unbound state** for all head-labeled constructs. **(A)** Population normalized histograms of the dwell time in the unbound state at 10 µM ATP concentration. **(B)** Population normalized histograms of the dwell time in the unbound state at 1 mM ATP concentration.

List of Tables

List of Figures

Publications

J. O. Wolff, L. Scheiderer, T. Engelhardt, J. Engelhardt, J. Matthias, S. W. Hell. MINFLUX dissects the unimpeded walking of kinesin-1. 2022, submitted (available as preprint on *bioRxiv*)

Bibliography

[1] F. Wang, D. Banerjee, Y. S. Liu, X. Y. Chen, and X. G. Liu. Upconversion nanoparticles in biological labeling, imaging, and therapy. *Analyst*, 135(8):1839–1854, 2010.

[2] F. Pinaud, S. Clarke, A. Sittner, and M. Dahan. Probing cellular events, one quantum dot at a time. *Nat Methods*, 7(4):275–285, 2010.

[3] S. W. Hell and J. Wichmann. Breaking the diffraction resolution limit by stimulated emission: stimulated-emission-depletion fluorescence microscopy. *Opt Lett*, 19(11):780–2, 1994.

[4] T. A. Klar, E. Engel, and S. W. Hell. Breaking abbe's diffraction resolution limit in fluorescence microscopy with stimulated emission depletion beams of various shapes. *Phys Rev E*, 64(6 Pt 2):066613, 2001.

[5] E. Betzig, G. H. Patterson, R. Sougrat, O. W. Lindwasser, S. Olenych, J. S. Bonifacino, M. W. Davidson, J. Lippincott-Schwartz, and H. F. Hess. Imaging intracellular fluorescent proteins at nanometer resolution. *Science*, 313(5793):1642–1645, 2006.

[6] M. J. Rust, M. Bates, and X. W. Zhuang. Sub-diffraction-limit imaging by stochastic optical reconstruction microscopy (STORM). *Nat Methods*, 3(10):793–795, 2006.

[7] A. Keppler, S. Gendreizig, T. Gronemeyer, H. Pick, H. Vogel, and K. Johnsson. A general method for the covalent labeling of fusion proteins with small molecules in vivo. *Nat Biotechnol*, 21(1):86–9, 2003.

[8] G. V. Los, L. P. Encell, M. G. McDougall, D. D. Hartzell, N. Karassina, C. Zimprich, M. G. Wood, R. Learish, R. F. Ohana, M. Urh, D. Simpson, J. Mendez, K. Zimmerman, P. Otto, G. Vidugiris, J. Zhu, A. Darzins, D. H. Klaubert, R. F. Bulleit, and K. V. Wood. HaloTag: a novel protein labeling technology for cell imaging and protein analysis. *ACS Chem Biol*, 3(6):373–82, 2008.

[9] L. Schermelleh, A. Ferrand, T. Huser, C. Eggeling, M. Sauer, O. Biehlmaier, and G. P. C. Drummen. Super-resolution microscopy demystified. *Nat Cell Biol*, 21(1):72–84, 2019.

[10] J. Schnitzbauer, M. T. Strauss, T. Schlichthaerle, F. Schueder, and R. Jungmann. Super-resolution microscopy with DNA-PAINT. *Nat Protoc*, 12(6):1198–1228, 2017.

[11] C. Manzo and M. F. Garcia-Parajo. A review of progress in single particle tracking: from methods to biophysical insights. *Rep Prog Phys*, 78(12):124601, 2015.

[12] Q. Zheng, M. F. Juette, S. Jockusch, M. R. Wasserman, Z. Zhou, R. B. Altman, and S. C. Blanchard. Ultra-stable organic fluorophores for single-molecule research. *Chem Soc Rev*, 43(4):1044–56, 2014.

[13] J. Vogelsang, R. Kasper, C. Steinhauer, B. Person, M. Heilemann, M. Sauer, and P. Tinnefeld. A reducing and oxidizing system minimizes photobleaching and blinking of fluorescent dyes. *Angew Chem Int Ed Engl*, 47(29):5465–9, 2008.

[14] H. Ueno, S. Nishikawa, R. Iino, K. V. Tabata, S. Sakakihara, T. Yanagida, and H. Noji. Simple dark-field microscopy with nanometer spatial precision and microsecond temporal resolution. *Biophysical Journal*, 98(9):2014–23, 2010.

[15] F. Balzarotti, Y. Eilers, K. C. Gwosch, A. H. Gynnå, V. Westphal, F. D. Stefani, J. Elf, and S. W. Hell. Nanometer resolution imaging and tracking of fluorescent molecules with minimal photon fluxes. *Science*, 355(6325):606–612, 2017.

[16] K. C. Gwosch, J. K. Pape, F. Balzarotti, P. Hoess, J. Ellenberg, J. Ries, and S. W. Hell. MINFLUX nanoscopy delivers 3D multicolor nanometer resolution in cells. *Nat Methods*, 17(2):217–224, 2020.

[17] Y. Eilers, H. Ta, K. C. Gwosch, F. Balzarotti, and S. W. Hell. MINFLUX monitors rapid molecular jumps with superior spatiotemporal resolution. *Proc Nat Acad Sci USA*, 115(24):6117–6122, 2018.

[18] A. Yildiz, M. Tomishige, R. D. Vale, and P. R. Selvin. Kinesin walks hand-over-hand. *Science*, 303(5658):676–678, 2004.

[19] J. B. Pawley. *Handbook of Biological Confocal Microscopy*. Springer, 3 edition, 2006.

[20] B. Harke, J. Keller, C. K. Ullal, V. Westphal, A. Schonle, and S. W. Hell. Resolution scaling in STED microscopy. *Opt Express*, 16(6):4154–62, 2008.

[21] M. Hofmann, C. Eggeling, S. Jakobs, and S. W. Hell. Breaking the diffraction barrier in fluorescence microscopy at low light intensities by using reversibly photoswitchable proteins. *Proceedings of the National Academy of Sciences of the United States of America*, 102(49):17565–17569, 2005.

[22] S. W. Hell and M. Kroug. Ground-state-depletion fluorescence microscopy - a concept for breaking the diffraction resolution limit. *Applied Physics B-Lasers and Optics*, 60(5):495–497, 1995.

[23] A. Sharonov and R. M. Hochstrasser. Wide-field subdiffraction imaging by accumulated binding of diffusing probes. *Proceedings of the National Academy of Sciences of the United States of America*, 103(50):18911–18916, 2006.

[24] C. M. Wells and M. Parsons. *Cell Migration*. Springer, 2 edition, 2011.

[25] M. Vishwakarma, J. P. Spatz, and T. Das. Mechanobiology of leader-follower dynamics in epithelial cell migration. *Current Opinion in Cell Biology*, 66:97–103, 2020.

[26] G. Khachaturyan, A. W. Holle, K. Ende, C. Frey, H. A. Schwederski, T. Eiseler, S. Paschke, A. Micoulet, J. P. Spatz, and R. Kemkemer. Temperature-sensitive migration dynamics in neutrophil-differentiated HL-60 cells. *Sci Rep*, 12(1):7053, 2022.

[27] G. M. Cooper. *The Cell: A Molecular Approach*. Sunderland (MA): Sinauer Associates, 2 edition, 2000.

[28] J. Howard. *Mechanics of Motor Proteins and the Cytoskeleton*. Sunderland (MA): Sinauer Associates, 2 edition, 2001.

[29] C. Veigel and C. F. Schmidt. Moving into the cell: single-molecule studies of molecular motors in complex environments. *Nat Rev Mol Cell Biol*, 12(3):163–176, 2011.

[30] D. Magde, W. W. Webb, and E. Elson. Thermodynamic fluctuations in a reacting system - measurement by fluorescence correlation spectroscopy. *Phys Rev Lett*, 29(11):705–708, 1972.

[31] E. L. Elson and D. Magde. Fluorescence correlation spectroscopy .1. conceptual basis and theory. *Biopolymers*, 13(1):1–27, 1974.

[32] A. Carisey, M. Stroud, R. Tsang, and C. Ballestrem. Fluorescence recovery after photobleaching. *Methods in Molecular Biology*, 769:387–402, 2011.

[33] N. Li, R. Zhao, Y. H. Sun, Z. Ye, K. M. He, and X. H. Fang. Single-molecule imaging and tracking of molecular dynamics in living cells. *National Science Review*, 4(5):739–760, 2017.

[34] N. P. Wells, G. A. Lessard, P. M. Goodwin, M. E. Phipps, P. J. Cutler, D. S. Lidke, B. S. Wilson, and J. H. Werner. Time-resolved three-dimensional molecular tracking in live cells. *Nano Lett*, 10(11):4732–7, 2010.

[35] E. P. Perillo, Y. L. Liu, K. Huynh, C. Liu, C. K. Chou, M. C. Hung, H. C. Yeh, and A. K. Dunn. Deep and high-resolution three-dimensional tracking of single particles using nonlinear and multiplexed illumination. *Nat Commun*, 6, 2015.

[36] C. Hellriegel and E. Gratton. Real-time multi-parameter spectroscopy and localization in three-dimensional single-particle tracking. *J. R. Soc. Interface*, 6 Suppl 1:S3–14, 2009.

[37] A. R. Dunn and J. A. Spudich. Dynamics of the unbound head during myosin V processive translocation. *Nat Struct Mol Biol*, 14(3):246–8, 2007.

[38] J. Ortega-Arroyo and P. Kukura. Interferometric scattering microscopy (iSCAT): new frontiers in ultrafast and ultrasensitive optical microscopy. *Phys Chem Chem Phys*, 14(45):15625–36, 2012.

[39] K. Svoboda, C. F. Schmidt, B. J. Schnapp, and S. M. Block. Direct observation of kinesin stepping by optical trapping interferometry. *Nature*, 365(6448):721–7, 1993.

[40] K. Svoboda and S. M. Block. Biological applications of optical forces. *Annu Rev Biophys Biomol Struct*, 23:247–85, 1994.

[41] M. J. Schnitzer and S. M. Block. Kinesin hydrolyses one ATP per 8-nm step. *Nature*, 388(6640):386–90, 1997.

[42] S. Sudhakar, M. K. Abdosamadi, T. J. Jachowski, M. Bugiel, A. Jannasch, and E. Schäffer. Germanium nanospheres for ultraresolution picotensiometry of kinesin motors. *Science*, 371(6530):eabd9944, 2021.

[43] Y. Seol, A. E. Carpenter, and T. T. Perkins. Gold nanoparticles: enhanced optical trapping and sensitivity coupled with significant heating. *Opt Lett*, 31(16):2429–31, 2006.

[44] R. Schmidt, T. Weihs, C. A. Wurm, I. Jansen, J. Rehman, S. J. Sahl, and S. W. Hell. MINFLUX nanometer-scale 3D imaging and microsecond-range tracking on a common fluorescence microscope. *Nat Commun*, 12(1):1478, 2021.

[45] M. Weber, M. Leutenegger, S. Stoldt, S. Jakobs, T. S. Mihaila, A. N. Butkevich, and S. W. Hell. MINSTED fluorescence localization and nanoscopy. *Nat Photonics*, 15(5):361–366, 2021.

[46] M. Weber, H. von der Emde, M. Leutenegger, P. Gunkel, V. C. Cordes, S. Sambandan, T. A. Khan, J. Keller-Findeisen, and S. W. Hell. MINSTED nanoscopy enters the angstrom localization range. *bioRxiv*, 2022.

[47] F. Gorlitz, P. Hoyer, H. J. Falk, L. Kastrup, J. Engelhardt, and S. W. Hell. A STED microscope designed for routine biomedical applications. *Progress in Electromagnetics Research-Pier*, 147:57–68, 2014.

[48] D. Meschede. *Optik, Licht und Laser*. Vieweg and Teubner, 3 edition, 2002.

[49] A. Yariv and P. Yeh. *Optical Waves in Crystals*. John Wiley and Sons, 1 edition, 2002.

[50] M. Zhao, P. R. Nicovich, M. Janco, Q. Deng, Z. Yang, Y. Ma, T. Bocking, K. Gaus, and J. J. Gooding. Ultralow- and low-background surfaces for single-molecule localization microscopy of multistep biointerfaces for single-molecule sensing. *Langmuir*, 34(34):10012–10018, 2018.

[51] R. Killick, P. Fearnhead, and I. A. Eckley. Optimal detection of changepoints with a linear computational cost. *Journal of the American Statistical Association*, 107(500):1590–1598, 2012.

[52] L. S. Goldstein and A. V. Philp. The road less traveled: emerging principles of kinesin motor utilization. *Annu Rev Cell Dev Biol*, 15:141–83, 1999.

[53] J. Howard. The movement of kinesin along microtubules. *Annual Review of Physiology*, 58:703–729, 1996.

[54] M. Thormahlen, A. Marx, S. Sack, and E. Mandelkow. The coiled-coil helix in the neck of kinesin. *J Struct Biol*, 122(1-2):30–41, 1998.

[55] H. Huang, X. Zhang, S. Li, N. Liu, W. Lian, E. McDowell, P. Zhou, C. Zhao, H. Guo, C. Zhang, C. Yang, G. Wen, X. Dong, L. Lu, N. Ma, W. Dong, Q. P. Dou, X. Wang, and J. Liu. Physiological levels of ATP negatively regulate proteasome function. *Cell Res*, 20(12):1372–85, 2010.

[56] R. A. Cross. Review: Mechanochemistry of the kinesin-1 ATPase. *Biopolymers*, 105(8):476–82, 2016.

[57] T. Mori, R. D. Vale, and M. Tomishige. How kinesin waits between steps. *Nature*, 450(7170):750–U15, 2007.

[58] S. Verbrugge, Z. Lansky, and E. J. Peterman. Kinesin's step dissected with single-motor FRET. *Proc Nat Acad Sci USA*, 106(42):17741–6, 2009.

[59] H. Isojima, R. Iino, Y. Niitani, H. Noji, and M. Tomishige. Direct observation of intermediate states during the stepping motion of kinesin-1. *Nat Chem Biol*, 12(4):290–+, 2016.

[60] K. J. Mickolajczyk, N. C. Deffenbaugh, J. O. Arroyo, J. Andrecka, P. Kukura, and W. O. Hancock. Kinetics of nucleotide-dependent structural transitions in the kinesin-1 hydrolysis cycle. *Proc Nat Acad Sci USA*, 112(52):E7186–93, 2015.

[61] K. J. Mickolajczyk, A. S. I. Cook, J. P. Jevtha, J. Fricks, and W. O. Hancock. Insights into kinesin-1 stepping from simulations and tracking of gold nanoparticle-labeled motors. *Biophysical Journal*, 117(2):331–345, 2019.

[62] A. Ramaiya, B. Roy, M. Bugiel, and E. Schaffer. Kinesin rotates unidirectionally and generates torque while walking on microtubules. *Proc Nat Acad Sci USA*, 114(41):10894–10899, 2017.

[63] W. Hua, J. Chung, and J. Gelles. Distinguishing inchworm and hand-over-hand processive kinesin movement by neck rotation measurements. *Science*, 295(5556):844–848, 2002.

[64] B. Gutierrez-Medina, A. N. Fehr, and S. M. Block. Direct measurements of kinesin torsional properties reveal flexible domains and occasional stalk reversals during stepping. *Proc Nat Acad Sci USA*, 106(40):17007–17012, 2009.

[65] S. Hasnain, M. L. Mugnai, and D. Thirumalai. Effects of gold nanoparticles on the stepping trajectories of kinesin. *J Phys Chem B*, 125(37):10432–10444, 2021.

[66] T. Deguchi, M. K. Iwanski, E.-M. Schentarra, C. Heidebrecht, L. Schmidt, J. Heck, T. Weihs, S. Schnorrenberg, P. Hoess, S. Liu, V. Chevyreva, K.-M. Noh, L. C. Kapitein, and J. Ries. Direct observation of motor protein stepping in living cells using MINFLUX. *bioRxiv*, 2022.

[67] M. Tomishige and R. D. Vale. Controlling kinesin by reversible disulfide cross-linking. identifying the motility-producing conformational change. *J Cell Biol*, 151(5):1081–92, 2000.

[68] D. S. Friedman and R. D. Vale. Single-molecule analysis of kinesin motility reveals regulation by the cargo-binding tail domain. *Nat Cell Biol*, 1(5):293–297, 1999.

[69] D. L. Coy, W. O. Hancock, M. Wagenbach, and J. Howard. Kinesin's tail domain is an inhibitory regulator of the motor domain. *Nat Cell Biol*, 1(5):288–292, 1999.

Acknowledgments

There are many people who helped me throughout my PhD. Thank you all for your support.

Especially, I want to thank Prof. Dr. Stefan Hell for giving me the opportunity and resources to accomplish this work in his lab. His supervision challenged me and my collegues to keep our projects on track, without limiting our abilities to pursue unconventional ideas. I further want to thank Prof. Dr. Joachim Spatz for being the second referee for my thesis and Prof. Dr. Selim Jochim and Priv.-Doz. Dr. Falko Ziebert for being part of the examination committee.

For their exellent co-supervision, I want to thank Dr. Johann Engelhardt and Dr. Jessica Matthias for the countless discussions about the theoretical framework of MINFLUX and their advice on research or career based questions. In detail, Hans assistance when building the microscope and especially his experience in Labview and FPGA programming helped me to improve my own skills in these areas. In the kinesin research project, Jessi played an irreplaceable role as the first contact for countless approaches regarding detailed biochemical questions, or administrative inquiries. However, she also taught me about sample preparation and buffer systems and proof-read important parts of my thesis even during her last month at the institue, which I am very grateful for.

In the lab special thanks go to now-Dr. Tobias Engelhardt and soon-to-be-Dr. Lukas Scheiderer. The shared time in the office and at the microscope together with Tobias was a pleasure. Both of us made important contributions in building the setup in a joint effort. With his broad knowledge about optics, electronics and software, Tobias taught me a lot of tricks crucial to any optics lab. The tedious work on the kinesin project together with Lukas was always productive and enjoyable. His rigorous quenstioning of results helped me gaining confidence in the interpretation of the data and making myself aware of the limitations of the microscope.

The other physics PhD students during my time in Heidelberg, namely Michael Remmel, Julian D. Rickert, Philip Matthias and Dr. Marcus Held, were, still are and will continue to be a great asset to the group. The work related discussions, as well as simply fooling around together were central to my PhD and my experience in Heidelberg. I am thankful I found some good friends in all of you. This of course also applies to all other members of the optical nanoscopy department not mentioned by name, with whom every day at the institute was fun. Whether it was playing Disc Golf, climbing in the bouldering gym or one of the many group activities we did together, all these memories are as important to me as the facts I learned.

I also want to thank all the helpful facilities at the institute and in particular the mechanical workshop, namely Martin Lukat and Daniel Berndt, for their help with any construction or device I needed and the IT-department who always provided immediate support.

Finally I want to thank Eva for always supporting and enduring me, even in times when work was piling up, but also for speaking clearly, when my greatest hurdle was myself. Also I want to thank my friends and family for supporting me, if not directly, then through knowing I can rely on them.